Mechanical Characterization and *In Vivo* Operation of an Implantable Drug Delivery MEMS Device

by

Yawen Li

B.S. Materials Science and Engineering
Xi'an Jiaotong University, China, 1995

M.S. Materials Science and Engineering
Xi'an Jiaotong University, China, 1997

ARCHIVES

Submitted to the Department of Materials Science and Engineering
in Partial Fulfillment of the Requirements for the Degree of

Doctor of Philosophy in Materials Science and Engineering

at the

Massachusetts Institute of Technology
February 2005

MASSACHUSETTS INSTITUTE OF TECHNOLOGY
APR 0 6 2005
LIBRARIES

© 2005 Massachusetts Institute of Technology
All rights reserved

Signature of Author.....

Yawen Li
Department of Materials Science and Engineering
January 31, 2005

Certified by.....

Michael J. Cima
Thesis Supervisor
Sumitomo Electric Industries Professor of Engineering

Accepted by.....

Carl V. Thompson II
Stavros Salapatas Professor of Materials Science and Engineering
Chair, Departmental Committee on Graduate Students

Mechanical Characterization and *In Vivo* Operation of an Implantable Drug Delivery MEMS Device

by

Yawen Li

Submitted to the Department of Materials Science and Engineering
on January 31, 2005, in partial fulfillment of the requirements for the degree of
Doctor of Philosophy in Materials Science and Engineering

ABSTRACT

The goal of this thesis was to advance an implantable drug delivery MEMS (MicroElectroMechanical Systems) device developed in our laboratory. This device was designed to locally deliver multiple substances in complex release profiles in order to maximize the effectiveness of drug therapies. It consists of an array of microreservoirs etched into a silicon substrate. Different types and dosages of drugs can be contained in these reservoirs capped by thin gold membranes. The drug release is achieved by the application of a small anodic potential on the gold membrane in a chloride containing medium (such as the body fluid). The gold membrane will corrode and disintegrate so that the drug contained within the reservoir is free to diffuse into the surrounding medium. Previous researchers have demonstrated *in vitro* and *in vivo* release of tracer molecules as well as a radiolabled chemotherapeutic agent (carmustine, or BCNU) from the device. However, systematic characterization of the mechanical and electrochemical behavior of gold membranes on the drug delivery device was necessary in order to achieve more reliable device performance and to demonstrate efficacy of BCNU delivered from the MEMS device against an experimental tumor model.

A bulge test apparatus was constructed to characterize the mechanical properties of gold membranes. Uniform pressure was applied from underneath the gold membrane and the membrane deflection was measured using optical interferometry. Analyzing the deflection and pressure data allowed extraction of the elastic modulus and residual stress of the gold membrane. Gold membranes with in-plane sizes ranging from 20 to 200μm showed lower modulus (126~168 GPa) than bulk (111) single crystal gold (189 GPa). But their yield strength (317~351 MPa) was higher than the bulk value.

An *in situ* experimental setup was constructed to observe the electrochemical disintegration process of the gold membranes. Real time images recorded from a CCD camera showed non-uniform corrosion occurring first around the membrane edges. Bulge tests on the corroded membranes indicated a gradual loss of mechanical integrity of the gold membranes due to corrosion. The gold membrane disintegration probably occurred by a combination of membrane thinning through active dissolution and accumulation of plastic deformation due to the transient formation of a passive film on top of the gold membrane in each voltammetry cycle.

Dense gold membranes with reproducible opening behavior are critical to the success of large scale in vivo studies and future commercial applications. Defects in the gold membranes led to premature leakage of BCNU, a small molecule drug. Wafers with sputtered gold membranes patterned by wet etching had a higher device yield and membrane quality than wafers with evaporated gold membranes patterned by lift off. The

mechanical and electrochemical studies provided guidance to improve the operation reliability and reproducibility of the drug delivery device.

In vivo release of BCNU from the drug delivery device was demonstrated in a rat flank model. Acute temporal release kinetics of ^{14}C labeled BCNU *in vivo* was evaluated by analysis of the plasma ^{14}C concentration using the accelerator mass spectrometry (AMS) technique. The *in vivo* ^{14}C labeled BCNU release profile from the activated devices was similar to that of the *in vitro* and subcutaneously injected controls. The time to reach a steady-state plasma ^{14}C concentration was on the order of one hour.

Efficacy of BCNU delivered from the drug delivery device was demonstrated in a 9L rat flank tumor model. Co-formulation of PEG with BCNU led to complete and rapid release of payload *in vivo*. The retarding effect of BCNU on the tumor growth was dose dependent in the range of 0.67 ~ 2 mg. BCNU delivered from activated devices seemed to be as effective as equipotent injections of BCNU against the tumor growth. This tumor effect study provided preliminary efficacy validation of the drug delivery device as well as important dosage information for further efficacy evaluation of the BCNU/IL-2 combination therapy.

Thesis Supervisor: Michael J. Cima

Title: Sumitomo Electric Industries Professor of Engineering

ACKNOWLEDGEMENTS

The mixed feeling of excitement and anxiety when I first came to Boston in the summer of 2000 is still fresh in my memory. Yet the time soon comes to conclude and head on a new (and still unknown) journey. My past four years at MIT has been a precious experience when I have seen myself grow intellectually and personally. I would like to thank a lot of people who helped shape this experience and make completion of this thesis possible.

The foremost thanks go to my advisor, Prof. Michael Cima, for his guidance and support throughout my graduate study at MIT, for giving me the opportunity of working on this exciting project, for providing valuable assistance in my career development, and for his encouragement and helping me to grow as a scientist.

I would like to thank my committee members for their helpful suggestions about my thesis. Prof. Robert Langer provided insight and guidance to the whole microchip project, and gave good comments on my paper drafts. Two chapters in this thesis would not have been completed without Prof. Carl Thompson giving access to the Wyko profiler in his group. The knowledge I learned from his MEMS and thin film processing classes has helped tremendously in my thesis work.

All the *in vivo* studies in this thesis would have been impossible without the collaboration of Betty Tyler in Dr. Henry Brem's group at Johns Hopkins University. It has been a pleasure to work with her. Her expertise and suggestions have helped broaden my experience.

I have had the opportunity to collaborate with Dr. Paul Henderson and Dr. John Vogel at Lawrence Livermore National Laboratory, which generated high quality data included in this thesis. Karolyn Burkhart-Schultz and Connie Beal are acknowledged for help with setting up the collaboration contract to make sure the samples were processed in a timely fashion.

I would like to thank the MTL staff, Vicky Diadiuk, Gwen Donahue, Kurt Broderick, Dan Adams, Robert Bicchieri, Paul Tierney, Dave Terry and Hongwei Sun, for teaching me various microfabrication skills, fixing the tools, and answering my processing questions.

I feel especially grateful for being a member of the microchip project team, and have benefited a great deal from the help, support and advice of past and present members. Thanks to Rebecca Shawgo for invaluable help especially when I first started in this project, to Amy Richards Grayson for help with microinjecting all the devices in my first animal study, to Hong Linh Ho Duc for his productive research that also helped my thesis greatly, to Malinda Tupper for her suggestions and help in the last year of my thesis experiment, to Audrey Johnson for helpful discussions on microfabrication issues. Grace Kim and Karen Daniel's expertise on polymer microchips has also broadened my perspectives on drug delivery.

Barbara Layne has provided invaluable help with administrative stuff with her always cheerful attitude. John Centorino and Lenny Rigione have always been patient to teach me how to use new equipment as well as to offer assistance in my experiments. James Serdy has always been willing to spend time to help me out with his machining expertise and to ask about how my research was going on.

All the students and postdocs in the Cima Group have been supportive and helpful over the past four years. I would like to especially thank Hong-Ren Wang, who helped me get adapted to the new environment when I first came to MIT. Thanks for listening to a lot of the ups and downs in my research, as well as for sharing his. I appreciate his friendship and wish him and his family all the best.

I would like to thank Hong Cai, Jianglong Chen, and Jian Shen for mutual support in our first year core course study. The company and support of them and other Course 3 Chinese graduate students have made my time at MIT more enjoyable.

I am forever grateful to my parents, who instilled in me a love of learning and a sense of integrity that led me to the completion of my graduate study and will continue to inspire me in my future endeavors. I thank them and my two brothers for their love and support wherever I go. Finally, I would like to thank my husband, Xingcheng Xiao, for his unwavering love and faith in me over all these years. I would not have achieved what I set out to do without his constant support and encouragement.

TABLE OF CONTENTS

LIST OF FIGURES

LIST OF TABLES

1 Introduction

1.1 Overview of electronic medical implants

The medical implant is defined by the U.S. Food and Drug Administration (FDA) to be "a device that is placed into a surgically or naturally formed cavity of the human body if it is intended to remain there for a period of 30 days or more"[21 CFR 812.3(d)]. Development of medical implants that incorporate electronic components, or electronic medical implants (EMI), began with the invention of the artificial cardiac pacemaker by Hyman in 1932[1], followed by the first implantation of the complete pacemaker in a Swedish patient in 1958[2]. Since then the industry has expanded to include a variety of implantable electronic devices to address different clinical indications, with an even larger demand for EMI products in the current decade due to ageing demographic trends and changing patient care strategies. The global EMI market was estimated to be $9.5 billion in 2003, which is projected to grow to $11.9 billion in 2004 and $32.3 billion in 2009[3].

A cardiac pacemaker is essentially a pulse generator that delivers electric signals to the heart to restore its regular rhythm in a patient usually with an abnormally slow heartbeat. Technological advances over the past 40 years have transformed the early bulky, single-chamber, fixed rate pacemakers to small, multiprogrammable, dual chamber, rate adaptive devices with diagnostic functions[4-7]. Of particular importance is the implantable cardioverter-defibrillator (ICD), which has been clinically established as an effective method for use both in primary prevention of life-threatening events and in secondary prevention of potentially fatal arrhythmia or cardiac arrest in patients with coronary disease[8, 9].

Today's EMI industry has spun into a wide array of life improving and life saving products. Neurostimulators are the descendants of the cardiac pacemaker and have been developed to restore posture and movement loss or bladder control function due to spinal cord injury[10-13]. They have also been used in deep brain stimulation for treatment of Parkinson's disease, and in vagus nerve stimulation for control of epilepsy[14]. The cochlear implant has enjoyed remarkable success over the past 10 years to restore hearing loss to profoundly deaf people by electrical stimulation of the auditory nerve[15, 16].

Ongoing studies by different research groups are aiming at development of electronic retina implants to restore sight to millions of people around the world who suffer from degenerative eye diseases[17, 18].

Applications descrbied above utilize electric signals to stimulate the cardiac and nervous systems of the body. Another area that is gaining more and more research and commercial interests is the use of EMI devices for drug delivery. Implantable drug infusion pumps are one example of such devices that have already been commercially available for pain management[19]. A number of electronic drug delivery implants are currently in various research and development satges, most of which capitalize on the strength of the microfabrication technology to enhance the capability and impact of drug delivery, as discussed below.

1.2 Microfabricated devices and systems for drug delivery

Microelectromechanical systems (MEMS) refer to the components or devices with minimum feature sizes on the order of micrometer range and with some level of integration between electronic and non-electronic function. Microfabrication, the technology to fabricate MEMS devices, uses a sequence of process steps (a process flow) — some borrowed from the integrated circuit (IC) and some developed specifically for MEMS — to create miniaturized objects[20, 21]. The diverse and flexible nature of MEMS technology promises a potentially wider range of applications than the IC field. The early stage of MEMS research and development were dominated by mechanical applications. Pressure sensors and airbag accelerometers in the automotive industry are two successful examples. The past several years have seen a rapid expansion of the MEMS field to biotechnology, environmental monitoring, industrial automation, IT and telecommunications, with the emergence of new commercial products such as Texas Instruments' Digital Micromirror Device and the I-STAT Point-of-Care blood analysis system.

Drug delivery remains a challenge in medicine although numerous polymer-based controlled drug delivery systems exist today[22, 23]. Most controlled release implants are capable of delivering only a single compound at a constant rate although it is well known

that the rate of a drug's delivery and its interactions with other chemicals have a significant influence on its effectiveness[24]. The digital capabilities and short response times of MEMS make them attractive for delivering pulses of endocrine hormones, which is difficult to achieve using the polymer implants[25]. Furthermore, the microfabrication technology is applicable to a wide variety of materials ranging from traditional silicon and glass to polymeric materials such as silicone rubber, polycarbonate, isobornyl acrylate and polyimide[26]. This allows the fabrication of novel drug delivery systems that integrate both hard and soft materials in order to achieve closed-loop self regulated delivery of drugs[27]. For example, hydrogels (a polymer that swells and deswells in response to changes in external environment such as temperature, pH, glucose level) and a polydimethylsiloxane (PDMS, also known as silicone rubber) membrane have been integrated into a silicon substrate to form a glucose sensitive microvalve that can be used for closed loop insulin delivery[28]. A more complex system that integrates a biosensor, batteries, and electroactive polymer for self regulating responsive delivery of insulin *in vivo*, is also being pursued by ChipRx[29].

A variety of microfabricated devices and components have been designed to release drugs of different dosages and with different delivery pattern and duration to address various clinical needs. Some recent review articles provide useful perspectives with comparison and contrast on their respective characteristics[30-35].

This thesis is focused on one microfabricated drug deliver device developed in this laboratory[36], as shown schematically in Figure 1.1. The device is based on a silicon substrate into which an array of reservoirs is etched. Each reservoir contains a single dose of drug and is covered with a gold membrane. The drug release is achieved by the application of a small anodic potential on the gold membrane in a chloride containing medium (such as the body fluid). The gold membrane will corrode and disintegrate so that the drug contained within the reservoir is free to diffuse into the surrounding medium.

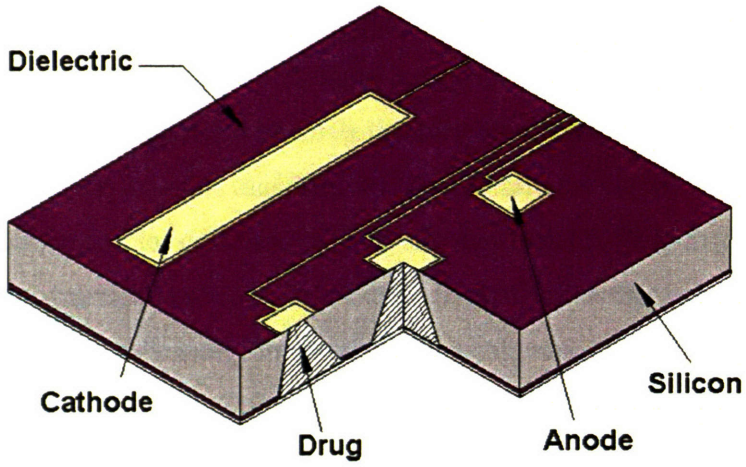

Figure 1.1 Schematic of the prototype drug delivery MEMS device developed in this laboratory[36].

Advantages of this drug delivery device over other existing devices include the variety of deliverable compounds, capability of complex release profiles, precise dosing, absence of moving parts, small size, and quick response time. Limitations include the small size of the microreservoirs and the need for surgical implantation and explantation. This kind of device may be particularly useful for the delivery of hormones, powerful painkillers, chemotherapeutic drugs, and other potent drugs. Besides delivering drugs, this device may also find potential applications in other fields such as medical diagnostics, chemical detection, industrial monitoring and control, combinational chemistry, microbiology, and fragrance delivery[37].

The initial successful demonstration of proof-of-principle release of single and multiple substances from a 17 mm square prototype device has stimulated research interest to further develop this technology. A new generation device was designed that uses the same electrochemical activation mechanism to achieve drug release but has a more compact design with 34 reservoirs on a 5 mm square device[38], as shown in Figure 1.2. This is also the device used throughout the study in this thesis.

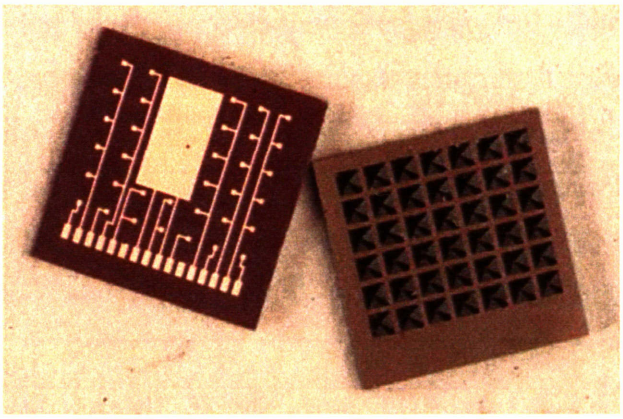

Figure 1.2 Photograph showing top and bottom of a drug delivery MEMS device used in this thesis. Photo taken by Rebecca Shawgo.

An important development has been the biocompatibility evaluation of the materials and voltammetry profiles for this drug delivery device in collaboration with Dr. James Anderson's group at Case Western Reserve University. All the materials used on this device were shown to be biocompatible[39]. The voltage application with activations up to five times and gold dissolution were found to induce an acute inflammatory response equivalent in magnitude to the initial implantation that was resolved within 72 hours[40, 41]. Further exploration of this drug delivery technology has led to development of a resorbable polymer based drug delivery device[42] and an impedance-based sensor for non-invasive real-time monitoring of drug release[43].

The first *in vivo* operation of the drug delivery device was demonstrated by the subcutaneous release of fluorescein dye in a rat flank model performed in collaboration with Dr. Henry Brem's group at Johns Hopkins Medical Institutions[38] (JHMI). The tissue section fluorimetry profiles shown in Figure 1.3 clearly demonstrate the superior capability of this MEMS device for achieving localized delivery.

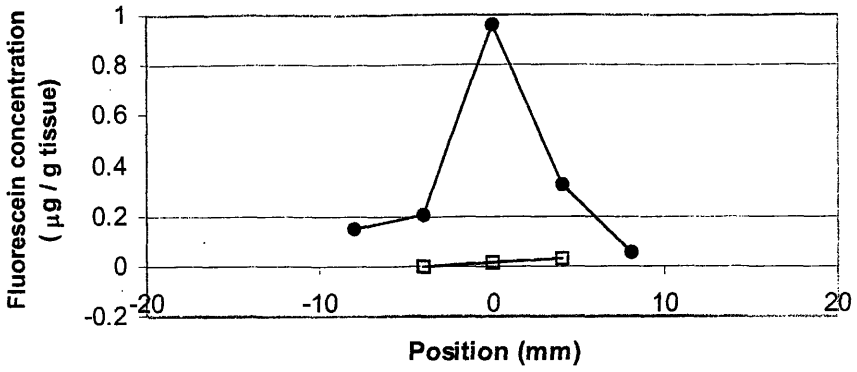

(a)

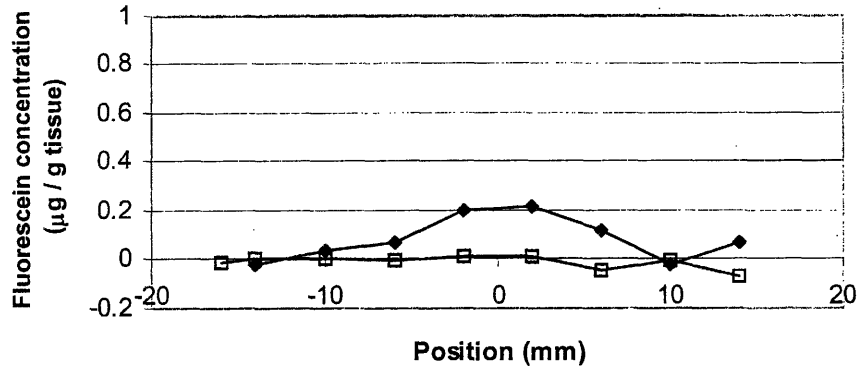

(b)

Figure 1.3 Spatial release profiles of fluorescent dye measured using spectrophotometry in tissue sections. Solid circles indicate data from the ipsilateral flank, and the open squares indicate data from the contralateral flank. Animals had (a) an activated device with 8 opened membranes, and (b) subcutaneously injected dye. Work completed by Rebecca Shawgo[38].

Local delivery is particularly important for many potent drugs that can cause serious side effects when delivered systemically at high concentration. One example of such drugs is BCNU, or carmustine, a chemotherapeutic drug. Its low molecular weight and high lipid solubility allows BCNU to easily cross the blood brain barrier and to be used for treatment of brain tumors[44]. Clinical use of BCNU is dose limited because high systemic concentration of BCNU causes extreme side effects affecting the liver, kidneys, and spleen[45]. Besides, BCNU has a short half-life both in plasma and within the brain when administered intravenously[46]. Biodegradable polymer wafers containing BCNU (Gliadel®) have been developed and approved by FDA for treatment of recurrent malignant glioma[47]. Local delivery of BCNU combined with other chemotherapeutic

agents, such as O^6-benzylguanine (O^6-BG), or immunotherapeutic agents, such as interleukin-2 (IL-2), can enhance the efficacy of BCNU therapy. Laboratory studies have indeed demonstrated improved survival on experimental tumor models[48, 49]. Effective delivery of the mutli-drug combination requires precise control of the temporal profiles of the agents, which is generally difficult to achieve using biodegradable polymers. The MEMS drug delivery device, on the other hand, will enable release of multiple compounds in complex release profiles to maintain drug concentrations within their therapeutic window. Therefore, the O^6-BG/BCNU or IL-2/BCNU combination therapy provides a suitable experimental paradigm for evaluating the efficacy of the drug delivery MEMS device.

Release of radiolabeled BCNU from the drug delivery device has been demonstrated *in vivo*[38]. However, the drug leakage problem and limitation of the radioactivity detection method made it difficult to extract accurate kinetics information of BCNU release *in vivo* and to further demonstrate efficacy of BCNU release in a flank tumor model. On the other hand, the gold membrane is the key functional component on this drug delivery device. Little was known about its mechanical properties, although it was realized that characterizing the mechanical integrity of the gold membranes was important for achieving robust and reliable performance of this MEMS device both *in vitro* and *in vivo*.

1.3 Thesis objectives

This thesis is focused on two aspects of study with different approaches. One is the characterization of the mechanical and electrochemical properties of the gold membranes using the materials science approach (processing-structure-properties). The other aspect of study, evaluation of the operation of the drug delivery device *in vivo*, will be performed in collaboration with Dr. Henry Brem's group at JHMI due to the multidisciplinary nature of the animal studies. However, these two aspects of study do not completely exclude one another since success of the device *in vivo* operation critically hinges on obtaining high quality gold membranes based on the mechanical and electrochemical characterization results. These two aspects of study will be implemented with the following specific objectives:

(1) To characterize the mechanical properties of gold membranes under different processing conditions (Chapter 2).

(2) To study the electrochemical disintegration process of gold membranes in chloride containing solutions (Chapter 3).

(3) To evaluate the BCNU release *in vitro* and to determine the influence of drug formulation and packaging method on the BCNU release kinetics (Chapter 4).

(4) To evaluate the release kinetics of ^{14}C labeled BCNU from the drug delivery device *in vivo* (Chapter 5).

(5) To demonstrate efficacy of BCNU released from the drug delivery device against the growth of an experimental tumor model (Chapter 6).

1.4 References

1. Hyman, A.S. Resuscitation of the stopped heart in intracardial therapy. II: Experimental use of an artificial pacemaker. *Archives of Internal Medicine* **50**, 283-305 (1932).
2. Elmqvist, R. and Senning, A. An implantable pacemaker for the heart, in C.N. Smyth (eds), *Proceedings of the Second International Conference on Medical Electronics*, Paris, France, pp. 253–254, (Iliffe & Sons, London, UK, 1959)
3. McWilliams, A. Microelectronic medical implants: products, technologies, and opportunities Business Communications Company, Inc., Norwalk, CT, 2004.
4. Glikson, M. and Hayes, D.L. Cardiac pacing: a review. *Medical clinics of North America* **85**, 369-421 (2001).
5. Hayes, D.L. Evolving indications for permanent pacing. *American journal of cardiology* **83**, 161D-165D (1999).
6. Saoudi, N., Appl, U., Anselme, F., Voglimacci, M. and Cribier, A. How smart should pacemakers Be? *American journal of cardiology* **83**, 180D-186D (1999).
7. Trohman, R.G., Kim, M.H. and Pinski, S.L. Cardiac pacing: the state of the art. *Lancet* **364**, 1701-1719 (2004).
8. DiMarco, J.P. Implantable cardioverter-defibrillators. *The New England Journal of Medicine* **349**, 1836-1847 (2003).
9. Groh, W.J., Foreman, L.D. and Zipes, D.P. Advances in the treatment of arrhythmias: implantable cardioverter-defibrillators. *American family physician* **57**, 297-307, 310-292 (1998).
10. Bhadra, N., Kilgore, K.L. and Peckham, P.H. Implanted stimulators for restoration of function in spinal cord injury. *Medical engineering & physics* **23**, 19-28 (2001).

11. Bajd, T., Kralj, A., Stefancic, M. and Lavrac, N. Use of functional electrical stimulation in the lower extremities of incomplete spinal cord injured patients. *Artificial organs* **23**, 403-409 (1999).

12. Sawan, M., Arabi, K. and Provost, B. Implantable volume monitor and miniaturized stimulator dedicated to bladder control. *Artificial organs* **21**, 219-222 (1997).

13. Rosenow Joshua, M., Mogilnert Alon, Y., Ahmed, A. and Rezai Ali, R. Deep brain stimulation for movement disorders. *Neurological research* **26**, 9-20 (2004).

14. Labar, D. and Dean, A. Neurostimulation therapy for epilepsy. *Current neurology and neuroscience reports* **2**, 357-364 (2002).

15. Lawson, D.T., Wilson, B.S., Zerbi, M., van den Honert, C., Finley, C.C., Farmer, J.C., Jr., McElveen, J.T., Jr. and Roush, P.A. Bilateral cochlear implants controlled by a single speech processor. *American Journal of Otology* **19**, 758-761 (1998).

16. Maniglia, A.J., Ko, W.H., Rosenbaum, M., Falk, T., Zhu, W.L., Frenz, N.W., Werning, J., Masin, J., Stein, A. and Sabri, A. Contactless semi-implantable electromagnetic middle ear device for the treatment of sensorineural hearing loss. Short-term and long-term animal experiments. *Otolaryngologic clinics of North America* **28**, 121-140 (1995).

17. Chow, A.Y., Chow, V.Y., Packo, K.H., Pollack, J.S., Peyman, G.A. and Schuchard, R. The artificial silicon retina microchip for the treatment of vision loss from retinitis pigmentosa. *Archives of ophthalmology* **122**, 460-469 (2004).

18. Margalit, E., Maia, M., Weiland James, D., Greenberg Robert, J., Fujii Gildo, Y., Torres, G., Piyathaisere Duke, V., O'Hearn Thomas, M., Liu, W., Lazzi, G., Dagnelie, G., Scribner Dean, A., de Juan, E., Jr. and Humayun Mark, S. Retinal prosthesis for the blind. *Survey of ophthalmology* **47**, 335-356 (2002).

19. Krames, E. Implantable technologies: spinal cord stimulation and implantable drug delivery systems, San Francisco, http://www.painconnection.org/myeducation/news_implantabletherapy.asp.

20. Spearing, S.M. Materials issues in microelectromechanical systems (MEMS). *Acta Materialia* **48**, 179-196 (2000).

21. Voldman, J., Gray, M.L. and Schmidt, M.A. Microfabrication in biology and medicine. *Annual Review of Biomedical Engineering* **1**, 401-425 (1999).

22. Langer, R. Drug delivery: drugs on target. *Science* **293**, 58-59 (2001).

23. Langer, R. and Peppas, N.A. Advances in biomaterials, drug delivery, and bionanotechnology. *AIChE Journal* **49**, 2990-3006 (2003).

24. Bakken, E.E. and Heruth, K. Temporal control of drugs: an engineering perspective. *Annals of the New York Academy of Sciences* **618**, 422-427 (1991).

25. Grayson, A.C.R., Shawgo, R.S., Johnson, A.M., Flynn, N.T., Li, Y., Cima, M.J. and Langer, R. A bioMEMS review: MEMS technology for physiologically integrated devices. *Proceedings of the IEEE* **92**, 6-21 (2004).

26. Whitesides, G.M., Ostuni, E., Takayama, S., Jiang, X. and Ingber, D.E. Soft lithography in biology and biochemistry. *Annual Review of Biomedical Engineering* **3**, 335-373 (2001).

27. Ziaie, B., Baldi, A., Lei, M., Gu, Y. and Siegel, R.A. Hard and soft micromachining for BioMEMS: review of techniques and examples of applications in microfluidics and drug delivery. *Advanced Drug Delivery Reviews* **56**, 145-172 (2004).

28. Baldi, A., Gu, Y., Loftness, P.E., Siegel, R.A. and Ziaie, B. A hydrogel-actuated environmentally sensitive microvalve for active flow control. *Journal of Microelectromechanical Systems* **12**, 613-621 (2003).

29. ChipRx. http://www.chiprx.com.

30. Prausnitz, M.R. Microneedles for transdermal drug delivery. *Advanced Drug Delivery Reviews* **56**, 581-587 (2004).

31. Razzacki, S.Z., Thwar Prasanna, K., Yang, M., Ugaz Victor, M. and Burns Mark, A. Integrated microsystems for controlled drug delivery. *Advanced Drug Delivery Reviews* **56**, 185-198 (2004).

32. Grayson, R.A.C., Shawgo, S.R., Li, Y. and Cima, M.J. Electronic MEMS for triggered delivery. *Advanced Drug Delivery Reviews* **56**, 173-184 (2004).

33. Shawgo, R.S., Richards Grayson, A.C., Li, Y. and Cima, M.J. BioMEMS for drug delivery. *Current Opinion in Solid State and Materials Science* **6**, 329-334 (2002).

34. Martin, F.J. and Grove, C. Microfabricated drug delivery systems: concepts to improve clinical benefit. *Biomedical Microdevices* **3**, 97-107 (2001).

35. Tao, S.L. and Desai, T.A. Microfabricated drug delivery systems: from particles to pores. *Advanced Drug Delivery Reviews* **55**, 315-328 (2003).

36. Santini, J.T., Jr., Cima, M.J. and Langer, R. A controlled-release microchip. *Nature (London)* **397**, 335-338 (1999).

37. Santini, J.T., Jr., Richards, A.C., Scheidt, R., Cima, M.J. and Langer, R. Microchips as controlled drug-delivery devices. *Angewandte Chemie, International Edition* **39**, 2396-2407 (2000).

38. Shawgo, R.S. *In vivo* activation and biocompatibility of a MEMS microreservoir drug delivery device, Ph.D. Thesis, Massachusetts Institute of Technology, 2004.

39. Voskerician, G., Shive, M.S., Shawgo, R.S., Recum, H.v., Anderson, J.M., Cima, M.J. and Langer, R. Biocompatibility and biofouling of MEMS drug delivery devices. *Biomaterials* **24**, 1959-1967 (2003).

40. Voskerician, G., Shawgo Rebecca, S., Hiltner, P.A., Anderson James, M., Cima Michael, J. and Langer, R. *In vivo* inflammatory and wound healing effects of gold electrode voltammetry for MEMS micro-reservoir drug delivery device. *IEEE Transactions on Bio-medical Engineering* **51**, 627-635 (2004).

41. Shawgo, R.S., Voskerician, G., Ho Duc, H.L., Li, Y., Lynn, A., Macewan, M., Langer, R., Anderson James, M. and Cima Michael, J. Repeated *in vivo* electrochemical activation and the biological effects of microelectromechanical

systems drug delivery device. *Journal of biomedical materials research* **71A**, 559-568 (2004).

42. Grayson, A.C.R., Choi, I.S., Tyler, B.M., Wang, P.P., Brem, H., Cima, M.J. and Langer, R. Multi-pulse drug delivery from a resorbable polymeric microchip device. *Nature Materials* **2**, 767-772 (2003).

43. Johnson, A.M., Sadoway, D.R., Cima, M.J. and Langer, R. Design and testing of an impedance-based sensor for monitoring drug delivery. *Journal of the Electrochemical Society*, In Press.

44. Barnhart, E.R. and Huff, B.B. Physicians' Desk Reference, Edition 48. (Medical Economics Company, Oradell, NJ; 1988).

45. Carter, S.K., Schabel, F.M., Jr., Broder, L. and Johnston, T.P. 1,3-Bis(2-chloroethyl)-1-nitrosourea (BCNU) and other nitrosoureas in cancer treatment. Review. *Advances in Cancer Research* **16**, 273-332 (1972).

46. Levin, V.A., Hoffman, W. and Weinkam, R.J. Pharmacokinetics of BCNU in man: a preliminary study of 20 patients. *Cancer treatment reports* **62**, 1305-1312 (1978).

47. Brem, H., Piantadosi, S., Burger, P.C., Walker, M., Selker, R., Vick, N.A., Black, K., Sisti, M., Brem, S. and Mohr, G. Placebo-controlled trial of safety and efficacy of intraoperative controlled delivery by biodegradable polymers of chemotherapy for recurrent gliomas. The Polymer-brain Tumor Treatment Group. *Lancet* **345**, 1008-1012 (1995).

48. Rhines, L.D., Sampath, P., Dolan, M.E., Tyler, B.M., Brem, H. and Weingart, J. O6-benzylguanine potentiates the antitumor effect of locally delivered carmustine against an intracranial rat glioma. *Cancer Research* **60**, 6307-6310 (2000).

49. Rhines, L.D., Sampath, P., DiMeco, F., Lawson, C.H., Tyler, B.M., Hanes, J., Olivi, A. and Brem, H. Local immunotherapy with interleukin-2 delivered from biodegradable polymer microspheres combined with interstitial chemotherapy: a novel treatment for experimental malignant glioma. *Neurosurgery* **52**, 872-879 (2003).

2 Mechanical testing on gold membranes

2.1 Introduction and motivation

Like any other MEMS devices, this drug delivery device must have enough mechanical stability to ensure robust and reliable performance. Knowing the mechanical properties of the materials involved is therefore important. Specifically, the mechanical integrity of the gold membranes is critically important for the proper function of the device. The gold membranes need to be strong to survive the chemical filling, packaging and surgical implantation. Moreover, the drug release from the device depends on the gold membrane disintegration upon the application of voltage, which includes both mechanical and electrochemical components, as will be discussed in detail in Chapter 3. It is therefore desirable to characterize the mechanical properties of gold membranes on this drug delivery device and to understand these properties are affected by different processing conditions.

The gold membrane on the drug delivery device is essentially a free standing thin film. There has been long-lasting research interest in the mechanical properties of thin films motivated not only by purely scientific curiosities, but more importantly by their application in a wide variety of microelectronic and MEMS devices and systems. Although in many cases thin films are selected mainly for their electronic, magnetic, or optical characteristics, understanding their mechanical properties is equally important[1]. In order for the devices to function reliably, they must have structural integrity to withstand the mechanical and chemical forces that arise in their applications. The trend towards miniaturization and integration in MEMS requires decreases in film thickness and increases in number of layers. This poses thermal and mechanical compatibility problems and necessitates a good understanding of the mechanical properties of the thin film materials.

This chapter first briefly reviews literature on the mechanical testing of free standing thin films. The bulge test, a well established mechanical testing method, was used in our study to measure the mechanical properties of the gold membranes on this drug delivery device and to study their dependence on the film in-plane size and processing conditions.

2.2 Review of mechanical testing on free standing thin films

It is known that the physical properties of thin films are often different from those of their bulk counterparts. One reason is due to the larger surface to volume ratio in thin films, leading to a larger role of surfaces and interfaces in governing materials properties[2]. For example, the often-observed enhanced yield strength in thin films is related to the more constrained dislocation motion. Furthermore, thin film preparation techniques, such as evaporation, sputtering, chemical vapor deposition, sol-gel, etc, are quite different from those used for bulk materials, such as molding, sintering and casting. The microstructures of thin films are often far from non-equilibrium and are highly dependent on the deposition and post-processing methods, which leads to a further divergence in materials properties.

Measuring the mechanical properties of bulk materials is usually straightforward and there are standards (such as the ASTM standards) specifying the methods and the specimen dimensions for measuring the property of interest. This is however not possible for thin film materials in MEMS. Many new methods have been developed applicable to the micron scale materials testing. Table 2.1 lists some commonly used techniques in measuring the mechanical properties of free standing thin films.

Table 2.1 Techniques for measuring mechanical properties of free standing thin films[3-6].

Techniques	Properties measured	Advantages	Disadvantages
Tensile test	Elastic and plastic properties, creep, fracture	Ease of test data interpretation	Difficulty in sample preparation, sensitivity to edge effects
Bulge test/ Blister test	Elastic properties/ Plastic properties	Simple test setup, insensitivity to edge effects	Difficulty in test data interpretation
Acoustic method	Elastic properties	Measurement of anisotropy in elastic constants	Unable to probe large strain phenomenon

The bulge test was chosen for the mechanical testing of the gold membranes on the drug delivery device because some of the current packaging components can be readily used to construct the pressurizing unit. One unique feature of our test is that the

gold membrane is part of the MEMS device so that the test result is directly applicable to predicting the mechanical behavior of the membrane in actual service. This is different from any other reported bulge test study where the test structure is non-integrated and the test is conducted purely for the sake of obtaining the materials properties. On the other hand, the multiple microfabrication process steps involved in the device fabrication could cause non-idealities in the gold membrane structure and hence affect its properties, as will be discussed in the section below.

In the bulge test, uniform pressure is applied from one side of a free standing thin-film "window", causing it to deflect to the other side (see Fig. 2.1). The stress and strain in the film can be obtained from measuring the pressure and film deflection. The bulge test for thin films was first used by Beams in 1958[7]. After over 30 years of continuous refinement and modification in film preparation, modeling, testing and data analysis, the accuracy and reproducibility of the bulge test have been greatly improved. A brief summary below is helpful for us to correctly conduct the test and interpret the results.

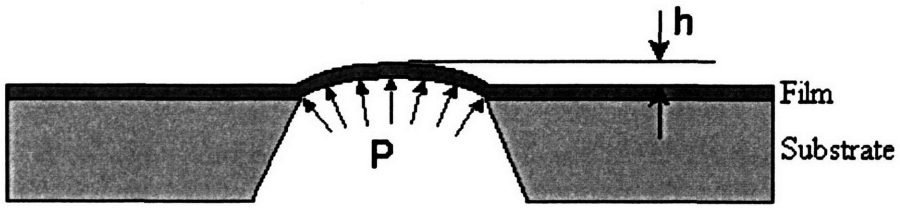

Figure 2.1 Schematic showing principle of the bulge test.

(1) Film preparation

Early studies used thin films evaporated on a dissolvable substrate, either a sodium chloride (NaCl) crystal or a plastic film glued on the end of a copper tube[8]. The main problem with this method is the uncertainty in the film in-plane dimension. The action of clamping the film over an orifice changed the initial stress state of the film. All this resulted in large scatter in the measured property data. Use of the silicon bulk micromachining technique has fundamentally solved the problem of sample preparation. The anisotropic etching produces perfectly square or rectangular membranes on silicon substrates that can be readily tested.

(2) Modeling

Modeling of the deformation behavior of the pressurized film is needed to translate the experimentally determined pressure-deflection relation into the stress-strain relation to extract the elastic modulus. A spherical bulge was initially assumed, which was found to be inconsistent with the constraints imposed by the attachment of the film to the substrate[8]. Later work using energy minimization and/or finite element modeling gives a generalized form for the bulge test[5, 6, 9-11]:

$$P = c_1 \frac{\sigma_0 t}{a^2} h + c_2 \frac{M t}{a^4} h^3 \qquad \text{(Equation 2.1)}$$

where P is pressure, σ_0 is the residual stress, t and a are film thickness and radius, h is the center deflection, ν is the Poisson ratio, M is the biaxial elastic modulus, $M = \frac{E}{1-\nu}$, and E is the Young's modulus. c_1 and c_2 are constants dependent on the film geometry, as listed in Table 2.2.

Table 2.2 Parameters for generalized bulge equation.

Film geometry	c_1	c_2	**Method**
Circular	4	$\frac{8(1.015-0.247\nu)}{3}$	Numerical approximation to Hencky's exact solution[5]
Circular	4	$\frac{7-\nu}{3}$	Energy minimization[10]
Circular	4	$\frac{2.67}{1.026+0.233\nu}$	Finite element simulation[9]
Square	3.41	1.981-0.585ν	Finite element simulation[9]
Square	3.393	1.996-0.613ν	Energy minimization[11]
Long rectangular	2	$\frac{4}{3(1+\nu)}$	Exact solution, plane strain stress state[5]

For square membranes, the two sets of available constants derived from different methods are very close. The set of constants derived from the energy minimization method (c_1=3.393, c_2=1.996-0.613ν) will be used in our study because it is more recent than the other set and its applicability has been supported by many experimental studies[12-14]. Fitting the experimental data with Equation 2.1 allows the extraction of not only the elastic modulus E (or the biaxial modulus M), but also the residual stress σ_0 in

the film. Excellent agreement has been reported between the extracted modulus using Equation 2.1 and that measured using other techniques from independent research groups.

It should be noted that the derivation of Equation 2.1 is based on the assumption that the bending stiffness of the membrane can be neglected. This is true for conventional bulge tests that use thin films with millimeter in plane dimension and submicron thickness. The importance of bending stiffness is determined by a dimensionless number $(E/\sigma_0)\cdot(t/a)^2$. The bending stiffness can be safely neglected if this number is small (for example, $<10^{-2}$). The in plane dimension of the gold membranes on our drug delivery devices is in the micron scale ($a \approx 30\mu m$), resulting in a non-negligible bending stiffness ($(E/\sigma_0)\cdot(t/a)^2 \approx 10^{-2}$). A revised bulge equation should be used[11]:

$$P = \left(c_1 \frac{\sigma_0 t}{a^2} + c_1' \frac{Et^3}{(1-\nu^2)a^4} \right) h + c_2 \frac{Et}{(1-\nu)a^4} h^3 \qquad \text{(Equation 2.2)}$$

where c_1' is the bending stiffness coefficient, $c_1' = 4$ for square membranes.

Another caution when using the generalized bulge equation is that the residual stress in the film has to be tensile. The compressive stress causes the film to buckle or wrinkle. Finite element calculations have shown that the circumferential stress near the edge of the film remains compressive even under large applied pressure, resulting in meaningless measurement[15]. One way to overcome this problem is to deposit the film onto another film with tensile stress to give a composite structure with positive value of

$$(\sigma_0 t)_{equivalent} = \sum_i \sigma_{0i} t_i \qquad \text{(Equation 2.3a)}$$

Here the multilayered film is treated by taking weighted average of the properties of individual films, therefore

$$(Mt)_{equivalent} = \sum_i \frac{E_i t_i}{1-\nu_i} \qquad \text{(Equation 2.3b)}$$

where i designates the ith layer of the composite structure. The multiplayer can then be bulge tested and the properties of the material under study can be extracted from the composite behavior using the known property data of the other layer material[16].

2.3 Experimental methods

2.3.1 Fabrication of free standing gold thin films

As mentioned in the previous section, one unique feature of our bulge test is that it is an integrated test performed on a real device rather than on a test structure. Fig. 2.2 shows the process steps to fabricate the drug delivery device, as briefly introduced below. Unless otherwise noted, all processing steps were performed in the Technology Research Laboratory (TRL), a Class 100 cleanroom (defined as "less than 100 particles larger than 0.5 microns in each cubic foot of air space") in the Microsystems Technology Laboratory (MTL) at MIT.

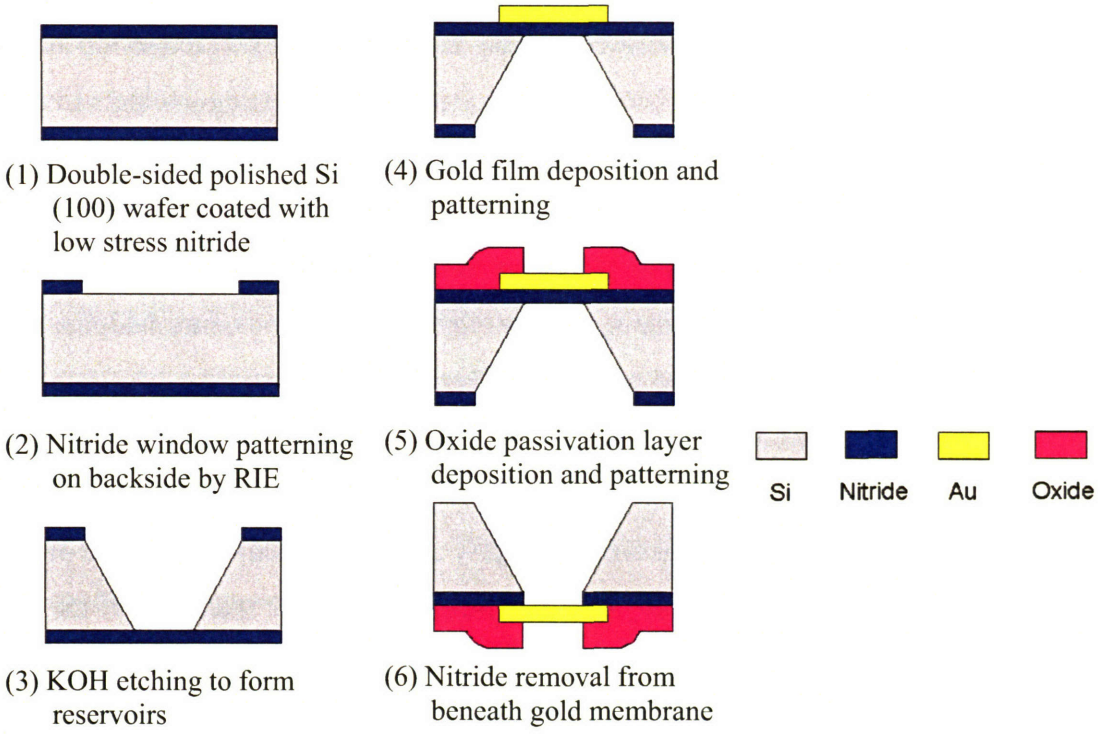

Figure 2.2 Microfabrication process flow of the drug delivery MEMS device.

(1) A 4″, double sided polished Si wafer (Wafernet Inc., San Jose, CA) was deposited with 2000 Å silicon nitride films on both sides in a vertical tube reactor (VTR – SVG/Thermco 7000 Series, San Jose, CA) by staff, with the following processing parameters: 250 sccm Dichlorosilane (SiH_2Cl_2) and 25 sccm Ammonia (NH_3), 250 mTorr pressure and 775°C. This gave a non-stoichiometric silicon rich nitride film nearly stress free and with a refractive index of 2.25. Low stress nitride is desirable in that relatively

thick films can be deposited and patterned without delamination or cracking. It also acts as a good mask against potassium hydroxide (KOH) etching with negligible etching rate. The absence of pin holes in the low stress nitride greatly decreased the chance of forming etch pits in deep and long KOH etching, thus retaining the wafer integrity and increasing the device yield.

(2) The nitride on one side of the Si wafer was patterned to define the large opening (480 x 480 μm) of the microreservoirs. Positive photoresist (OCG 825, Arch Chemicals, Norwalk, CT) was spin coated on the wafer, soft baked at 90 °C for 30 minutes, patterned on a mask aligner (EV 620, EV Group Inc., Tempe, AZ) under 365~405 nm UV exposure system, developed in OCG 934 1:1 developer, and hard baked at 120 °C for 30 minutes. The exposed nitride was removed by reactive ion etching (PlasmaQuest Series II Reactor Model 145), using the following recipe: 15 sccm Tetrafluormethane (CF_4), 15 sccm Helium (He) and 2 sccm Oxygen (O_2), 20 mtorr process pressure, 100 W electron cyclotron resonance (ECR) microwave power, 20 W Radio Frequency (RF) power, and 25 °C chamber temperature. The nitride etching rate was monitored by optical interferometry on NanoSpec (Nanometrics, Inc., Milpitas, CA). Non-uniform etching was observed across the 4″ wafer with the center usually etching faster than the corners by 0.02~0.15 Å/sec.

(3) The wafer was then soaked in a KOH bath (20% by weight) at 85°C. It is well known that the etching of Si in KOH is highly anisotropic and the etch rate of (100) and (110) crystal planes can be two orders of magnitude higher than that of the (111) plane. As a result, square pyramidal shaped reservoirs were formed after the KOH etching. The Si etching rate was about 1μm/min in our process. The etching greatly slowed down (about 0.5 Å/min) upon reaching the nitride on the other side of the wafer. This allows accommodation of the thickness non-uniformity across the entire wafer. The resulting small opening of the reservoirs had dimension around 50 x 50 μm. The wafers after KOH etching must be thoroughly cleaned to remove the K^+ contamination before any further process in TRL. The post-KOH cleaning included a 10-minute piranha etching (a mixture of sulfuric acid and hydrogen peroxide at 3:1 volume ratio), rinse, another 10-minute piranha etching, spin rinse dry, and 1-minute dip in hydrofluoric acid (HF) diluted in deionized H_2O (at 1: 50 volume ratio).

(4) The gold film was then deposited and electrodes patterned on the other side of the wafer. Two physical vapor deposition methods, evaporation and sputtering, were used to deposit the gold film. The corresponding gold electrode patterning method was also different:

A process called lift-off was used to pattern the evaporated gold film. An image reversal photoresist (AZ 5214E, Clariant) was first spin coated onto the surface of the wafer having the nitride film covering the reservoirs, soft baked at 90 °C for 30 minutes, exposed under EV 620 mask aligner, hard baked at 105 °C for 30 minutes, flood exposed without a mask for 1 minute, and developed in developer (AZ 422 MIF, Clariant). The patterned wafer was then placed in an electron beam evaporator (Temescal Semiconductor Products Model VES 2550, Fairfield, CA) for the gold film deposition. The chamber was pumped down to a vacuum of about 7×10^{-7} torr, followed by deposition of 100 Å thick titanium (Ti) layer to promote the adhesion of the gold film to the silicon nitride. A 3000 Å thick gold film was then deposited on top of the Ti layer. Both the Ti and Au films were deposited at a rate of 1 Å/sec. The wafer was then soaked in acetone for about half an hour to "lift off" the metals deposited on top of the photoresist, leaving the areas where the metal films were deposited directly onto the nitride (the electrode pattern and bond pads) intact.

The gold film on some wafers was deposited using sputtering by an outside vendor (Lance Goddard Associates, Foster City, CA) in a Class 100 cleanroom. An MRC 903 sputter system was used that utilized a linear scan underneath fixed sputtering targets. The system was pumped to $2.5 \sim 4 \times 10^{-7}$ torr. Ar was bled in to 10 mtorr pressure to sputter clean the wafer surface for 30 seconds at 0.5 W/cm^2 power. A 100 Å thick chromium (Cr) film was immediately sputter deposited as adhesion layer at 0.67 kW DC and a scan rate of about 30 in/min, followed by deposition of 3000 Å thick gold film at 2.5 kW DC with a scan rate of about 8 in/min. The wafer was at room temperature at the beginning of the sputtering process with the main heating coming from bombardment of the surface by the depositing Au atoms, and the wafer temperature did not exceed 90 °C throughout the process. Positive photoresist (OCG 825) was spin coated onto the wafer surface with the gold film, soft baked at 90 °C for 30 minutes, patterned on the EV 620 mask aligner, developed and hard baked at 120 °C for 30 minutes. The

exposed gold areas were removed by wet etching in an iodine-based gold etchant (TFA, Transene Company Inc., Danvers, MA) at about 28 Å/second etching rate. The wafer was then dipped in a Cr etchant (CR-7, Cyantek Inc., Fremont, CA) briefly (approximately 10 seconds) to etch the exposed Cr. The different gold film deposition conditions led to different film microstructure, which could affect its properties, as discussed in Section 2.4.2.

(5) A 6000 Å thick silicon dioxide (SiO_2) layer was deposited on top of the gold layer to passivate some portions of the gold electrode (trace). Key requirements for the SiO_2 are good adhesion to the gold, and *in vivo* stability and biocompatibility. The deposition technique of SiO_2 is also limited to low temperature processing (< 350 °C) since high temperature can lead to thermal grooving and void formation in gold films, as reported in literature[17, 18] as well as shown in our own test (see Figure 2.3). These defects can cause premature leakage of the drugs contained in the microreservoirs and affect the device operation reliability.

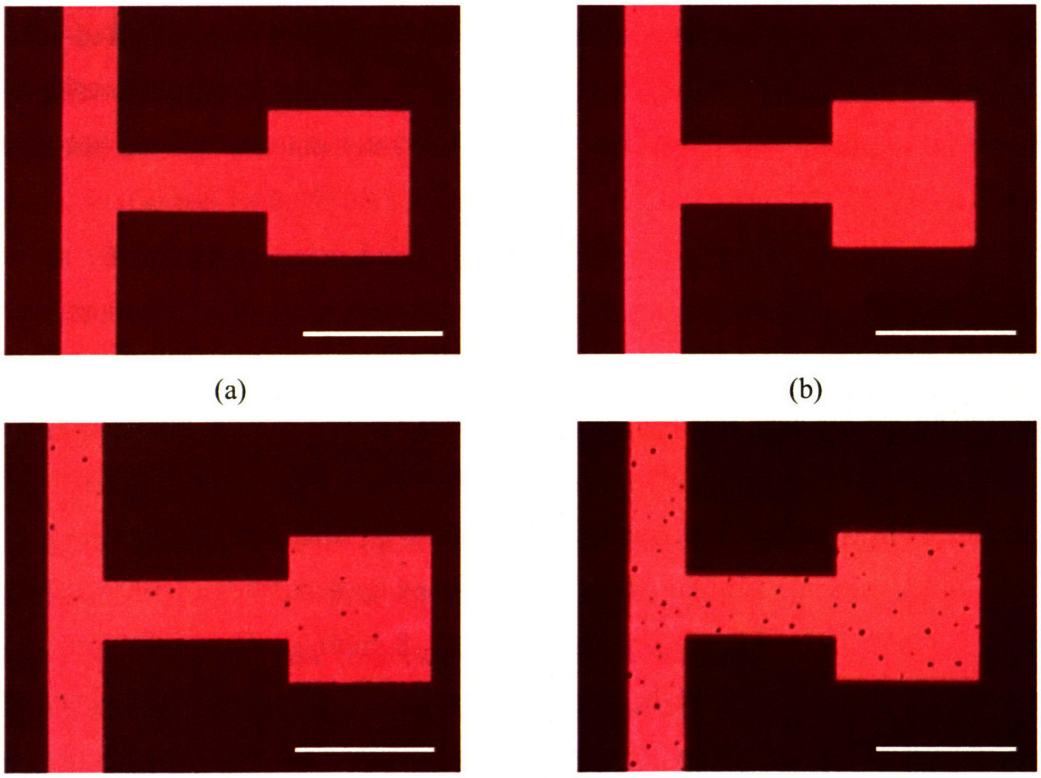

Figure 2.3 Optical micrographs of evaporated gold films. (a) as-deposited, and annealed at (b) 300°C/4h, (c) 300°C/8h, (d) 350°C/1h. Scale bar is 100 μm.

Plasma enhanced chemical vapor deposition (PECVD) at 300°C was chosen for the oxide deposition either on a dual chamber PECVD/RIE system (700 Series, PlasmaTherm Inc., Kresson, NJ) or by an outside vendor (Strataglass, Mountain View, CA). The PlasmaTherm system is located in the Exploratory Materials Laboratory (EML), which is a low level cleanroom without tight control of the particulate count in the environment. Wafers processed in EML were not allowed to return to the TRL. The subsequent oxide patterning and nitride etching had to be processed in EML, which could negatively affect the device yield. The oxide deposition by Strataglass, on the other hand, was performed in a Class 100 cleanroom. Therefore, wafers could continue to be processed in TRL after the oxide deposition.

Prior to the oxide deposition on the PlasmaTherm, a 100 Å Ti was evaporated on top of the gold layer and patterned to promote the adhesion between the gold and oxide. The processing parameters for the oxide deposition were: 600 sccm Silane (SiH_4, 5% diluted in He) and 250 sccm Nitrous Oxide (N_2O), 500 mtorr pressure, 25 V DC controlled RF, and 300 °C chamber temperature. Positive photoresist (OCG 825) was spin coated onto the wafer surface with the oxide layer, soft baked at 90 °C for 30 minutes, patterned on a contact mask aligner (Karl Suss MJB-3, Suss MicroTec Inc., Waterbury Center, VT), developed and hard baked at 120 °C for 30 minutes. The exposed oxide was removed by RIE on the PlasmaTherm using the following recipe: 20 sccm CF_4 and 5 sccm O_2, 20 mtorr pressure, 300 V DC controlled RF, and 25 °C chamber temperature. Wafers with oxide deposited by Strataglass were patterned in TRL on the EV 620 mask aligner. The exposed oxide was removed by RIE on the PlasmaQuest using the following recipe: 15 sccm CF_4, 15 sccm He, 20 mtorr process pressure, 100 W ECR microwave power, 10 W RF power, and 25 °C chamber temperature.

The PlasmaTherm oxide had a refractive index of 1.47, which is slightly different from that deposited by Strataglass (1.55). Nevertheless, both types of oxide films exhibited excellent adhesion to the gold electrode in the Scotch tape test. The Scotch adhesive tape was applied to the device over the oxide dielectric layer and then peeled off. No lift-off of the oxide or gold was observed. Moreover, after *in vitro* activation of

the devices in the phosphate buffered saline (PBS) solution, no sign of corrosion was observed on the traces under the microscope.

(6) The last microfabrication step was to remove the silicon nitride beneath the gold electrode membranes using RIE on the PlasmaTherm (for wafers with the oxide deposited on PlasmaTherm) or on the PlasmaQuest (for wafers with the oxide deposited by Strataglass). The wafer was first diced into 5 × 5 mm individual devices on a diesaw (DAD-2H/6T, Disco Hi-Tec America, Inc., Santa Clara, CA). A 1 μm thick positive photoresist layer was spin coated onto the wafer surface to protect the gold membranes from the cooling water jet. Devices were cleaned in nanostrip (Cyantek Inc., Fremont, CA) and placed on top of a 4″ test wafer in groups of 20 or less. The electrode side of the devices was in contact with the test wafer to expose the nitride membranes to the plasma. The nitride etching recipe on the PlasmaTherm was: 45 sccm Trifluoromethane (CHF_3), 5 sccm O_2, 300 V DC controlled RF, 30 mtorr pressure, and 25 °C chamber temperature. The same nitride etching recipe in Step (2) was used to etch the nitride on the PlasmaQuest. However, much longer time (2~2.5 times that needed to etch the same thickness on a test wafer) was used to completely remove the nitride at the bottom of the reservoirs due to transport limitations within the confined space. The difficulty to measure the nitride etching rate in the reservoir made it difficult to evaluate this backside etching process and know whether the nitride had been completely removed using conventional methods. The bulge test has been shown to be an effective non-destructive method to evaluate this nitride etching process, as discussed in Section 2.4.3.

Free standing gold films with different in-plane sizes can be obtained by changing the nitride window size in Step (2). Unless otherwise noted, Step (5) was omitted when fabricating the devices bulge tested in this chapter. The absence of oxide from these devices simplified the fabrication process and more importantly eliminated possibility of measurement error under the optical profiler due to the difference in the refractive index between oxide and gold.

2.3.2 Bulge test apparatus

The bulge test apparatus is shown in Figure 2.4. Compressed air from a gas tank was regulated by a mini valve and a relief valve (not shown in the figure) to pressurize the gold membranes on a device placed on a pressurizing unit (Figure 2.4b). Two stainless steel frames and a silicone gasket (with a 3 mm hole cut in the center) were readily used in this unit. The thickness of the bottom frame (450 μm, MicroPhoto, Roseville, MI) is slightly smaller than the total thickness of the device (350 μm) and gasket (125 μm, Advanced Bio-Technologies, Inc., Silverdale, WA) so that the gasket could be compressed against the device bottom to form a seal by tightening nuts and bolts (# 000-120, Small Parts Inc., Miami Lakes, FL) using a torque screw driver (Model TT-1, Cooper Power Tools, Hicksville, OH). A Wyko NT 2000 non-contact optical profiler (Veeco Instruments Inc., Tucson, AZ) was used to measure the profile of the deflected membrane.

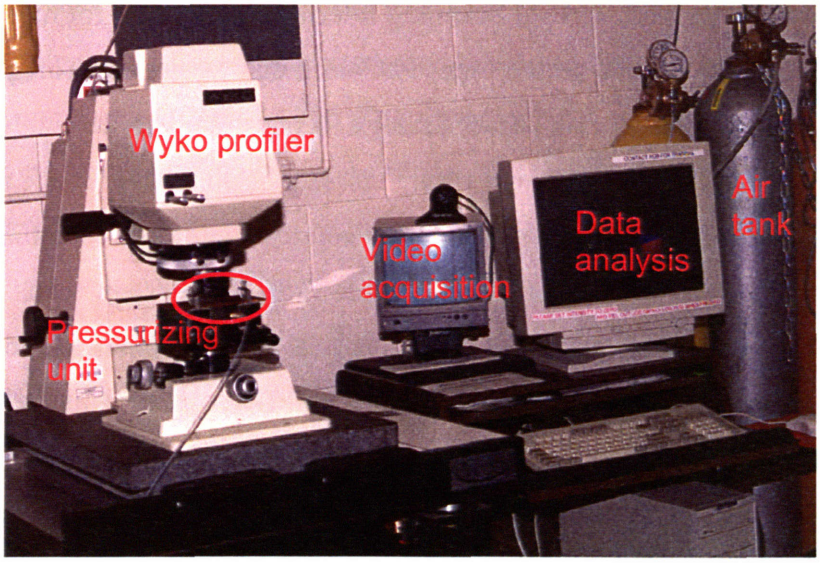

(a)

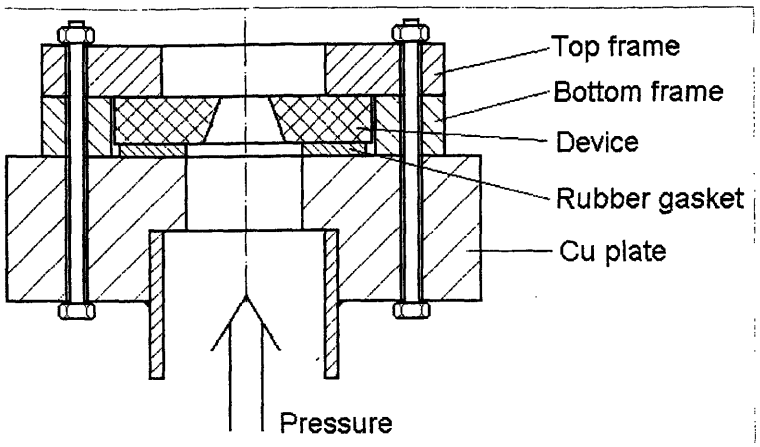

(b)

Figure 2.4 (a) Photograph showing the bulge test apparatus, and (b) Cross section of the pressurizing unit (not drawn to scale).

There are two measurement techniques for the Wyko profiler: Phase Shifting Interferometry (PSI) for sub-nanometer resolution measurement of smooth surfaces with steps less than 160nm, and Vertical Scanning Interferometry (VSI) for measuring rougher surfaces and steps up to several mm high. The basic interferometric principles are similar in both techniques: A light beam passes through an interferometer objective to the sample surface. A beam splitter reflects half of the incident beam to a reference mirror surface. The beams reflected from the sample and the reference surface recombine at the beam splitter to form interference fringes (see Figure 2.5). The system scans through focus (starting above focus) at evenly spaced intervals as the camera captures frames of interference data. The analysis unit of the system uses advanced computer algorithms to resolve the surface height profile. One big difference between the VSI and PSI techniques is that in VSI, the white-light source is not filtered, and the system measures the degree of fringe modulation, or coherence, instead of the phase of the interference fringes as in the PSI mode. The VSI mode (with a vertical resolution of 3 nm) was used to measure the bulged profile of gold membranes in this chapter.

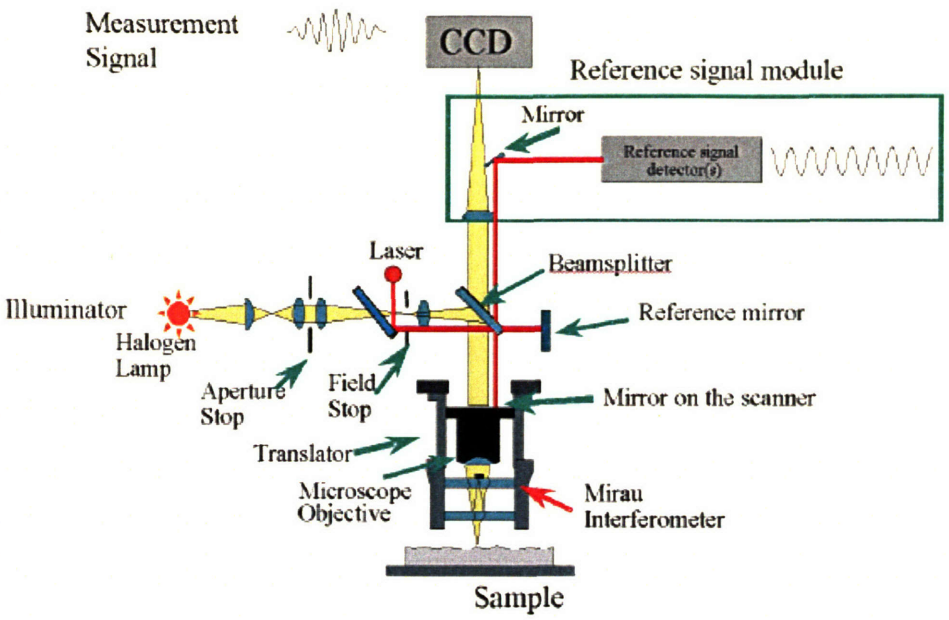

Figure 2.5 Interferometric principle of the Wyko profiler[19].

2.3.3 Data analysis

In the bulge test, pressure was gradually applied to the gold membrane from 0 psi, stopped at every 5 psi (1 psi = 6895 Pa) increment for the profile of the deformed membranes to be recorded. After reaching 60 psi, the pressure was slowly decreased at 5 or 10 psi interval by careful control of the relief valve. The profile of the depressurized membranes was also recorded. The profile acquisition and analysis was performed using Vision 32, a software accessory to the Wyko profiler.

Figure 2.6a shows an example of the raw measurement dataset of a gold membrane under 60 psi pressure recorded by Vision 32. A terms mask was first defined that assumed the subregions excluding the electrode and trace to be of the same height level. This terms mask was then activated to remove the linear tilt from the measurement. Of the various post-processing options available in Vision 32, the 2D analysis is the most useful in that the membrane center deflection can be directly obtained (see Figure 2.6b). All the deflection data in this Chapter were taken from the gold film center relative to a reference point 200 μm away on the trace.

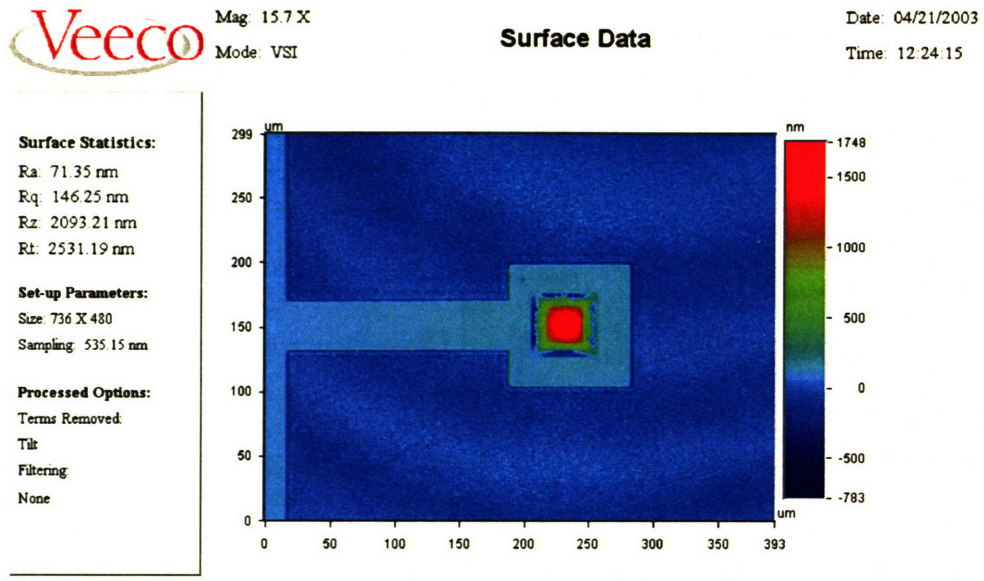

Title: D40-E3-P60
Note: P=60 psi

(a)

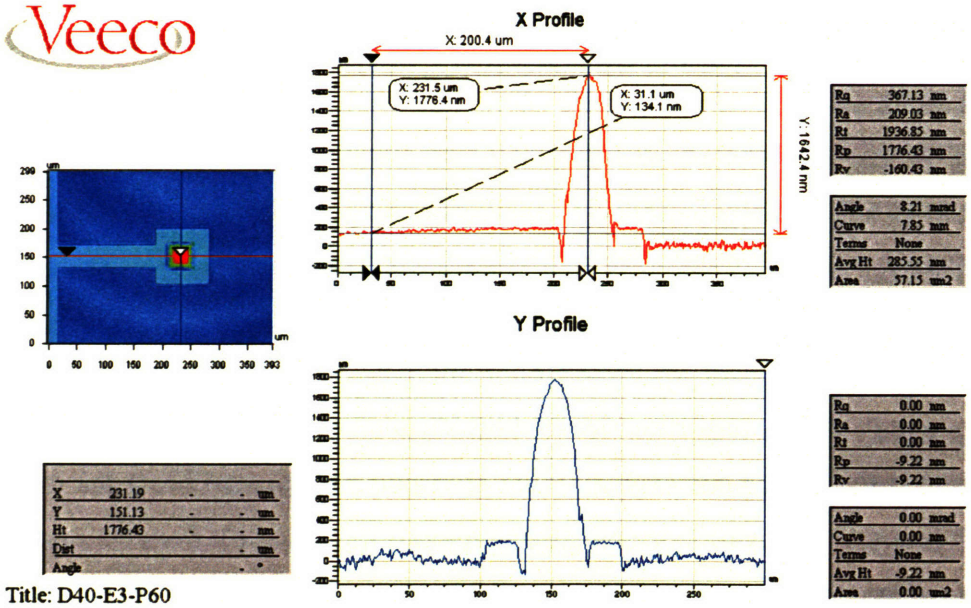

Title: D40-E3-P60
Note: P=60 psi

(b)

Figure 2.6 (a) Raw dataset and (b) 2D profile of a deformed gold membrane under 60 psi pressure.

The 3D interactive plot is another appealing feature of the software, which gives vivid three-dimensional representation of the deformed gold membranes, as illustrated in Figure 2.7.

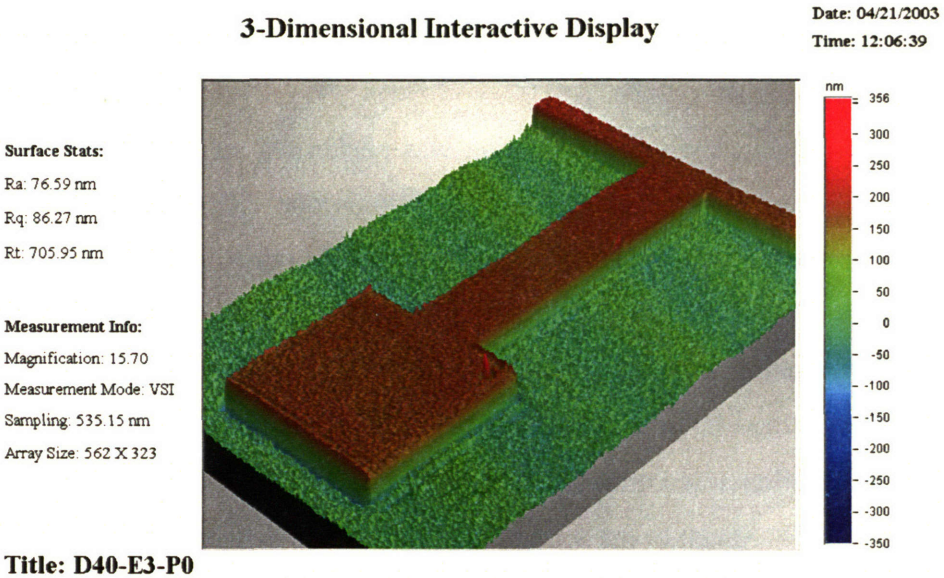

(a)

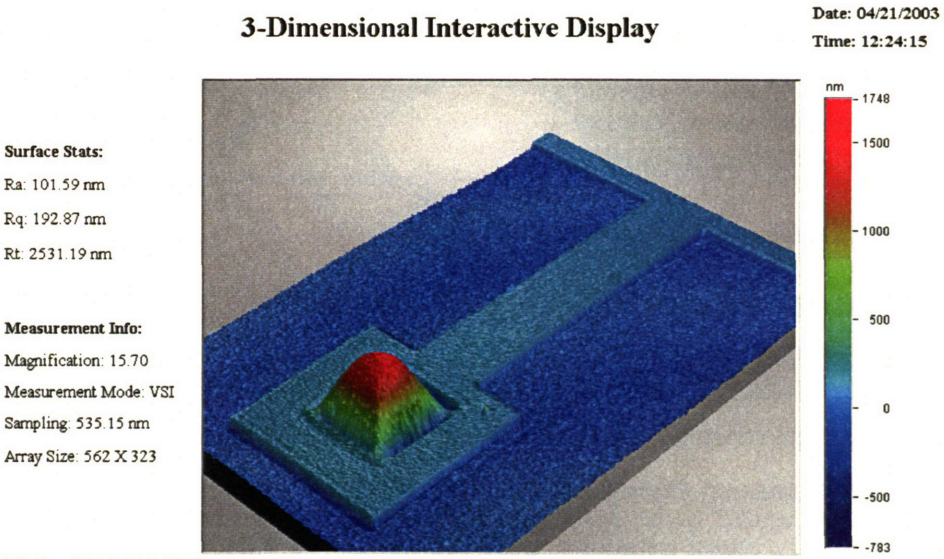

(b)

Figure 2.7 3D plots of a gold membrane (a) with no pressure being applied and (b) under 60 psi pressure.

2.3.4 Microstructural characterization

Besides the Wyko profiler, other characterization tools were used to reveal the microstructural characteristics of the gold membranes, which not only helped to explain the bulge test results, but also served as useful guidance for the optimization of gold membrane processing conditions.

The optical microscopy observation was performed on an Olympus microscope (BH-2). A field emission scanning electron microscope (Hitachi 4700) was used to observe the in-plane grain structure of the gold membranes. A transparent sheet was overlaid on the printed SEM image so that the grains could be identified by tracing the grain boundaries using a marker. The resulting overlay was scanned to form a digital image, which can then be analyzed using the UTHSCSA ImageTool program (Version 3.0). X-ray diffraction was conducted on a Rigagu D/Max diffractometer using Cu K_α radiation to obtain the membrane texture information. A Tencor contact surface profiler (P10, KLA-Tencor, Milpitas, CA) was used to measure the deposited gold film thickness and to compare with the measurement by the Wyko profiler. The surface morphology of gold membranes was also observed by atomic force microscopy (AFM) under a Nanoscope III Multimode AFM system (Veeco Instruments Inc., Tucson, AZ).

2.4 Results and discussion

2.4.1 Evaporated gold membranes

2.4.1.1 Elastic deformation

Figure 2.8 shows the center deflection of two gold membranes in three pressurizing-depressurizing cycles. As expected, both membranes showed increased deflection with increasing pressure. Depressurizing led to an almost identical path back to the initial state. The good coincidence of the deflection data in the three pressurizing-depressurizing cycles indicated elastic deformation behavior of the two gold membranes up to 60 psi pressure.

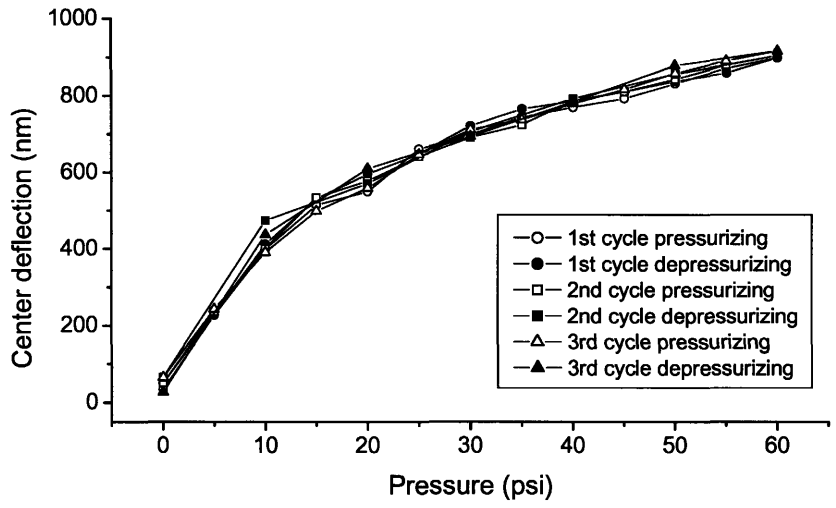

(a)

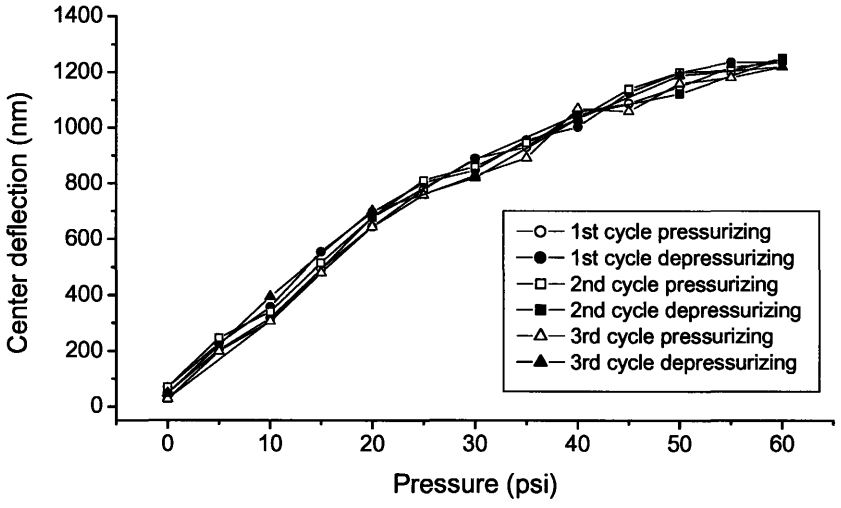

(b)

Figure 2.8 Center deflection of two gold membranes in three pressurizing-depressurizing cycles. The in-plane sizes of the two membranes measured under the optical microscope were (a) 36.6 μm and (b) 54.3 μm.

A revised equation from Equation 2.2 was used when fitting the experimentally measured data:

$$P = P_0 + P_1 h + P_2 h^3 \qquad \text{(Equation 2.4)}$$

The fitting parameter P_0 was introduced to account for the pressure and deflection offset errors, which led to a non-zero deflection at zero pressure. The thickness of the gold membrane was measured by the contact profiler to be 2500 Å, which was lower than

the target value (3000 Å). It was later found out that full calibration for the TRL e-beam equipment was not achieved at the time of film deposition. XRD analysis showed a strong (111) texture in the evaporated gold film (see Figure 2.9). Therefore, the calculated Poisson ratio for (111) textured gold ($\nu_{(111)} = 0.571$ [3]) was used to extract the residual stress and elastic modulus, as listed in Table 2.3.

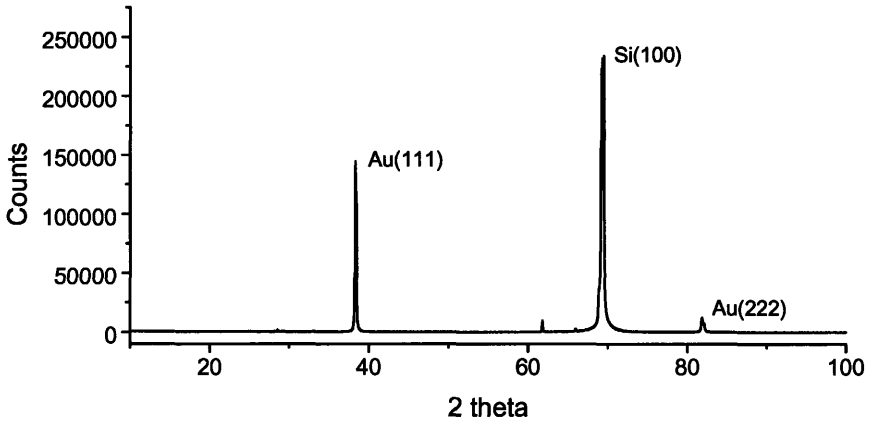

Figure 2.9 XRD spectrum on the drug delivery MEMS device, showing strong (111) texture of the gold membranes.

Table 2.3 Bulge test curve fitting and extracted mechanical properties for two gold membranes.

Membrane in-plane size (μm)		**36.6**	**54.3**
Curve fitting results	P_0	0.65±1.19	-0.26±1.05
	P_1	7.81±3.52	24.06±2.45
	P_2	72.22±3.69	14.50±1.38
	R^2	0.993	0.992
Biaxial modulus M (GPa)		148 ± 8	143 ± 14
Residual stress σ_0 (MPa)		23 ± 10	157 ±16

The coefficients of determination (R^2) for both membranes were very close to 1, indicating good fitting of the experimental data to the bulge equation. The extracted modulus for the two membranes was about 23% lower than the theoretical modulus for (111) single crystal gold (189GPa[20]). However, similar amount of lowering in modulus has been reported in other researchers' tests on free standing gold films or other metal films[3, 13, 21]. It is intuitively obvious that the lowering of the thin film stiffness should be related with its non-equilibrium microstructure. Some models have been proposed

attempting to correlate thin film microstructural features such as texture[22], voids[22], grain boundary compliance[23, 24], microcracking[22, 25], or dislocation movement[26, 27], to the measured lower moduli. However, no consensus explanation has been achieved and the exact mechanism for the lowered stiffness in thin films remains unclear.

2.4.1.2 Plastic deformation

Figure 2.10 shows the center deflection vs. pressure curves for three gold membranes with larger in-plane size. The large deviation of the membrane center deflection between the pressurizing segment and the depressurizing segment indicates that plastic deformation occurred. Moreover, the membrane with 215.7 μm in-plane size ruptured before pressure was increased to 30 psi.

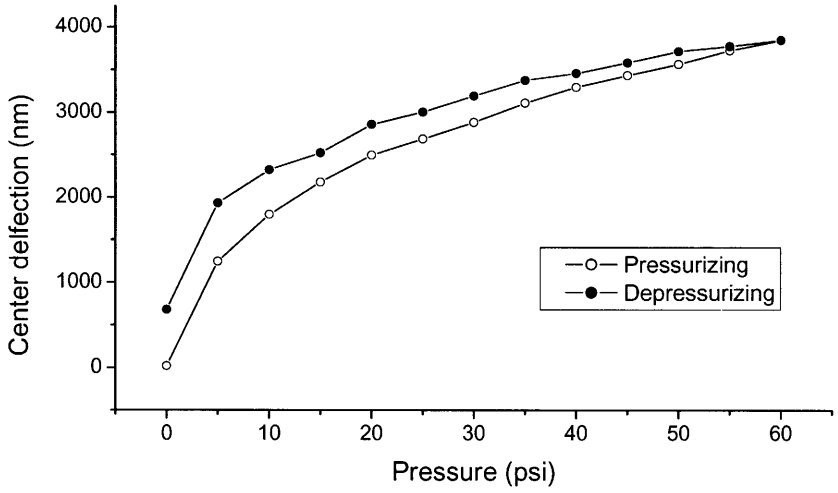

(a)

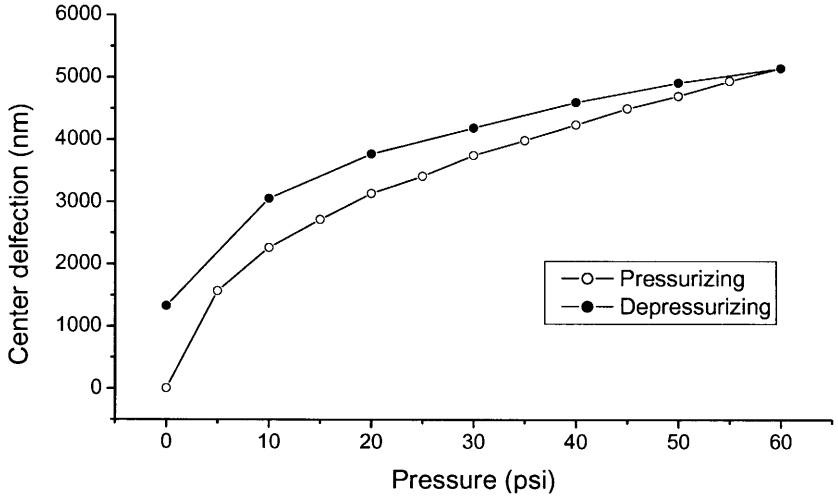

(b)

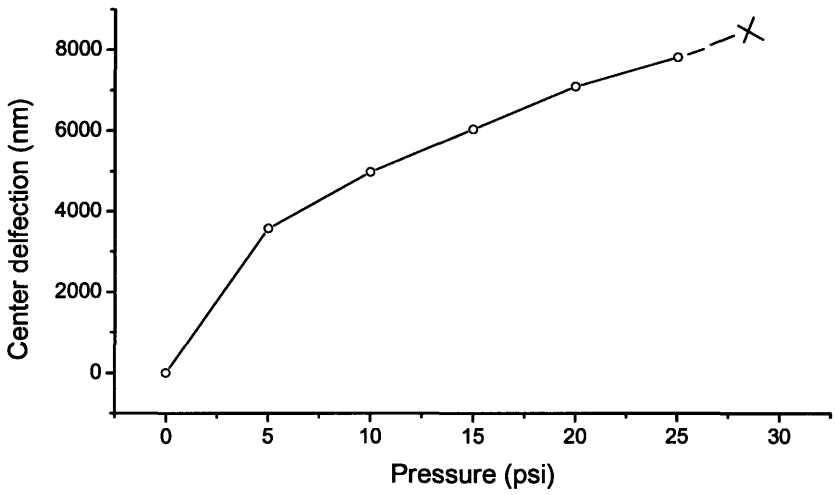

(c)

Figure 2.10 Center deflection vs. pressure for three gold membranes with in-plane sizes of (a) 100.9 μm, (b) 127.2 μm, and (c) 219.7 μm.

The free standing square film has a non-uniform stress state under the application of pressure, with biaxial stress state in the film center and plane strain stress state towards the film edge. If we rewrite Equation 2.1 as:

$$\frac{Pa^2}{c_1 ht} = M\left[\frac{c_2}{c_1}\frac{h^2}{a^2}\right] + \sigma_0 \qquad \text{(Equation 2.5)}$$

where $c_1 = 3.393$, $c_2 = 1.966 - 0.613\nu$ for square membranes, we can use Equation 2.5 to estimate the stress in the membrane under a given pressure:

$$\sigma = \frac{Pa^2}{3.393ht} \qquad \text{(Equation 2.6)}$$

The gold membrane yield strength σ_y, therefore, can be obtained by comparing the stress of the two membranes (with 54.3 μm and 100.9 μm in-plane sizes respectively) at 60 psi pressure, and the fracture strength σ_f estimated using the deflection data of the 219.7 μm membrane under 25 psi pressure:

$$317\ MPa < \sigma_y < 351\ MPa \qquad \text{(Equation 2.7a)}$$

$$\sigma_f \approx 340\ MPa \qquad \text{(Equation 2.7b)}$$

The gold membranes on the drug delivery device showed significantly higher strength than the bulk gold (See Table 2.4). This is not surprising, as similar strengthening phenomena have been reported not only for the gold thin films, but also for a number of other thin film systems[28-32]. The non-equilibrium microstructure of thin films, notably the small grain size and large surface/volume ratio, is generally believed to be correlated with the enhanced strength in thin films. There have been extensive studies to investigate the deformation and strengthening behavior of thin films. Many models, such as grain boundary strengthening, dislocation interaction strengthening, film thickness and texture effect, have been proposed[14, 33, 34]. A systematic experimental study on the stress-strain relationship of gold membranes supplemented with careful microstructural observation and modeling, though beyond the scope of this thesis' objectives, may be necessary to fully understand the strengthening mechanism. For example, a long rectangular membrane is more suitable than a square membrane in studying the stress-strain relationship. The stress state in a long rectangular membrane approaches that of plane strain[13], making it straightforward to analyze both elastic and plastic deformation of the membrane. Change of the testing strain rate and temperature, and detailed microstructural analysis on the kinetics of dislocation motion, may provide useful insight into the deformation and strengthening behavior of thin films.

Table 2.4 Mechanical properties of bulk gold[20].

Condition	Yield strength (MPa)	Tensile strength (MPa)
Cast	N/A	125
Wrought, annealed	N/A	130
Work hardened	205	220

2.4.1.3 Gold/nitride composite membranes

To circumvent the plastic deformation of gold membranes with larger in-plane sizes, gold/nitride composite membranes were bulge tested. Figure 2.11 shows the deflection vs. pressure curves for five composite membranes with in-plane sizes ranging from 25.4 μm to 215.7 μm. The presence of the stiff nitride strengthened the gold

membranes, leading to only elastic deformation behavior up to 60 psi pressure for all the samples tested.

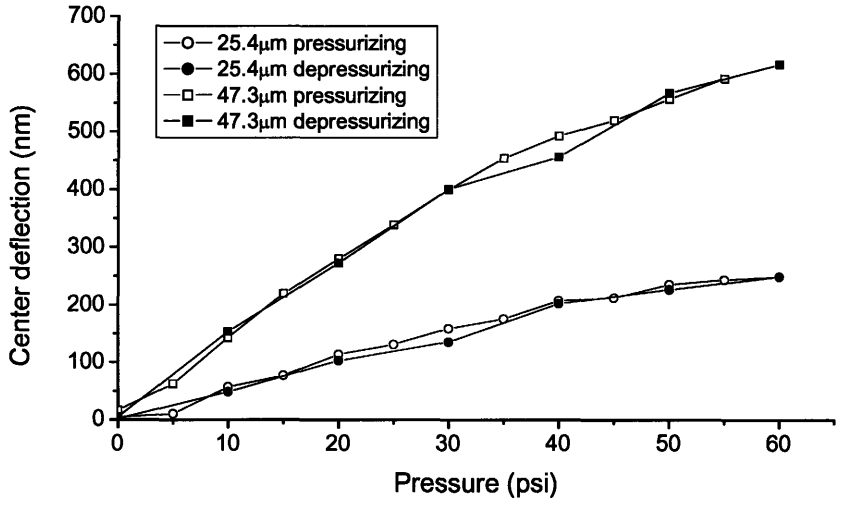

(a)

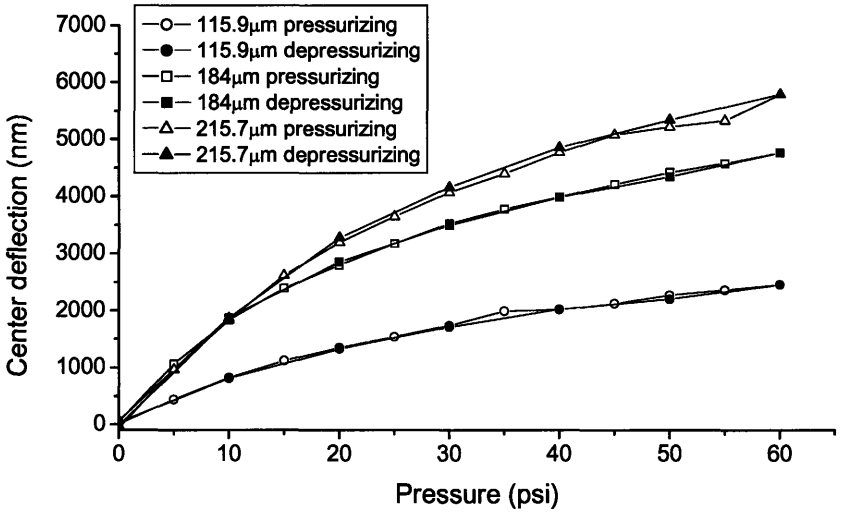

(b)

Figure 2.11 Center deflection of gold/nitride composite membranes (a) with smaller in-plane size and (b) with larger in-plane size in a pressurizing-depressurizing cycle.

Equation 2.2 and 2.3 were used to fit the curves in Figure 2.11. The modulus and Poisson's ratio of nitride were taken to be 250 GPa and 0.23 respectively[35]. The nitride thickness after the KOH etching was measured to be 2032 Å, and its residual stress was

measured by wafer curvature to be 180 MPa. The extracted gold membrane properties from curve fitting results are shown in Table 2.5.

Table 2.5 Mechanical properties of evaporated gold membranes extracted from bulge test on gold/nitride composite membranes.

Membrane in-plane size (μm)	**25.4**	**47.3**	**115.9**	**184**	**215.7**
Biaxial modulus (GPa)	126 ±108	145 ±48	144 ±29	168 ±12	146 ±23
Residual stress (MPa)	69 ±21	151 ±17	152 ±28	140 ±15	259 ±43

The extracted gold membrane properties from the gold/nitride composite systems were comparable to those from pure gold membranes, indicating good applicability of the bulge test analytical solutions to the gold membranes with much smaller in-plane sizes. The narrow range of the biaxial modulus suggested that the modulus was probably independent of the membrane in-plane sizes.

It is also noted that the extracted property data showed relatively larger error than those from pure gold membranes, especially for composite membranes with smaller in-plane sizes. This is most probably a result of experimental error in the measurement of deflection and pressure values, which becomes more significant for films with smaller in-plane sizes because of the much smaller total deflection of the membrane. Another contributing factor is the neglect of the very thin Ti adhesion layer (approximately 100 Å thick) between nitride and gold when applying the bulge equation to the composite membranes mainly due to unavailability of the property data of this Ti layer.

2.4.2 Sputtered gold membranes

Two gold membranes deposited by sputtering were also bulge tested and the deflection vs. pressure data were plotted in Figure 2.12. Both membranes had relatively small in-plane sizes, and exhibited only elastic deformation up to 60 psi pressure. Table 2.6 lists the extracted mechanical properties for the two membranes according to Equation 2.2:

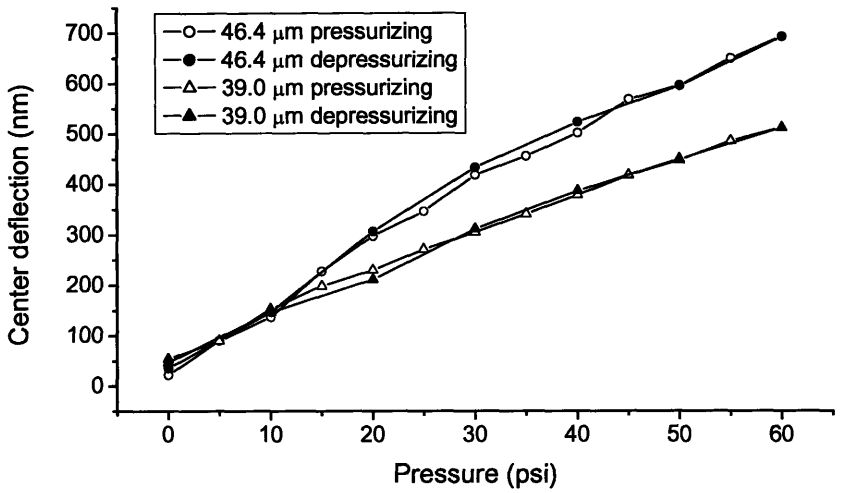

Figure 2.12 Center deflection of two sputtered gold membranes under one pressurizing-depressurizing cycle.

Table 2.6 Mechanical properties of sputtered gold membranes extracted from bulge test.

Membrane in-plane size (μm)	**46.4**	**39.0**
Biaxial modulus (GPa)	157 ± 23	149 ± 27
Residual stress (MPa)	257 ± 11	283 ± 10

The two sputtered membranes showed slightly higher modulus and residual stress than the evaporated gold membranes with comparable in-plane sizes. Although the result is not statistically conclusive due to the small difference in the modulus value and limited number of sputtered samples tested, it is not surprising that gold membranes fabricated under different processing conditions exhibited differences in the microstructure and mechanical properties.

Schematics of the evaporation and DC sputter deposition equipments are shown in Figure 2.13. In evaporation, the source material is heated in a vacuum chamber by electron beam, giving off evaporated atoms that travel along "line-of-sight" and condense onto the substrate surface. In contrast, the DC sputter deposition uses a parallel plate arrangement, with the target placed on the cathode and the substrate on the anode. An inert gas, such as argon (Ar), is introduced into the chamber at low pressure. A voltage applied across the two electrodes creates plasma and ionizes Ar, which is accelerated to the target and dislodge, or sputter the target atoms. These atoms then travel through the plasma and strike the surface of the substrate to form a film. Although both evaporation

and sputtering are physical vapor deposition techniques, the difference in the generation of depositing atoms between these two processes leads to different structural characteristics of the resulting films, as summarized in Table 2.7.

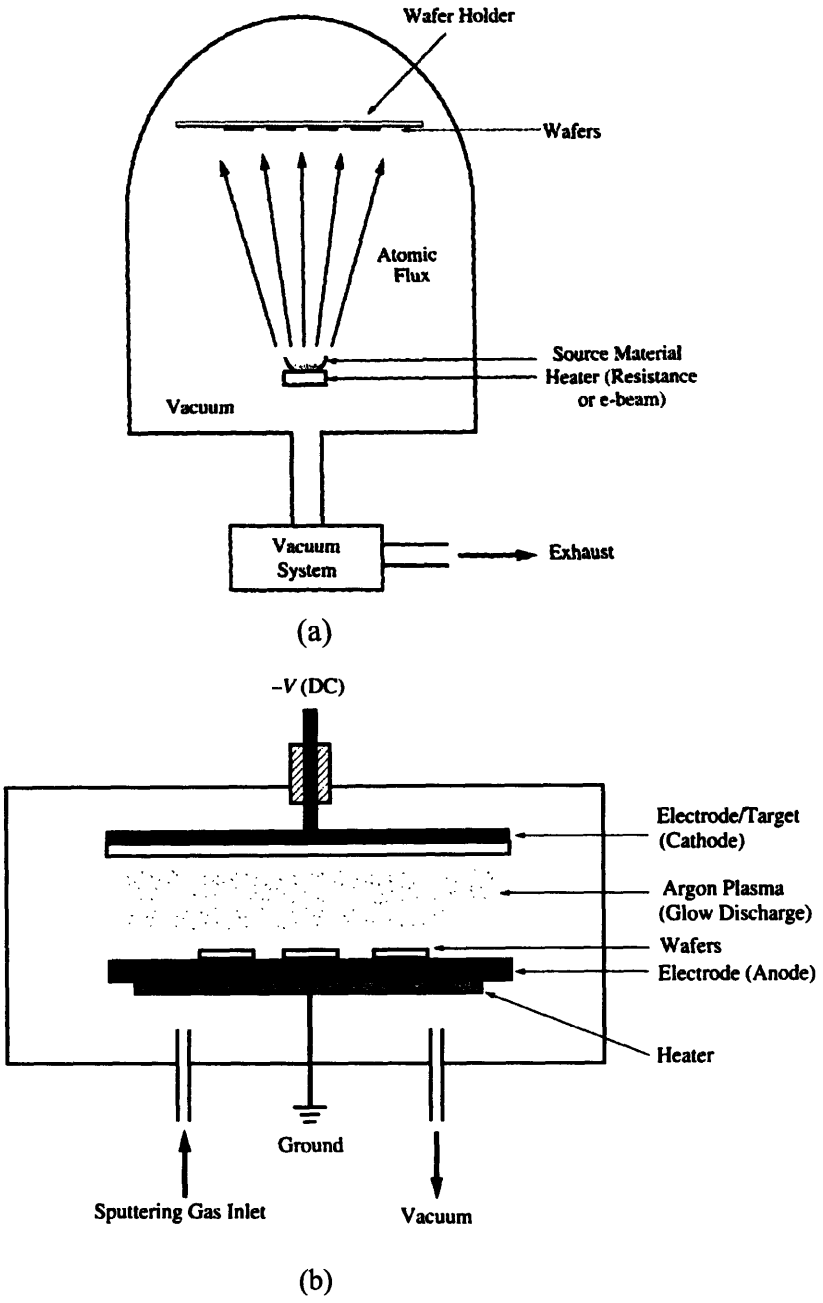

Figure 2.13 Schematics of (a) an electron beam evaporator and (b) a DC sputter deposition equipment. Redrawn after Plummer[36].

Table 2.7 Comparison of evaporation and sputter deposition techniques[37, 38].

	Evaporation	**Sputter deposition**
Mechanism of atom removal	Thermal evaporation (hot source)	Ion Bombardment and collisional momentum transfer (cool target)
Pressure	High-ultrahigh (~10^{-5} to 10^{-10} torr)	Low-medium (~1 to 100 mtorr)
Species energy	~ 0.1 to 0.2 eV for evaporants	3 to 10 eV for sputtered atoms
Atomic mean free path	Larger than source-substrate spacing	Less than target-substrate spacing
In situ cleaning	Not an option	Easily done with a sputter etch
Adhesion	Often poor	Excellent
Uniformity	Difficult	Easy over large areas
Surface damage	Very low	Ionic bombardment damage
Film purity	Better	Possibility of incorporating impurities

Figure 2.14 shows the SEM micrographs of the top surface (perpendicular to the film thickness direction) of evaporated and sputtered gold films. Both films show cellular like in-plane grain morphology, and the sputtered film has slightly more rounded grains (roundness 0.72) than the evaporated film (roundness 0.69). According to Thornton's zone model[39], gold films are expected to exhibit columnar grain structure in the thickness direction due to the relatively high mobility of gold atoms[40]. Gold has a low hardness and tends to smear when being polished, making it difficult to obtain good quality SEM cross section images. Nevertheless, transmission electron microscopy (TEM) and scanning tunneling microscopy (STM) examinations on gold films deposited using similar conditions as in our study have confirmed the columnar grain structure[41, 42].

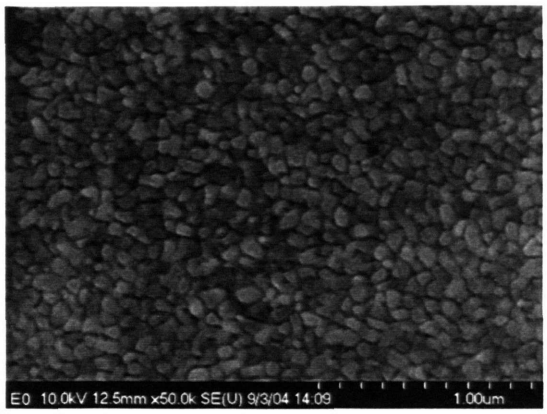

(a)

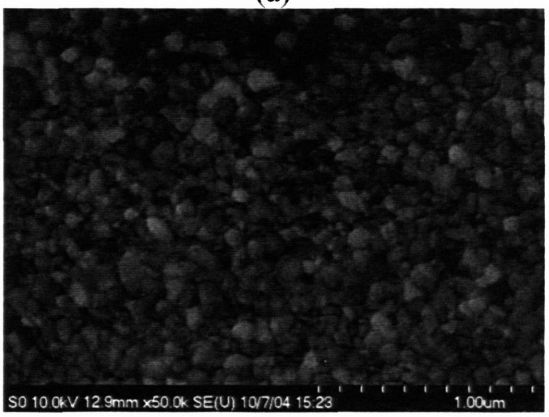

(b)

Figure 2.14 SEM micrographs of top surface of gold films deposited by (a) evaporation (thickness 2500 Å) and (b) sputtering (thickness 3000 Å).

Figure 2.15 shows the image analysis result for the two types of gold films. The average in-plane grain size for the evaporated gold film is 75 nm (standard deviation 18 nm), comparing to 66 nm (standard deviation 27 nm) for the sputtered gold film. The sputtered film also showed a wider spread in the 2D grain size distribution. The atoms that arrive on the sputtered surface are more energetic than those arrive on the evaporated surface, and hence have higher surface diffusivity. The bombardment of the sputtered atoms to the substrate surface leads to increase of the surface temperature, which also helps to enhance the mobility of depositing atoms. All these factors may have contributed to a denser film by sputtering than by evaporation. Phenomenologically, this result also seems to agree with one principle in the packing theory, which states that the fraction of voids in packed particulate materials decreases with increasing width of particle size distribution[43].

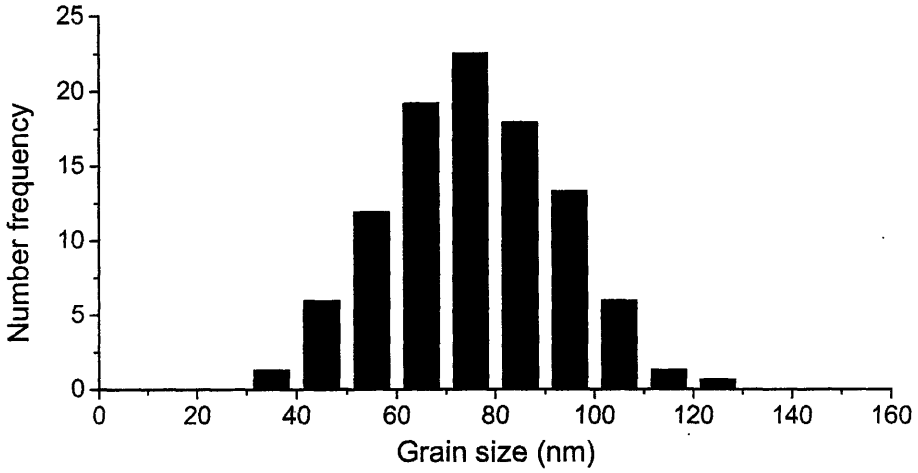

(a)

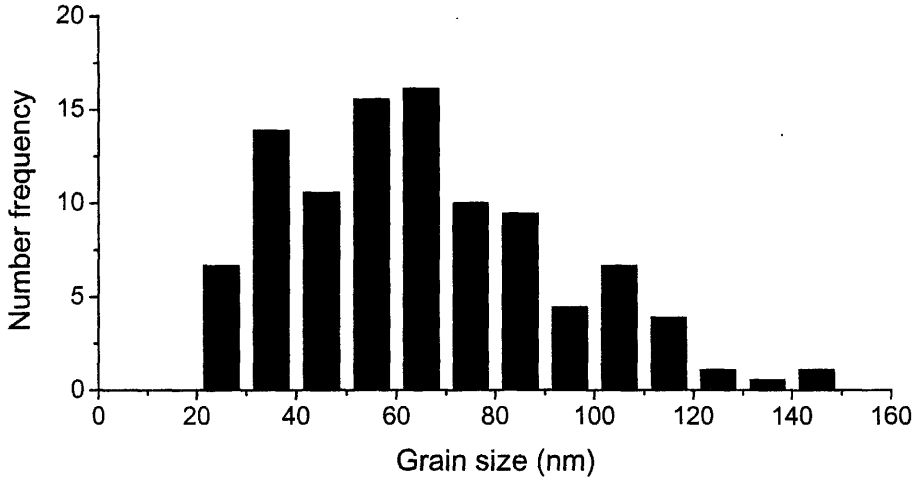

(b)

Figure 2.15 In-plane grain size distribution of gold films deposited by (a) evaporation (N=151 grains, thickness 2500 Å) and (b) sputtering (N= 180 grains, thickness 3000 Å).

Surface morphology comparison of the two types of films by AFM (see Figure 2.16) indicated that both films were very smooth, with the sputtered film having slightly lower root-mean-square (RMS) roughness (1.80 nm) than the evaporated gold film (2.56 nm). The RMS roughness measured by the Wyko profiler was around 6 nm for both types of films. The difference could be due to the fact that a much larger area was measured (30 × 30 μm) by the optical profiler than by the AFM (1 × 1 μm).

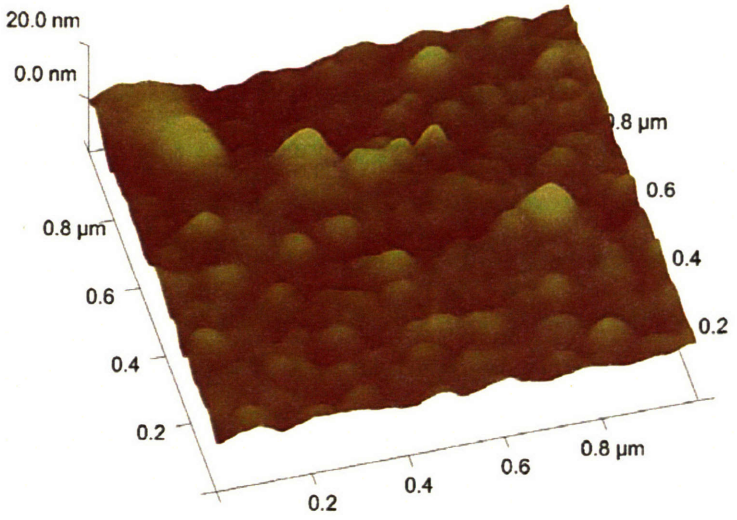

(a)

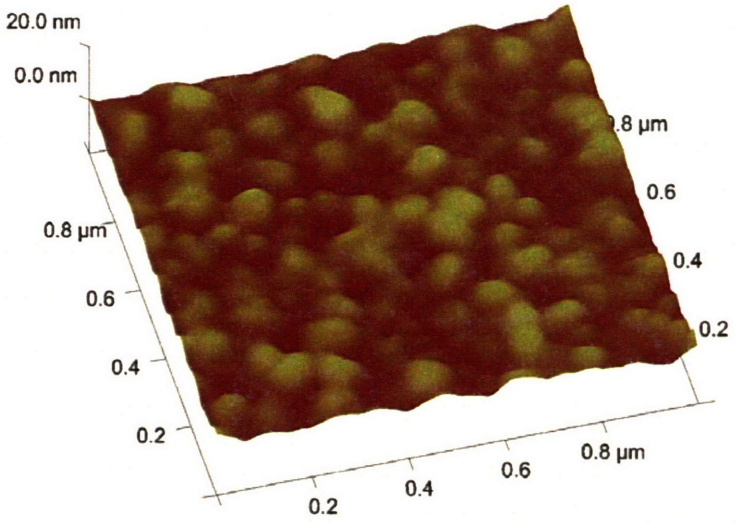

(b)

Figure 2.16 AFM surface morphology of gold films deposited by (a) evaporation (thickness 2500 Å) and (b) sputtering (thickness 3000 Å).

As mentioned in the device fabrication section (2.3.1), gold electrodes deposited by evaporation were patterned using the lift-off process. The multiples photoresist processing steps before the gold film deposition increased possibility of contamination by photoresist residues or other particles on the patterned wafer, even though great care was taken to minimize contamination in the lithography step and a short (1 minute) oxygen plasma etching (TRL asher) was also used just before putting the wafer into the e-beam

chamber. The particles could become origin of defects in the gold film, which can lead to premature leakage of chemicals (especially those of low molecular weight) contained in the reservoirs. In contrast, a wet etching process was used to pattern the sputtered gold film. The wafer was thoroughly cleaned in Nanostrip (a mixture of sulfuric acid and hydrogen peroxide) before it was placed into the sputtering chamber. Besides, a 30-second Ar ion sputter etching step was performed to further clean the wafer surface just before the gold film deposition. Wafers with sputtered gold membranes thus had a higher device yield and better membrane quality than wafers with evaporated gold membranes, as supported by the leak test that will be discussed in Chapter 4.

2.4.3 Nitride etching evaluation

The bulge test was used to non-destructively evaluate the bottom nitride etching step in the microfabrication process. Devices used in this study had evaporated gold membranes. The nitride thickness was 1350 Å. Due to an error made by the outside vendor, about 6000 Å was deposited on the bottom of the reservoirs. Therefore, both the oxide and nitride need to be removed. The nitride etching recipe given in Section 2.3.1 was essentially the oxide etching recipe with oxygen added, and therefore worked for both nitride and oxide etching. Twenty devices were etched in the PlasmaQuest with the etching time ranging from 500 to 3600 seconds. All the etching was performed within an 8-hour period.

Figure 2.17 shows the center deflection of gold membranes with different nitride etching time after bulge tested to 60 psi pressure. The intermediate plateau region seems to suggest that all the nitride was removed with 1500sec etching. This observation however was not well-grounded since the membrane center deflection is strongly dependent on its in-plane size, which was different among the membranes tested. A better way is to compare the extracted mechanical properties of these membranes assuming nitride was completely removed. The pressure-deflection data corresponding to different nitride etching time were fitted using Equation (2.2), and the extracted property data are listed in Table 2.8.

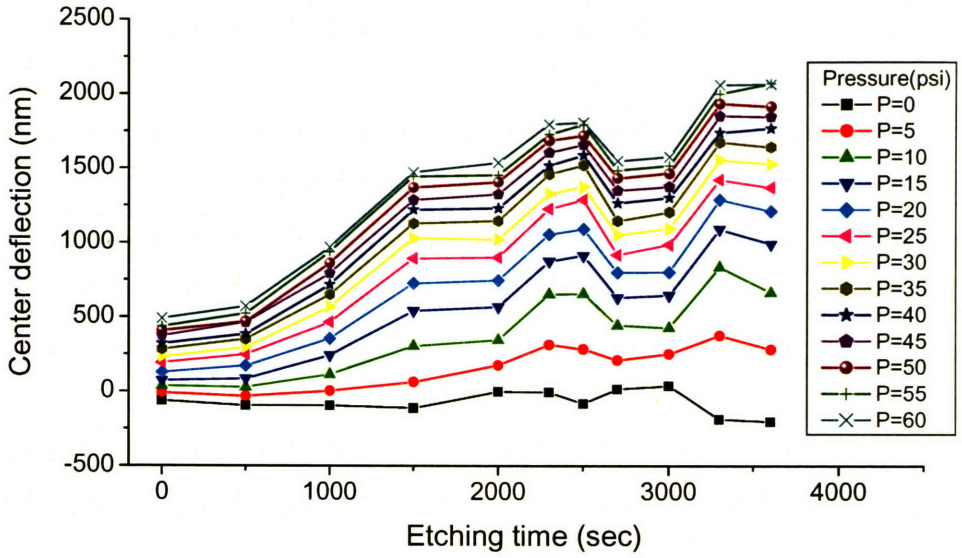

Figure 2.17 Center deflection of 11 gold membranes with different nitride etching time.

Table 2.8 Extracted mechanical properties of gold membranes with different nitride etching time.

Etching time (sec)	**1500**	**2000**	**2300**	**2500**	**2700**	**3000**	**3300**	**3600**
Biaxial modulus (GPa)	175 ±13	135 ±9	142 ±7	142 ±11	121 ±6	130 ±9	103 ±3	75 ±5
Residual stress (MPa)	123 ±11	152 ±9	68 ±10	49 ±15	139 ±7	130 ±10	41 ±4	61 ±9

It is clearly seen from the modulus values that the nitride was not completely removed until after 2000 second etching. The plateau in the elastic modulus from 2000 to 3000 seconds suggests that gold is immune to the CF_4/O_2 plasma etching condition within a certain time range. However, prolonged etching with ion bombardment could have physically weakened the gold membranes, or even caused local yielding of the membrane, which led to abrupt drop of the elastic modulus. An obvious increase in the roughness of the gold membrane bottom surface was also observed with excessive etching (see Figure 2.18).

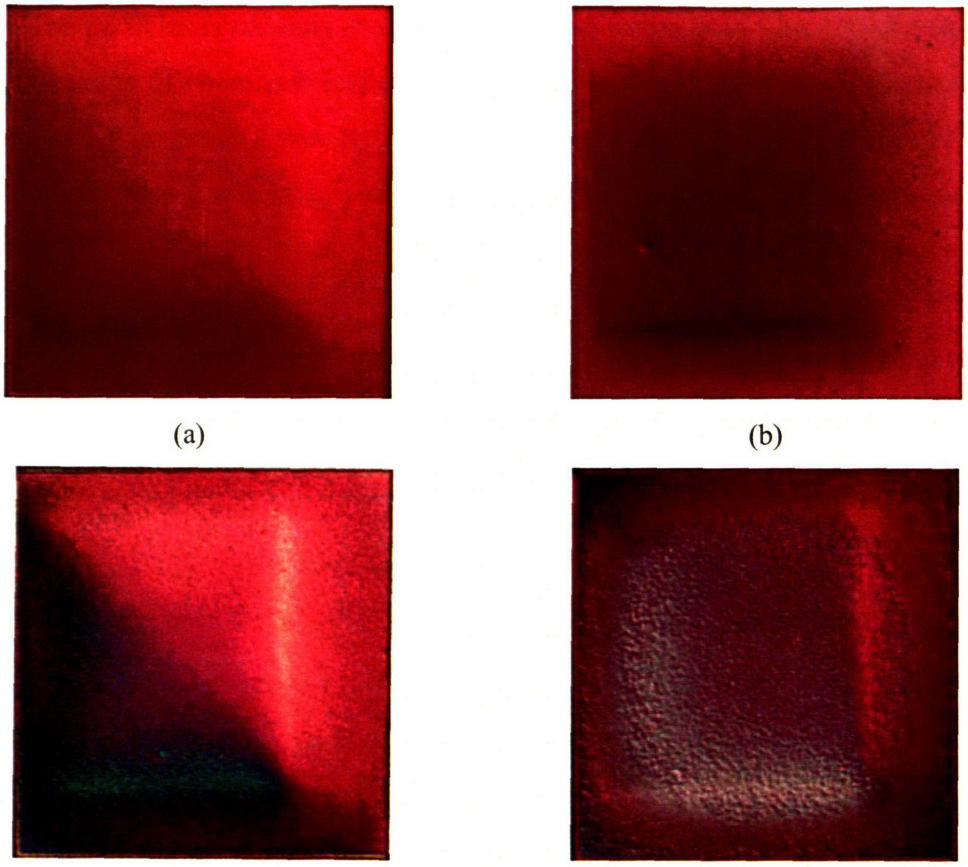

Figure 2.18 Optical micrographs of backside gold membranes (approximately 67 μm in-plane size) with different nitride etching time: (a) unetched, (b) 1000 seconds (c) 2500 seconds and (d) 3600 seconds. The Nomarski filter was used to enhance the image contrast.

It should be noted that the nitride etching time determined from this study may not be applicable to other devices even from the same wafer and using the same nitride etching recipe. The PlasmaQuest is used to perform both PECVD and etching for a variety of films in the same chamber. The etching rate tends to change with different chamber processing history. However, the value of this nitride etching study is that it provided a quick and reliable method to non-destructively evaluate the bottom nitride etching step, which is especially important given the machine variability.

2.5 Conclusions

The bulge test is a viable technique to test the mechanical properties of the gold membranes on the drug delivery MEMS device. Important results from experiments performed in this Chapter are:

(1) Available analytic solutions seem to still work well for membranes with in-plane size in the range of 20~200 μm. The extracted gold membrane properties from the gold/nitride composite systems were comparable to those from pure gold membranes.

(2) The biaxial moduli of gold membranes were independent of their in-plane sizes and were lower compared to bulk (111) gold. The yield strength of the gold membranes, on the other hand, was significantly higher than the bulk value.

(3) Comparing to evaporated gold membranes, membranes deposited by sputtering was denser with a wider grain size distribution. The extracted modulus of sputtered gold membranes was also higher than that of evaporated gold membranes with similar in-plane sizes.

(4) The bulge test also provided a reliable non-destructive method to evaluate the bottom nitride etching step in the microfabrication process. The nitride etching test indicated that gold was immune to the CF_4/O_2 plasma only within a certain time range, and that extended etching tended to weaken the gold membranes and led to decrease of the membrane modulus.

2.6 Acknowledgements

Prof. Carl Thompson is acknowledged for giving access to the Wyko profiler in his laboratory. Robert Bernstein and James Serdy helped with the bulge test setup. Lin Han performed the AFM analysis.

2.7 References

1. Nix, W.D. Mechanical properties of thin films. *Metallurgical Transactions A: Physical Metallurgy and Materials Science* **20A**, 2217-2245 (1989).
2. Alexopoulos, P.S. and O'Sullivan, T.C. Mechanical properties of thin films. *Annual Review of Materials Science* **20**, 391-420 (1990).
3. Huang, H. Mechanical properties of free-standing polycrystalline metallic thin films and multilayers, Ph.D. Thesis, Harvard University, 1998.
4. Sharpe, W.N., Jr. and Hemker, K.J. Mechanical testing of free-standing thin films. *Materials Research Society Symposium Proceedings* **687**, 293-304 (2002).
5. Hohlfelder, R.J. Bulge and blister testing of thin films and their interfaces, Ph.D. Thesis, Stanford University, 1999.
6. Pan, J.Y. and Senturia, S.D. Suspended-membrane methods for determining the effects of humidity on the mechanical properties of thin polymer films. *Annual Technical Conference - Society of Plastics Engineers* **49th**, 1618-1621 (1991).
7. Beams, J.W. Properties of thin films on Au and Ag. *Structure and Properties of Thin Films, Proceedings of an International Conference*, 183-192 (1959).
8. Brotzen, F.R. Mechanical testing of thin films. *International Materials Reviews* **39**, 24-45 (1994).
9. Lin, P. and Senturia, S.D. The in-situ measurement of biaxial modulus and residual stress of multi-layer polymeric thin films. *Materials Research Society Symposium Proceedings* **188**, 41-46 (1990).
10. Pan, J.Y. A study of suspended-membrane and acoustic techniques for the determination of the mechanical properties of thin polymer films, Ph.D. Thesis, Massachusetts Institute of Technology, 1991.
11. Vlassak, J.J. New experimental techniques and analysis methods for the study of the mechanical properties of materials in small volumes (nanoindentation, anisotropy, pressure, deflection), Ph.D. Thesis, Stanford University, 1994.
12. Karimi, A., Shojaei, O.R., Kruml, T. and Martin, J.L. Characterization of TiN thin films using the bulge test and the nanoindentation technique. *Thin Solid Films* **308-309**, 334-339 (1997).
13. Paviot, V.M., Vlassak, J.J. and Nix, W.D. Measuring the mechanical properties of thin metal films by means of bulge testing of micromachined windows. *Materials Research Society Symposium Proceedings* **356**, 579-584 (1995).
14. Leung, O.S. Studies in the strengthening mechanisms of thin polycrystalline gold films, Ph.D. Thesis, 2001.
15. Small, M.K. and Nix, W.D. Analysis of the accuracy of the bulge test in determining the mechanical properties of thin films. *Journal of Materials Research* **7**, 1553-1563 (1992).
16. Small, M.K. Use of the bulge test in measuring the mechanical properties of thin films, Ph.D. Thesis, Stanford University, 1993.

17. Jiran, E. and Thompson, C.V. Capillary instabilities in thin films. *Journal of Electronic Materials* **19**, 1153-1160 (1990).

18. Hummel, R.E., DeHoff, R.T., Matts-Goho, S. and Goho, W.M. Thermal grooving, thermotransport and electrotransport in doped and undoped thin gold films. *Thin Solid Films* **78**, 1-14 (1981).

19. Zecchino, M., Novak, E. and Schmit, J. Advances in Optical Profiling Open New Applications, www.veeco.com/pdf/Optical_Library/ Advances_in_Optical.pdf.

20. ASM Handbook, Vol. 2: Properties and Selection - Nonferrous Alloys and Pure Metals. (ASM International, 1990).

21. Kalkman, A.J., Verbruggen, A.H. and Janssen, G.C.A.M. Young's modulus measurements and grain boundary sliding in free-standing thin metal films. *Applied Physics Letters* **78**, 2673-2675 (2001).

22. Huang, H. and Spaepen, F. Tensile testing of free-standing Cu, Ag and Al thin films and Ag/Cu multilayers. *Acta Materialia* **48**, 3261-3269 (2000).

23. Korn, D., Morsch, A., Birringer, R., Arnold, W. and Gleiter, H. Measurements of the elastic constants, the specific heat, and the entropy of grain boundaries by means of ultrafine grained materials. *Journal de Physique, Colloque*, C5-769/C765-779 (1988).

24. Weller, M., Diehl, J. and Schaefer, H.E. Shear modulus and internal friction in nanometer-sized polycrystalline palladium. *Philosophical Magazine A: Physics of Condensed Matter: Structure, Defects and Mechanical Properties* **63**, 527-533 (1991).

25. Laws, N. and Brockenbrough, J.R. The effect of micro-crack systems on the loss of stiffness of brittle solids. *International Journal of Solids and Structures* **23**, 1247-1268 (1987).

26. Gibeling, J.C. and Nix, W.D. Observations of anelastic backflow following stress reductions during creep of pure metals. *Acta Metallurgica* **29**, 1769-1784 (1981).

27. Nix, W.D., Gibeling, J.C. and Hughes, D.A. Time-dependent deformation of metals. *Metallurgical Transactions A: Physical Metallurgy and Materials Science* **16A**, 2215-2226 (1985).

28. Emery, R.D. and Povirk, G.L. Tensile behavior of free-standing gold films. Part II. Fine-grained films. *Acta Materialia* **51**, 2079-2087 (2003).

29. Emery, R.D. and Povirk, G.L. Tensile behavior of free-standing gold films. Part I. Coarse-grained films. *Acta Materialia* **51**, 2067-2078 (2003).

30. Kang, Y.S., Ho, P.S., Knipe, R. and Tregilgas, J. Film thickness effect on tensile properties and microstructures of submicron aluminum thin films on polyimide. *Materials Research Society Symposium Proceedings* **436**, 35-40 (1997).

31. Ruud, J.A., Josell, D., Spaepen, F. and Greer, A.L. A new method for tensile testing of thin films. *Journal of Materials Research* **8**, 112-117 (1993).

32. Yu, D.Y.W. and Spaepen, F. The yield strength of thin copper films on Kapton. *Journal of Applied Physics* **95**, 2991-2997 (2004).

33. Keller, R.M., Baker, S.P. and Arzt, E. Quantitative analysis of strengthening mechanisms in thin Cu films: effects of film thickness, grain size, and passivation. *Journal of Materials Research* **13**, 1307-1317 (1998).

34. Zhang, J.-M. and Xu, K.-W. The yield strengths of polycrystalline thin films. *Journal of Advanced Materials* **34**, 51-58 (2002).

35. Sharpe, W.N., Jr. Mechanical properties of MEMS materials. *MEMS Handbook*, 3/1-3/33 (2002).

36. Plummer, J.D., Deal, M.D. and Griffin, P.B. Silicon VLSI Technology, Fundamentals, Practice and Modeling. (Prentice Hall, Upper Saddle River, NJ; 2000).

37. Ohring, M. Materials Science of Thin Films, Deposition and Structure., Second Edition. (Academic Press, San Diego, CA; 2002).

38. Madou, M.J. Fundamentals of Microfabrication, the Science of Miniaturization., Second Edition. (CRC Press, Boca Raton, FL; 2002).

39. Thornton, J.A. Structure-zone models of thin films. *Proceedings of SPIE-The International Society for Optical Engineering* **821**, 95-103 (1988).

40. Thompson, C.V. Structure evolution during processing of polycrystalline films. *Annual Review of Materials Science* **30**, 159-190 (2000).

41. Harris, K.E. and King, A.H. Localized texture formation and its detection in polycrystalline thin films of gold. *Materials Research Society Symposium Proceedings* **317**, 425-430 (1994).

42. Munuera, C., Aznarez, J.A., Rodriguez-Canas, E., Oliva, A.I., Aguilar, M. and Sacedon, J.L. Study of rough growth fronts of evaporated polycrystalline gold films. *Journal of Vacuum Science & Technology, A: Vacuum, Surfaces, and Films* **22**, 1767-1772 (2004).

43. Forsyth, A.J., Hutton, S.R., Osborne, C.F. and Rhodes, M.J. Effects of interparticle force on the packing of spherical granular material. *Physical Review Letters* **87**, 244301/244301-244301/244303 (2001).

3 Electrochemical disintegration of gold membranes

3.1 Introduction and motivation

Release of chemicals from the drug delivery MEMS device is achieved by the electrochemical disintegration of gold membranes upon the application of a potential. Understanding the gold membrane disintegration mechanism provides useful guidance to improve the reliability of device operation. For the first prototype drug delivery device developed by Santini, an extended (several seconds to less than 5 minutes) DC potential of 1.04 V vs. a saturated calomel electrode (SCE) was applied to activate and remove the gold membranes in the phosphate buffered saline (PBS) solution. Santini performed *in situ* observation of the membrane disintegration and found non-uniform corrosion occurred across the membrane. He concluded that both corrosion and physical stress (from sources both inside and outside the reservoir) contributed to the disintegration of the gold membranes. However, it was unclear whether these two factors acted independently, or if they acted in combination through the stress corrosion cracking (SCC) mechanism[1].

The DC potential was later found to be less reproducible to activate gold membranes in the calf serum, a biological medium close to the body fluid. A revised voltammetry profile was developed by Shawgo to efficiently activate the membranes *in vivo*[2]. This profile has since been used in both *in vitro* and *in vivo* release studies. It is desirable to understand the gold membrane disintegration mechanism with the new voltammetry profile as it closely correlates with the reliability of device operation both *in vitro* and *in vivo*.

An *in situ* experimental setup was constructed to observe the electrochemical disintegration process of the gold membranes in PBS. Real time images recorded from a CCD camera attached to an optical microscope were used to trace the microstructural changes of the gold membranes. The bulge test was again used in this chapter to evaluate the mechanical integrity of the corroded gold membranes. A qualitative mechanism was developed based on the visualization and mechanical testing results.

3.2 Experimental methods

3.2.1 Device fabrication and packaging

Devices were fabricated using the same microfabrication process described in the previous chapter (Section 2.2.1). The gold membranes on these devices were deposited by evaporation. A 100 Å Ti layer was deposited both before and after the gold film evaporation to promote the adhesion of gold to the nitride as well as to the oxide.

Fifteen devices from the same wafer (# 091902-11) were packaged using the method developed by Shawgo. Stainless steel frames (Microphoto Inc., Roseville, MI) pressed the device reservoirs against a silicone gasket (125 μm thick, Advanced Bio-Technologies, Silverdale, WA) and backing plate. A detachable connector board and gold wire bonding (Gold ball wire bonder, Model 4124, Kulicke and Soffa Industries Inc., Willow Grove, PA) were used to establish electrical connection between the device and the external triggering unit, a potentiostat. Wirebonds were mechanically protected and electrically isolated with two-component epoxy (Masterbond EP42HT, Hackensack, NJ). Photos of a device packaged in frames and a complete package with a connector board are shown in Figure 3.1.

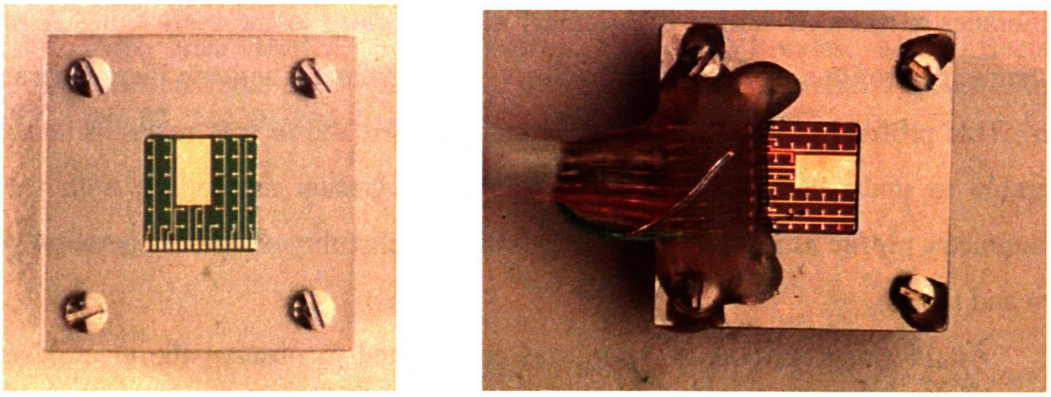

(a) (b)

Figure 3.1 Photographs of (a) a packaged device and (b) a packaged device with electrical connection established by wire bonding through a connector board fixed on frame top using epoxy. Photos taken by Rebecca Shawgo.

3.2.2 *In situ* observation setup

The packaged device was fixed inside a plastic petri dish using epoxy (Devcon 5-minute epoxy). PBS solution (0.15 M PO_4^-: 0.15 M Cl^-, pH 7.2) was filled to completely cover the device top surface. The dish was placed under an optical light microscope (Olympus BH-2) with an ultra long working distance 50x objective and 10x eyepiece. A 3-CCD color camera (Hitachi HV-D30) was attached to the microscope to capture real time video images, which were archived to DV cassettes (Panasonic DV 120) through a digital video recorder (Panasonic AG-DV2000). The video data were captured and analyzed using Adobe Premier (Version 6.0) through an IEEE 1394 interface with the following settings: NTSC DV format, 720 × 480 frame size, 0.9 pixel aspect ratio, and 29.97 frame rate. Figure 3.2 illustrates the *in situ* experimental setup.

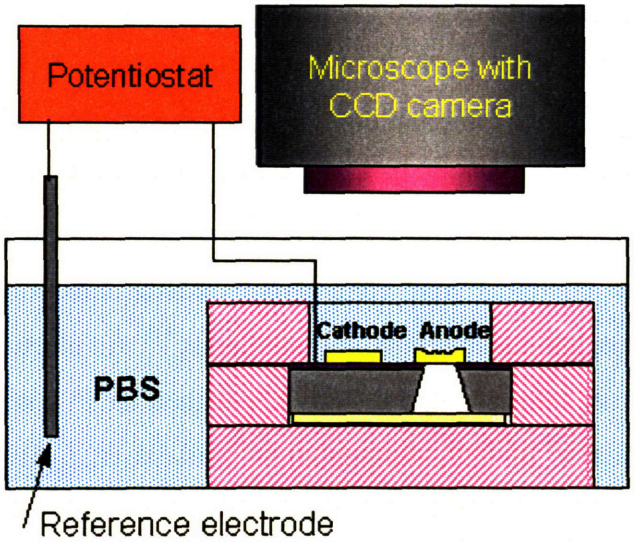

Figure 3.2 Schematic of the *in situ* observation setup.

3.2.3 Electrochemical test

A Gamry potentiostat (PC 4-300, Gamry Instruments, Warminster, PA) was used to output the voltammetry profile to the packaged drug delivery devices. The electrochemical test used a three-electrode system, which included the 50 x 50 μm anode gold membranes and a large cathode gold membrane on the device, and a platinum (Pt) wire serving as the reference electrode.

One key requirement for the reference electrode is a stable and well characterized reference potential in the test solution. SCE is a popular reference electrode for common laboratory use. However, SCE will leak Cl^- into the electrochemical cell, which can change the Cl^- concentration of the electrolyte and requires the use of a salt bridge to keep constant Cl^- concentration in the cell. The bulky size of SCE and salt bridge makes it unsuitable to be used as an *in vivo* reference electrode. A platinum wire was chosen because of its small size and biocompatibility. The commercially available Pt wire has a very smooth shining surface. Such a Pt electrode however was found to function less stable in the PBS solution, as shown by the cycle to cycle shift in the gold corrosion peak potential as well as the difference in the magnitude of peak corrosion rate in the cyclic voltammograms for a gold foil in PBS solution (see Figure 3.3a).

The reason for the unstable electrochemical behavior was largely due to the high impedance of the Pt electrode-electrolyte (PBS) interface, which led to a large potential drop near the interface[3]. This made the electric field applied to the working electrodes highly susceptible to small fluctuations in the interface condition. Roughening the electrode surface has been found to significantly lower the electrode impedance by increasing the effective surface area. Various surface roughening procedures have been developed, such as chemical and electrolytic etching, electrodeposition, oxidation-reduction cycling, mechanical abrasion, and sputtering[4-8]. An electrodeposition procedure developed by Kershner was used in our study to roughen the Pt wire surface[9]. The Pt wire was placed in a solution of 2 % chloroplatinic acid (H_2PtCl_6-$6H_2O$) and 0.02 % lead acetate [$Pb(CH_3COO)_2$-$3H_2O$] as a cathode with respect to a large area platinum foil anode. A current of 3 mA (120 Current Source, LakeShore Cryotronics, Westerville, OH) was applied on a Pt wire (0.2 mm diameter, Alfa Aesar, Ward Hill, MA) with 15 mm long tip immersed in the solution for 2 minute, leading to the deposition of a uniform coating with thickness approximately 5 μm as measured under an optical microscope. The deposited Pt coating appeared black due to the high roughness of the electroplated surface. The term "blackened Pt wire" will be used in this chapter to refer to the reference Pt wire electrode after the above electrodeposition roughening treatment. The potential of the blackened Pt wire electrode measured + 0.32 V vs. SCE in PBS (0.15 M Cl^-, 25 °C).

A more stable electrochemical response was obtained using the blackened Pt wire as the reference electrode, as shown in Figure 3.3b.

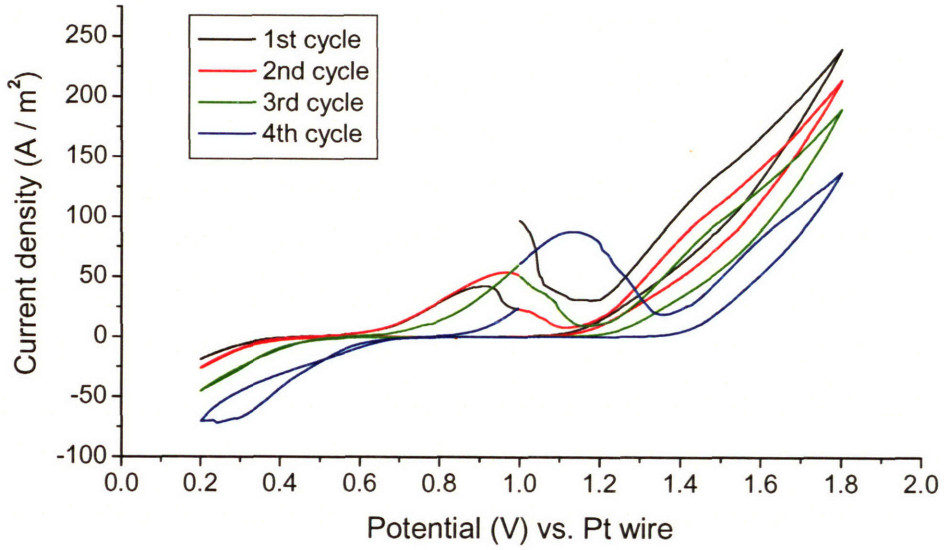

(a)

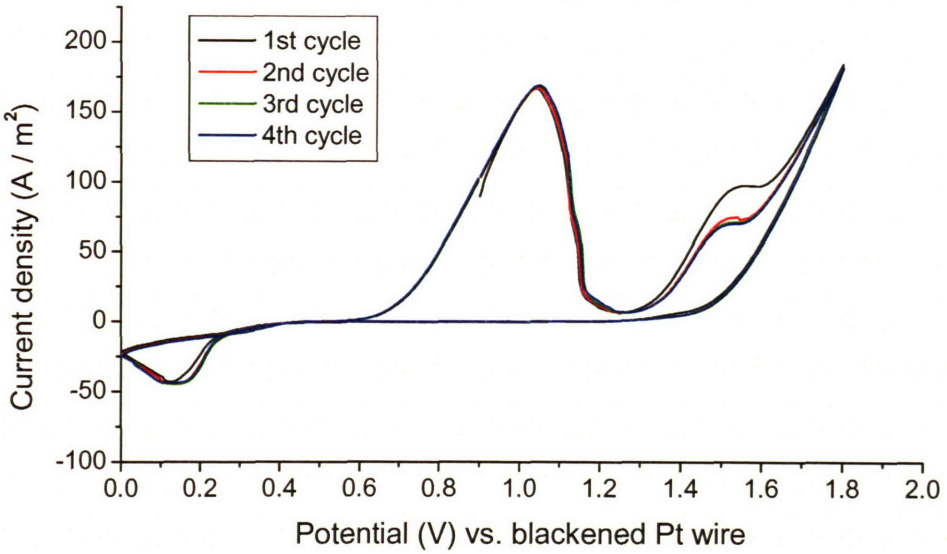

(b)

Figure 3.3 Cyclic voltammograms for a gold foil in PBS using (a) a smooth shiny Pt wire and (b) a blackened Pt wire as the reference electrode. Two gold foils (10 × 5 × 0.05 mm) were used as the counter and working electrodes. The current density was calculated by dividing the measured current by the apparent surface area of the working electrode (1.015×10^{-4} m^2).

The following voltammetry profile was applied to each of the 15 devices: One row of gold anode membranes (Row G in Figure 3.4) was selected as the test row that

received two sets of cyclic scans. This included 4 cathodic cleaning cycles between −1 to −1.5 V at 100 mV/sec scan rate, and 4 diagnostic cycles between 0 and 1.5V at 100 mV/sec scan rate. All 15 devices showed a peak corrosion potential at 0.75 (± 0.03) V and depassivation potential at 0.04 (± 0.02) V (Figure 3.5). A square wave voltammetry (0/0.8 V, 1Hz) was then applied to the other 5 rows of membranes on each device for different duration of time, ranging from 1 second to 10 minutes. All potential values were relative to a blackened Pt wire placed approximately 5 mm away from the packaged device in PBS. All electrochemical tests were performed at room temperature with no stirring of the electrolyte solution. Each of the packaged devices was examined under the optical microscope before the electrochemical test. Occasionally one or two membranes were found broken, which were noted and excluded from later analysis. Besides the test row of membranes, a maximum of 24 membranes on each device were electrochemically corroded for the same duration of time using the square wave voltammetry.

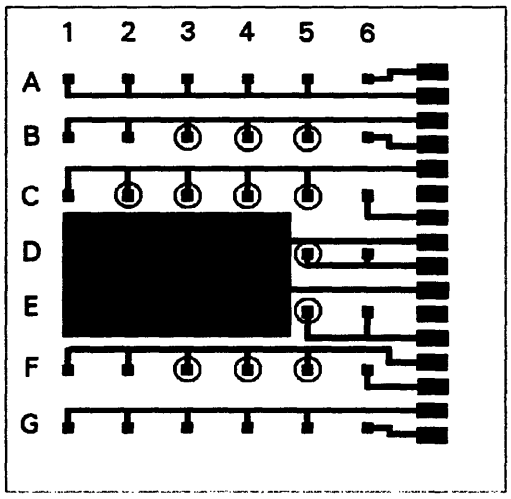

Figure 3.4 Designation of electrodes in the electrochemical and bulge tests. Each anode is designated by a combination of row (letter) and column (number). Bulge test was performed on the 12 anodes (marked by circle) after the electrochemical corrosion test.

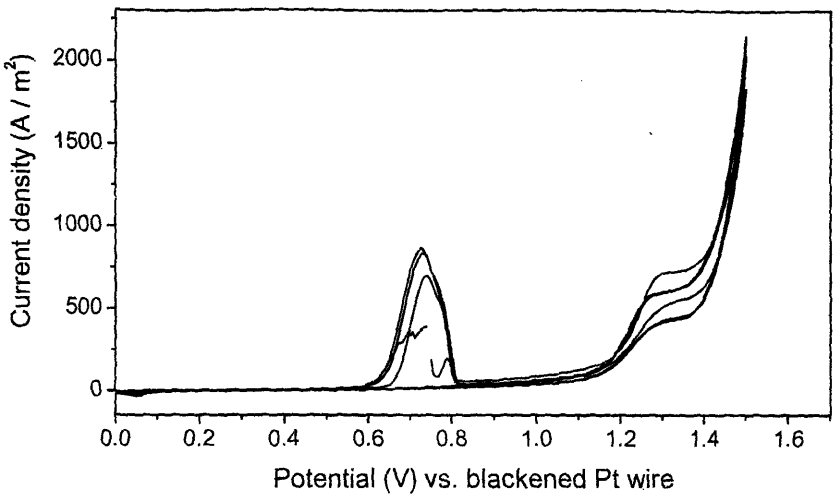

Figure 3.5 Typical cyclic voltammograms for gold membranes in the diagnostic scan in PBS with 0.15 M Cl^-, pH =7.2, 25 °C and 100 mV/sec scan rate.

3.2.4 Bulge test

Following the electrochemical test, the bottom plate of the packaged device was immediately removed. The remaining corroded device was placed on the bulge test apparatus described in Chapter 2. Pressure was applied from 0 to 60 psi at 5 psi interval. At every 5psi interval, the 3D profiles of each membrane were recorded and analyzed. The device was pressed against a silicon gasket with a 3mm hole so that at most 12 corroded membranes (marked in Figure 3.4) could be bulge tested.

3.3 Results and discussion

3.3.1 Visualization of the gold membrane corrosion process

Figure 3.6 shows a series of real time images of a gold membrane under the square wave voltammetry with potential alternating between 0 and 0.8 V at 1 Hz frequency. Non-uniform corrosion was observed to occur first around the membrane edges, probably due to the non-uniform distribution of potential across the membrane. The corrosion proceeded from the edges toward the center until the membrane opened.

Another interesting observation is the periodic change of the brightness of the membrane synchronized with the alternating potential. Comparison of Figure 3.6b and Figure 3.6c indicated that the membrane seemed to be brighter at the half cycle than at the integer cycle.

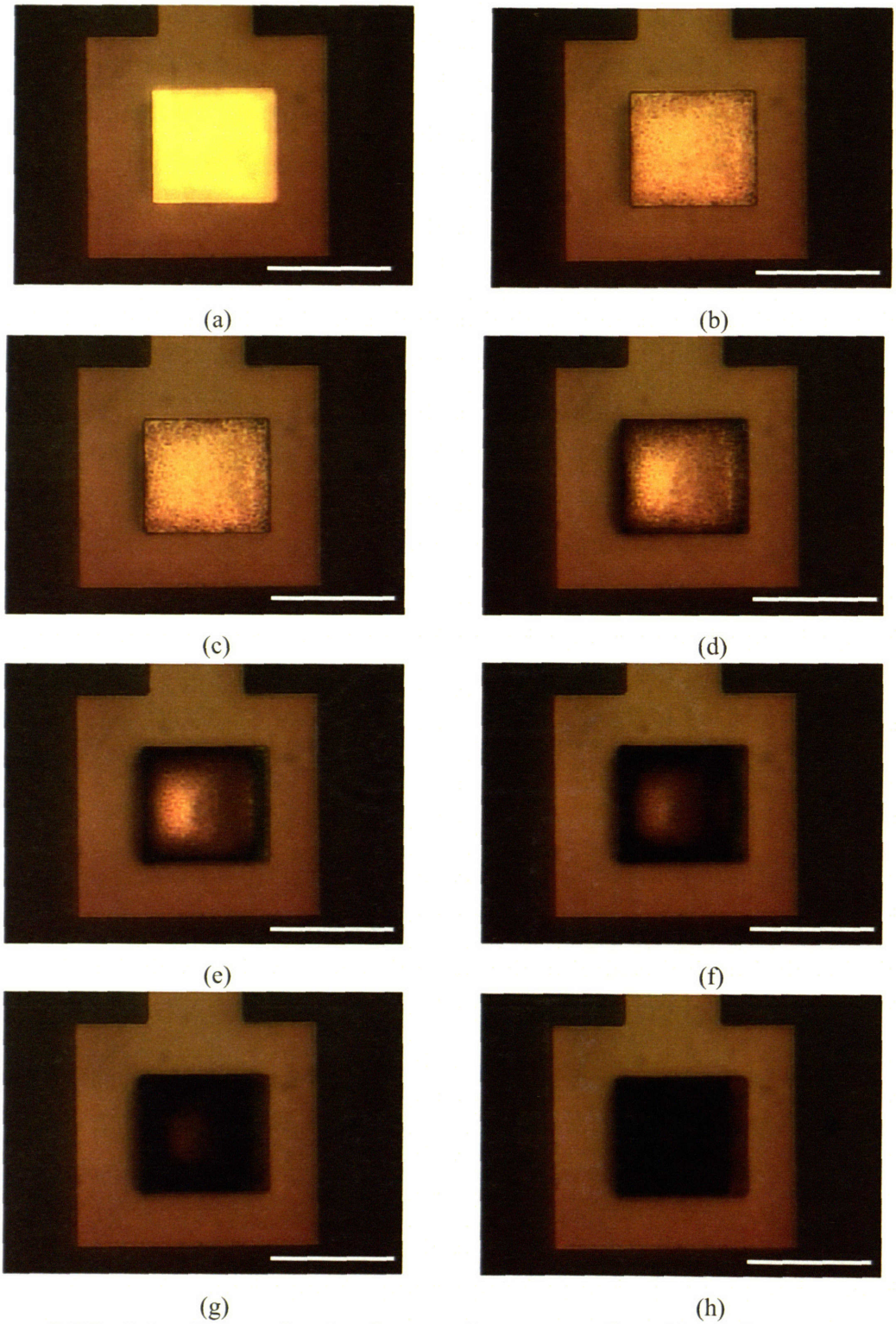

Figure 3.6 Real time images showing the corrosion process of a gold membrane under a square wave voltammetry with (a) 0 cycle, (b) 7 cycles, (c) 7.5 cycles, (d) 12 cycles, (e) 17 cycles, (f) 20 cycles, (g) 24 cycles, and (h) 30 cycles in PBS. Scale bar is 50 μm.

The number of opened membranes on each corroded device was counted and listed in Table 3.1. The time for the membranes to open varied from less than 1 minute to several minutes. More than 90% of the membranes on all the 15 devices were opened after being corroded longer than 1 minute.

Table 3.1 Results of gold membranes opening after corrosion for different duration of time in PBS.

Corrosion time (sec)	Total number of tested membranes	Total number of opened membranes	Notes*
1	24	0	
3	24	0	
5	24	0	
7	24	0	
10	24	0	
15	23	0	F5 broken
17	22	5	E5 & E6 broken
20	23	3	C3 broken
25	24	17	
30	24	19	
40	22	19	Row D broken connection
50	24	12	
60	22	20	A1& C3 broken
240	23	22	F4 broken
600	24	24	

*Notes: These membranes were broken when observed under the optical microscope after packaging and were excluded from the subsequent electrochemical test and analysis. The membranes were named by the row (letter) and column (number) labels used in Figure 3.4.

3.3.2 Mechanical integrity of corroded membranes

The bulge test on the corroded membranes yielded two types of results, as illustrated in Figure 3.7 and Figure 3.8. All membranes corroded longer than 7 seconds burst at a certain pressure, whereas membranes corroded shorter than 5 seconds could be pressurized up to 60 psi without rupture.

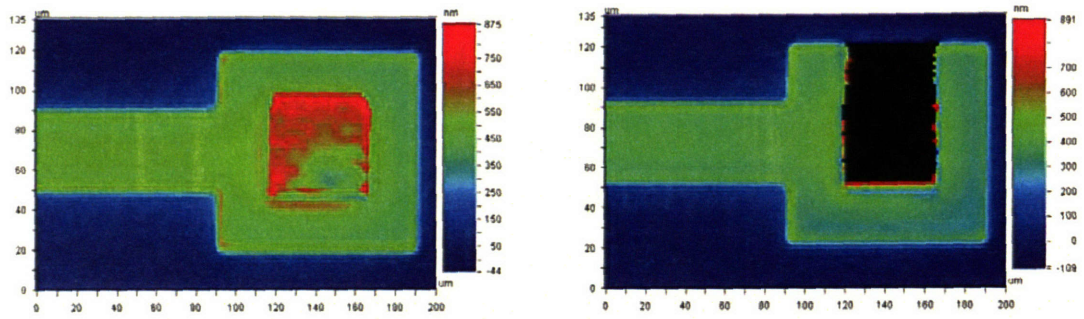

(a) (b)

Figure 3.7 2D profiles of a 15-second corroded gold membrane (a) before the bulge test and (b) burst under 5 psi pressure.

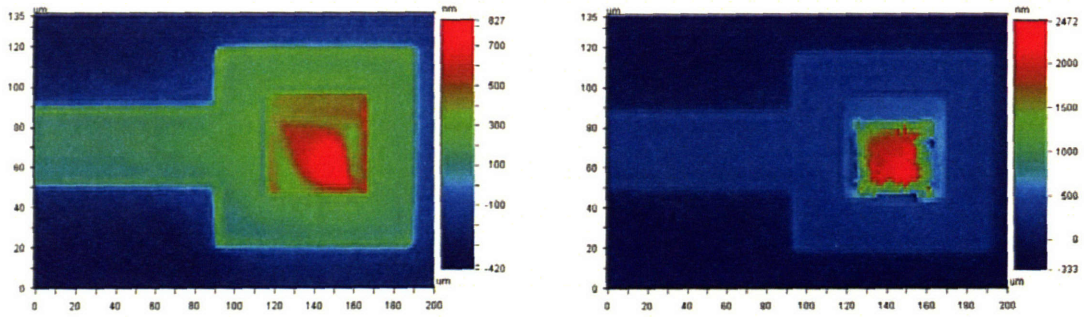

(a) (b)

Figure 3.8 2D profiles of a 5-second corroded gold membrane (a) before the bulge test and (b) under 60 psi pressure.

The bulge test results were summarized in Table 3.2 (for membranes corroded longer than 7 seconds) and Figure 3.9 (for membranes corroded shorter than 5 seconds). A trend of decreasing burst pressure with longer corrosion time was clearly seen in Table 3.2. However, membranes corroded for the same duration of time did not necessarily burst at the same pressure, reflecting the non-uniform nature of the corrosion process. In Figure 3.9, membranes corroded for longer time also showed a higher center deflection as well as larger data scatter. It is difficult to extract exact mechanical property data of these corrode membranes due to unknown membrane thickness and possible variation of in-plane sizes between membranes. Nevertheless, results in Table 3.2 and Figure 3.9 clearly indicated that the electrochemical corrosion led to a gradual loss of the mechanical integrity of gold membranes.

Table 3.2 Percentage of burst gold membranes as a function of corrosion time and applied pressure.

Burst pressure (psi) / Corrosion time (sec)	0	5	10	15	20	25	30	35	40	45	50	55
7							25		17	50	8	
10		17	8		25		17		17	8		8
15		9	64	9	9	9						
17	27	27	9	9			9					
20	18	18	64									
25	75	25										
30	84			8	8							
40	100											
50	42	50	8									
60	100											
240	91	9										
600	100											

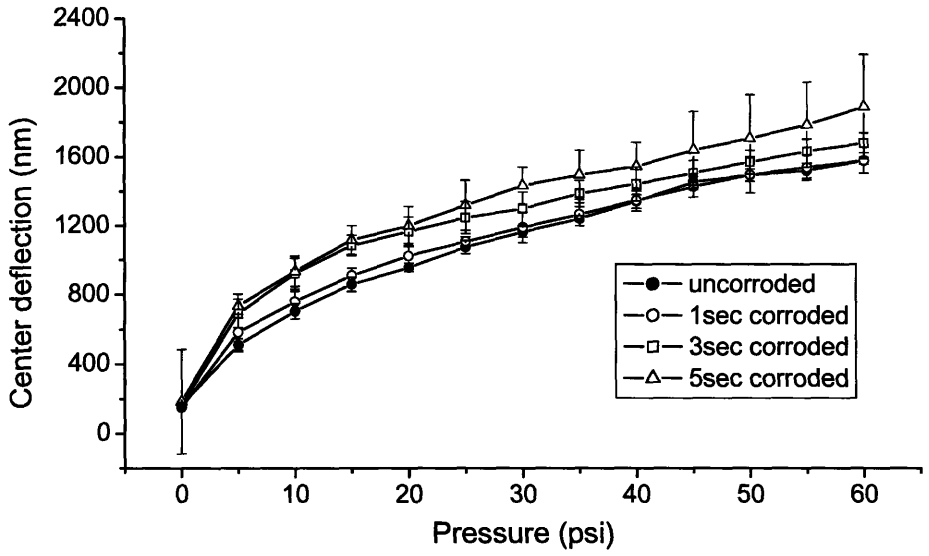

Figure 3.9 Deflection of gold membranes corroded for different time under the bulge test. Each data point calculated from N= 4 membranes.

Analysis of the 3D profiles of the corroded membranes revealed another interesting phenomenon, as shown in Figure 3.10. The uncorroded gold membrane

showed a flat profile (Figure 3.10a), which was consistent with the slightly tensile residual stress in the membrane analyzed in Chapter 2. In contrast, a buckled profile was observed for all membranes corroded longer than 5 seconds, as shown in Figure 3.10b-d.

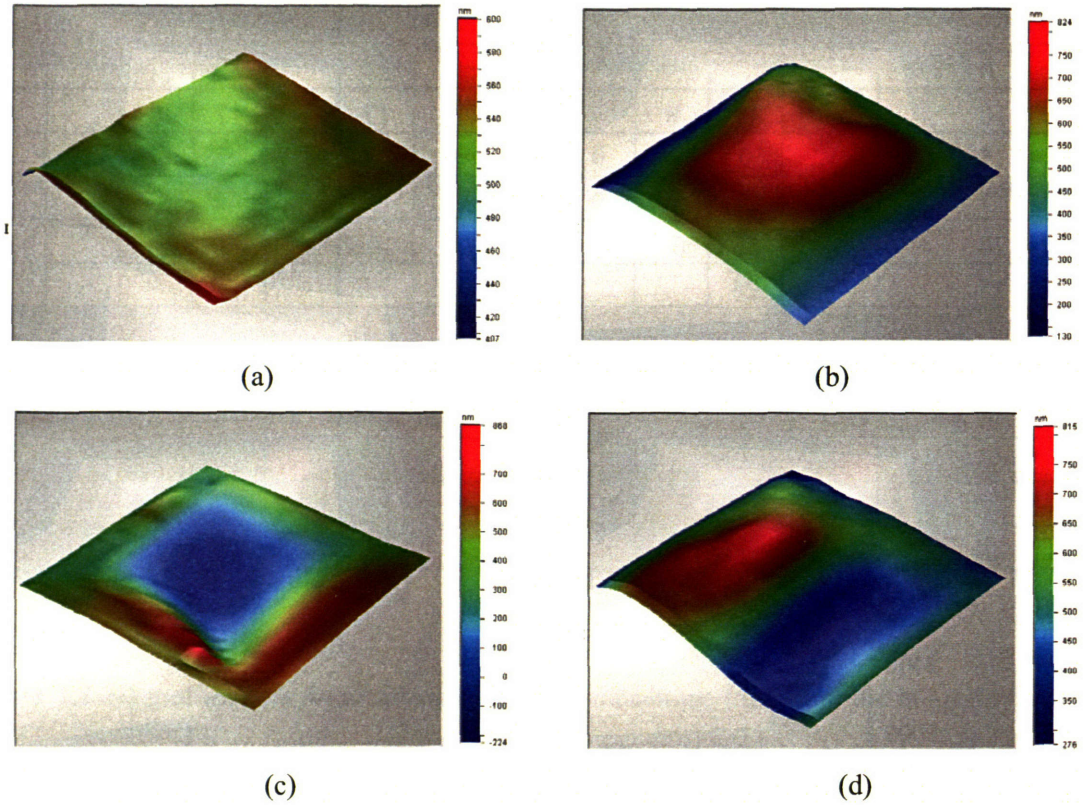

Figure 3.10 Typical 3D profiles of gold membranes (a) uncorroded, and (b)-(d) corroded for 5~15 seconds.

The roughness and peak-to-valley difference for the corroded membranes were calculated and plotted in Figure 3.11. A small increase in the membrane surface roughness was noted with increasing corrosion time. However, the peak-to-valley difference exhibited a much larger increase over time, which was in agreement with the observed buckled membrane profiles shown in Figure 3.10.

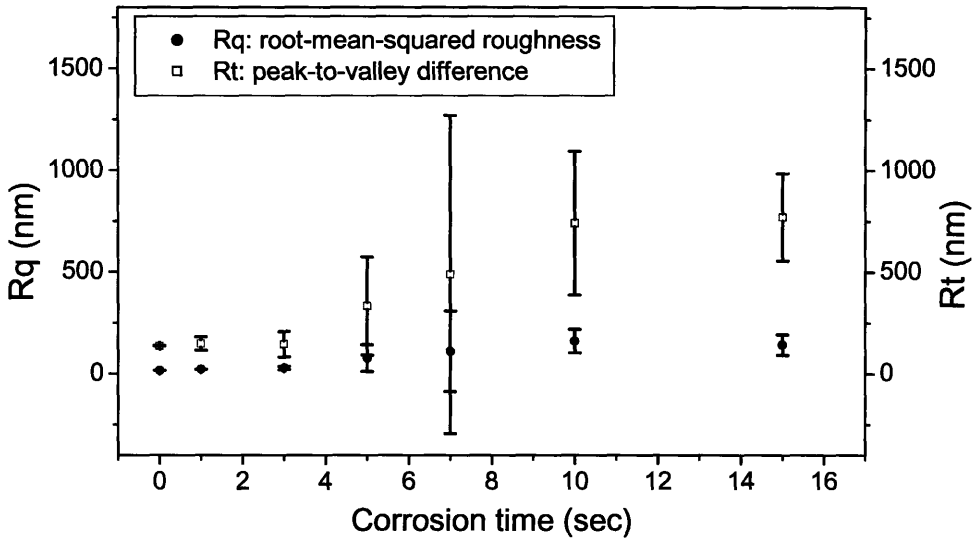

Figure 3.11 3D profile data analysis of gold membranes corroded for different duration of time in PBS. Each data point calculated from N=4 membranes.

3.3.3 Electrochemical disintegration process of gold membranes

Results from the previous section indicated that the electrochemical corrosion led to a gradual loss of the mechanical integrity of the gold membranes, accompanied by a rapid transition of the membrane profile form flat to buckled. An examination of the thermodynamics and kinetics of gold corrosion helped to explain the possible cause for the buckled profile and to understand the gold membrane disintegration process. Figure 3.12 shows the calculated Pourbaix diagram of gold in chloride solution (0.1 M). Figure 3.13 (Evans diagram) is a duplicate of Figure 3.5 with exchange of the x-y axis and conversion of the potential relative to SCE for easy comparison with the Pourbaix diagram. All potentials used in this section are relative to SCE unless otherwise noted.

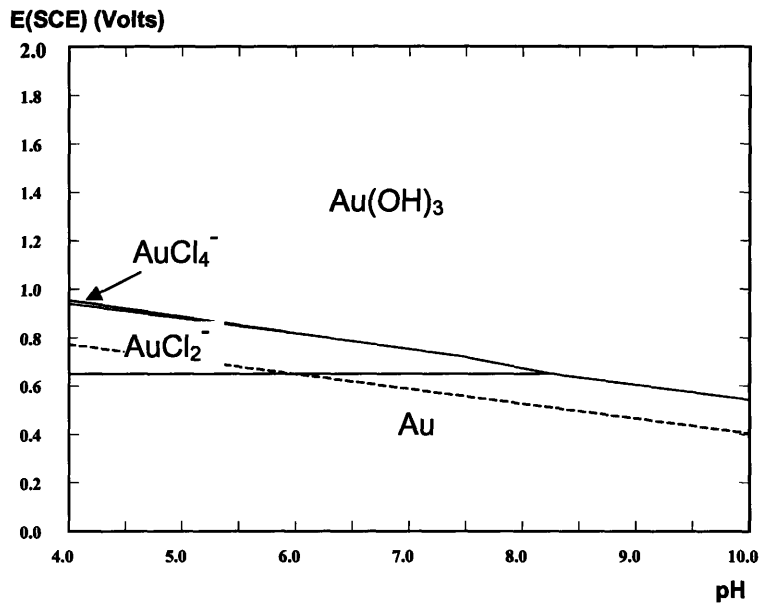

Figure 3.12 Calculated Pourbaix diagram for gold in water containing 0.1 M chloride ions[10].

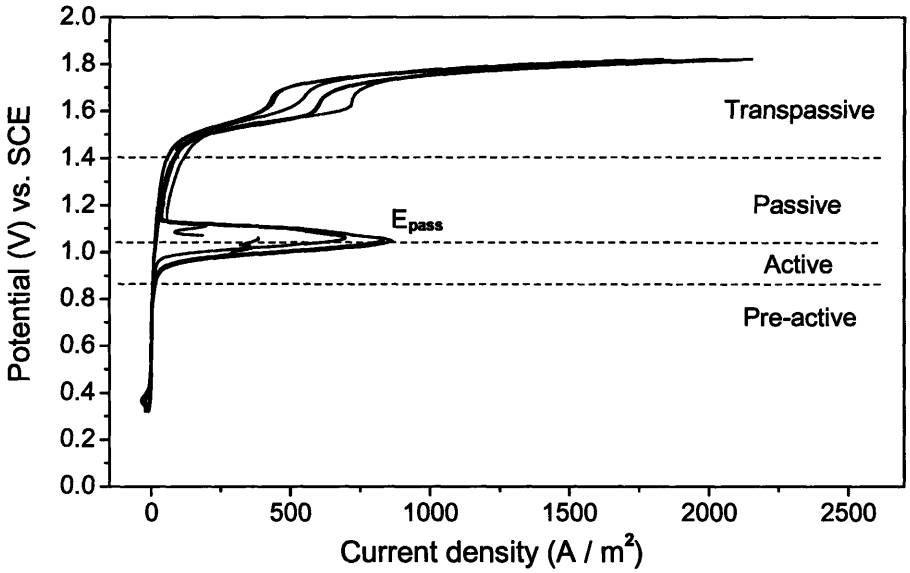

Figure 3.13 Evans diagram for gold membranes in PBS with 0.15 M Cl^-, pH =7.2, 25 °C and 100 mV/sec scan rate.

Detailed discussions on the gold corrosion can be found in the literature[11-15]. A brief description about the four regions (shown in Figure 3.13) in the gold electrochemical behavior is provided below:

The pre-active region (E < 0.9 V) is characterized by close to zero current density indicating no occurrence of corrosion. The gold surface however is believed to be

saturated with chloride ions. When the potential exceeds 0.9 V, the formation of a soluble gold chloride complex leads to active dissolution of gold. Many experimental studies have confirmed Au^{3+} to be the main species formed from gold dissolution[14, 16, 17]. The gold surface enters a state of passivity with the formation of a protective oxide film when the potential is increased above E_{pass}. E_{pass} is defined as the potential where the passive film growth begins to predominate over dissolution with the current dropping to a very low level, and generally falls in the range of 1.05~1.2 V[13-15, 18]. The mechanism for the passive film formation is explained by oxygen adsorption and/or chloride ion depletion on the gold surface. The transpassive region (E > 1.4 V) is characterized by breakdown of the passive film, the evolution of gases such as chlorine and oxygen, and an increase in the current density. The little peak in the cathodic polarization segment when the potential is swept back to zero is related to the redeposition of dissolved Au^{3+} ions. The anodic dissolution peak is much higher than the cathodic redeposition peak, indicating a net mass loss of gold after experiencing one voltammetry cycle.

In our study, the gold membranes were corroded by a square wave voltammetry with potential alternating between 0.32 and 1.12 V vs. SCE (or between 0 and 0.8 V vs. blackened Pt wire). The upper potential (1.12V) exceeded E_{pass} measured from the diagnostic scan (1.05 V). Therefore, the gold dissolution was followed by the formation of a passive film when the potential reached the upper bound in each voltammetry cycle. This passive film would be broken down when the potential cycled to the lower bound (0.32V) due to the presence of chloride. Chloride has been known to induce passivity breakdown in many metals and alloys including gold[19-21]. The removal of the passive film exposed the gold surface for corrosion to proceed in the next cycle, as well as the formation and breakdown of another passive layer.

Figure 3.14 shows a typical current vs. time plot for a row of 5 gold membranes under the square wave voltammetry. The high current in each half voltammetry cycle indicated corrosion of gold, while the close to zero current in the other half cycle indicated the formation and breakdown of the passive film when little gold corrosion occurred. The peak current varied among different rows of membranes and different devices. Some membranes showed a decreasing peak current over time. A peak current range of 2~20 μA was observed for all the devices tested in this study.

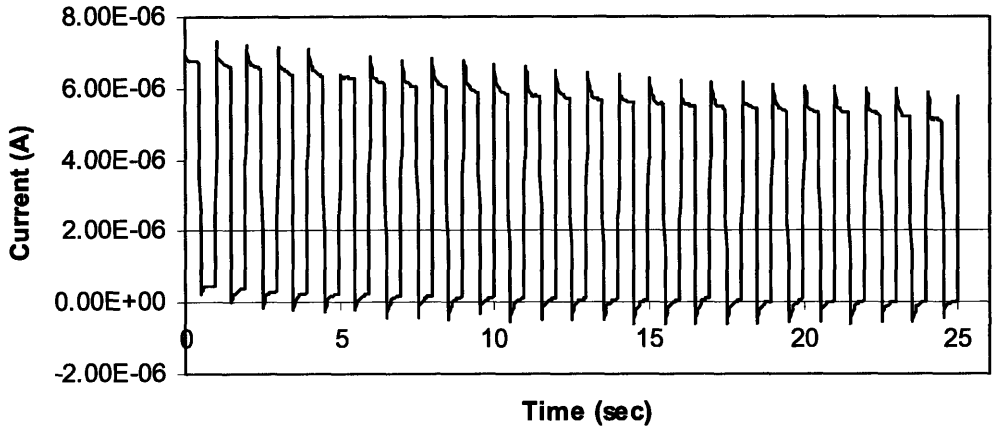

Figure 3.14 A typical current vs. time plot for a row of 5 gold membranes under the square wave voltammetry in PBS.

The gold membrane corrosion rate can be estimated using Faraday's Law[22]:

$$m = \frac{Ita}{nF} \qquad \text{(Equation 3.1)}$$

where I is the current, t the time, a the atomic weight, n the number of equivalents exchanged, and F the Faraday's constant (96500 Coulombs/equivalents). For gold, a=197 g/mol, n=3 assuming Au^{3+} is the main corrosion species. The mass of corroded gold per cycle of square wave voltammetry was calculated to be in the range of 0.68 to 6.8 ng corresponding to a peak current of 2 to 20 μA.

Furthermore, assuming uniform corrosion in the thickness direction and a film density of 19.3 g/cm^3, we can estimate the corrosion rate of gold membranes to be 2.8 to 28 nm per second. Therefore, the time needed to completely remove a 250 nm thick gold membrane would be in the range of 9 to 89 seconds. Although the range agrees with the observed results, the above calculation is an overestimation by assuming that all the current passed was used to corrode the exposed gold membranes. In fact, the uniform corrosion rate assumption contradicts with the observation of non-uniform corrosion illustrated in Figure 3.6. Moreover, no correlation was found between the peak current value and the time needed for membranes to open in this electrochemical test. The peak current did not become zero after all membranes were opened, implying that not 100% of the passed current was used to corrode the exposed gold membranes. After the

membranes were fully opened, the electrochemical reaction probably continued to extend to the gold covered by the oxide passivation layer.

The buckled profiles in Figure 3.10 were most probably a result of plastic deformation of the corroded gold membranes. It is postulated that the transient formation of the passive film in each voltammetry cycle led to the accumulation of plastic deformation, which contributed to the electrochemical disintegration of the gold membranes. A qualitative analysis is provided below in order to support this hypothesis.

It is well accepted in electrochemistry that the passive film formation involves oxide growth on top of a noble metal electrode (such as gold or platinum) when an anodic potential is applied. The mechanism of the anodic oxide film formation at polycrystalline gold electrodes is believed to proceed by surface chemical processes mainly involving the following two steps[23], as shown schematically in Figure 3.15:

(1) Initial monolayer formation of a two-dimensional compact oxide (α-oxide) film, which occurs through place-exchange between the adsorbed OH or O species on the surface and Au atoms within the surface lattice. The Au α-oxide (AuO, $Au(OH)_2$[24], Au_2O_3[25], have all been suggested) is anhydrous and only can form up to 3 monolayers[26].

(2) Higher potential and longer time lead to the growth of a multilayer hydrous oxide (β-oxide) film, probably by continuing injection of ions of the substrate metal and their migration through the growing film under the influence of the electric filed[23]. The Au β-oxide is hydrous and poorly ordered with low density[27]. Many compositions have been suggested for the Au β-oxide, including AuOH, $Au(OH)_3$, and a series of $Au_2O_3 \cdot nH_2O$ (n ranging from 1 to 10)[26]. The Au β-oxide grows with no limiting thickness with its composition and structure being strongly influenced by factors such as potential, temperature, pH, and ionic strength. For example, three Au β-oxide states were identified in the potentiostatic polarization of Au electrodes in 0.5 M aqueous H_2SO_4[24], 1.0M $HClO_4$[28] and 0.5 M KOH[24] solutions. Another study using ellipsometric and quartz crystal microbalance techniques found that the β-oxide film became increasingly hydrated as it thickened when grown at constant potential, with a mass to charge ratio and refractive index consistent with $Au_2O_3 \cdot H_2O$ and later with $Au_2O_3 \cdot 2H_2O$. In contrast, the β-oxide film formed by multicycling was found to become less hydrated as it thickened

with time, with a mass to charge ratio and refractive index consistent with $Au_2O_3 \cdot 10H_2O$ and later with $Au_2O_3 \cdot 2H_2O$ as the film thickened[26].

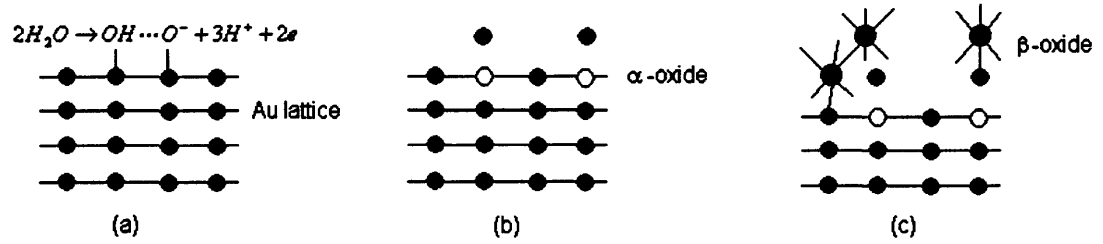

Figure 3.15 Schematic of the formation of Au anodic oxides in aqueous solutions. (a) initial adsorption of OH or O on metal surface, (b) place-exchanged formation of compact Au α-oxide monolayer, (c) growth of hydrous Au β-oxide film under higher potential and/or with longer time. Redrawn after Burke[27].

The growth kinetics of Au anodic films was experimentally determined by a number of researchers to follow the logarithmic growth law[24, 28, 29]. However, some researchers found an inverse logarithmic relation[24] ($1/q \propto -\log t$, here q is the oxide charge reduction density, a quantity proportional to the oxide thickness, and t is the growth time), whereas other researchers claimed a direct logarithmic relation[28] ($q \propto \log t$). The extracted slopes of the logarithmic curves vary greatly in different studies, the interpretation of which remains controversial. Two and even more distinguishable kinetic regions have also been reported in many studies[24, 28], presumably corresponding to the growth of Au α-oxide and various β-oxides.

It is well known that the thermal oxidation of Si and metals could induce stress, which includes the thermal stress and internal stress generated during the film growth. The thermal stress is not a factor in the formation of the gold passive film in our study. However, the growth of the gold oxide film could induce stress in both the oxide film and the gold membrane (substrate). In fact, stress generation has been reported in the anodic oxidation of a number of metals such as aluminum[30] (Al), tungsten[31] (W), titanium[32, 33] (Ti), zirconium[34] (Zr), and nickel[35] (Ni).

Stresses in the anodic oxide films include the volume-generated stress and electrostrictive stress[32, 36]. The electrostrictive stress is usually insignificant because of the weak electric field used in the anodic polarization. Kim's study confirmed that the

electrostrictive stress constituted less than 10% of the total stress during the growth of anodic oxide films on a W electrode[36]. The volume-generated stress is closely related to the Pilling-Bedworth ratio[37] (PBR), defined as the volume of the metal oxide to the consumed metal volume:

$$PBR = \frac{V_{metal\ oxide\ produced}}{V_{metal\ consumed}} = \frac{M\,d}{a\,m\,D} \qquad \text{(Equation 3.2)}$$

where M and D are the molecular weight and density of the metal oxide with composition $(Metal)_a(Oxygen)_b$; *m* and *d* are the atomic weight and density of the metal. The sign and magnitude of the volume-generated stress are related to (1-PBR). A positive sign indicates tensile stress and a negative sign indicates compressive stress in the oxide film. A larger absolute value of (1-PBR) implies a higher stress[38].

PBR values for most metals fall in the range of 0.5~3[39]. No PBR data is available for gold, probably because of the unstable nature of gold oxides. Data of the physical properties of gold oxides are also scarce. Nevertheless, we can estimate the PBR for the Au-Au_2O_3 system, using available density data of bulk Au_2O_3 (10.58 g/cm^3)[40] and Au (19.3 g/cm^3), molecular weight of Au_2O_3 (442 g/mol), and atomic weight of Au (197 g/mol). The calculated PBR (=2) is higher than many metals, suggesting that high stress could occur in the gold oxide film. A few GPa stress was measured during the formation of the first monolayer oxide for Ni[35], which has a PBR of 1.65[39]. It is therefore reasonable to assume that GPa level stress could be generated during the formation of the Au α-oxide film in our study.

The stress in the underlying gold membrane (σ_{Au}) is then directly related to the oxide film stress (σ_{Au2O3}) by applying the force equilibrium condition:

$$\int_0^{Au} \sigma_{Au}(z)dz = -\int_{Au}^{Au+Au2O3} \sigma_{Au2O3}(z)dz \qquad \text{(Equation 3.3)}$$

where t_{Au} and t_{Au2O3} are the thicknesses of the gold membrane and oxide respectively.

Although the stress distribution in the gold membrane is unknown, it is reasonable to assume that the gold area adjacent to the Au/oxide interface has the highest stress considering that this is the region that is perturbed most by the oxide growth. It is thus plausible that high stress in this area could even exceed the yield strength of gold (around 300 MPa according to the estimation in Chapter 2) and induce plastic deformation of the

substrate membrane. As a supporting example of the above argument, plastic deformation of 100 μm thick Si substrates (which is much thicker than the submicron thick gold membrane in our study) has been found to occur during the oxidation process[41].

It is also possible that the failure (or opening) of the corroded gold membrane occurred when there was still some gold mass remaining. With the accumulation of plastic deformation after each voltammetry cycle, a critical state could be reached when the exerted stress in a new voltammetry cycle exceeded the fracture strength of the deformed gold membrane, causing it to fail. Therefore, the electrochemical disintegration of gold membranes under the square wave voltammetry is a result of the combined effect of membrane thinning due to active dissolution and accumulation of plastic deformation due to the transient formation of a passive film.

The *in situ* observation setup is a useful tool to visualize the gold membrane disintegration process. Further investigation using other *in situ* techniques may provide more quantitative experimental data of the composition, structure and stress state of the oxide layer, which in turn provides useful guidance to effectively improve the operation reproducibility of this drug delivery device.

3.4 Conclusions

Combination of the *in situ* observation and bulge test provided valuable information about the gold membrane disintegration process. Real time images recorded from a CCD camera showed non-uniform corrosion occurring first around the membrane edges. More than 90% of the membranes on the 15 devices tested in PBS were opened after being corroded longer than 1 minute. The decrease in the membrane burst pressure with longer corrosion time under the bulge test confirmed a gradual loss of mechanical integrity of the gold membranes due to corrosion. The morphology observation revealed a buckled profile of the corroded membranes, which was probably correlated with the plastic deformation induced by the transient formation of a passive film on top of the gold membrane. The gold membrane electrochemical disintegration occurred by a combination of membrane thinning through active dissolution and accumulation of plastic deformation.

3.5 References

1. Santini, J.T., Jr. A controlled release microchip, Ph.D. Thesis, Massachusetts Institute of Technology, 1999.

2. Shawgo, R.S. In vivo activation and biocompatibility of a MEMS microreservoir drug delivery device, Ph.D. Thesis, Massachusetts Institute of Technology, 2004.

3. Geddes, L.A. and Roeder, R. Criteria for the selection of materials for implanted electrodes. *Annals of biomedical engineering* **31**, 879-890 (2003).

4. Tian, Z.-Q. and Ren, B. Adsorption and reaction at electrochemical interfaces as probed by surface-enhanced Raman spectroscopy. *Annual Review of Physical Chemistry* **55**, 197-229 (2004).

5. Mitrovski, S.M., Elliott, L.C.C. and Nuzzo, R.G. Micro fluidic Devices for Energy Conversion: Planar Integration and Performance of a Passive, Fully Immersed H2-O2 Fuel Cell. *Langmuir* **20**, 6974-6976 (2004).

6. Sakai, T., Kawami, Y., Takenaka, H. and Torikai, E. Effects of surface roughening of Nafion on electrode plating, mechanical strength, and cell performances for SPE water electrolysis. *Journal of the Electrochemical Society* **137**, 3777-3783 (1990).

7. Huang, Q.J., Yao, J.L., Mao, B.W., Gu, R.A. and Tian, Z.Q. Surface Raman spectroscopic studies of pyrazine adsorbed onto nickel electrodes. *Chemical Physics Letters* **271**, 101-106 (1997).

8. Egli, W.A., Visintin, A., Triaca, W.E. and Arvia, A.J. The development of facetting and roughening at platinum polyfacetted single-crystal electrodes in a chloroplatinic acid solution. *Applied Surface Science* **68**, 583-593 (1993).

9. Kershner, R.J., Bullard, J.W. and Cima, M.J. The role of electrochemical reactions during electrophoretic particle deposition. *Journal of Colloid and Interface Science* **278**, 146-154 (2004).

10. Rosenberg, A.D. In-vitro, Electrochemical Testing of a MIcrochip Based Controlled Drug Delivery Device, Master's Thesis, Massachusetts Institute of Technology, 2001.

11. Moeller, P. Electrochemical corrosion of natural gold alloys. *NATO ASI Series, Series E: Applied Sciences* **280**, 357-367 (1995).

12. Erusalimchik, I.G. Electrochemical and corrosion behavior of gold and its alloys. I. Electrochemical behavior of gold in hydrochloric acid solutions. *Protection of Metals (Translation of Zashchita Metallov)* **31**, 520-524 (1995).

13. Frankenthal, R.P. and Siconolfi, D.J. The anodic corrosion of gold in concentrated chloride solutions. *Journal of the Electrochemical Society* **129**, 1192-1196 (1982).

14. Lovrecek, B., Moslavac, K. and Matic, D. Anodic dissolution and passivation of gold, particularly in presence of chloride. *Electrochimica Acta* **26**, 1087-1098 (1981).

15. Gaur, J.N. and Schmid, G.M. Electrochemical behavior of gold in acidic chloride solutions. *Journal of Electroanalytical Chemistry and Interfacial Electrochemistry* **24**, 279-286 (1970).

16. Cadle, S.H. and Bruckenstein, S. Ring-disk study of the effect of trace chloride ion on the anodic behavior of gold in 0.2M sulfuric acid. *Journal of Electroanalytical Chemistry and Interfacial Electrochemistry* **48**, 325-331 (1973).

17. Ye, S., Ishibashi, C., Shimazu, K. and Uosaki, K. An in situ electrochemical quartz crystal microbalance study of the dissolution process of a gold electrode in perchloric acid solution containing chloride ion. *Journal of the Electrochemical Society* **145**, 1614-1623 (1998).

18. Gallego, H.J., Castellano, C.E., Calandra, A.J. and Arvia, A.J. Electrochemistry of gold in acid aqueous solutions containing chloride ions. *Journal of Electroanalytical Chemistry and Interfacial Electrochemistry* **66**, 207-230 (1975).

19. MacDonald, D.D. Passivity - the key to our metals-based civilization. *Pure and Applied Chemistry* **71**, 951-978 (1999).

20. Ahn, S., Kwon, H. and Macdonald, D.D. The role of chloride ion in passivity breakdown on nickel. *Proceedings - Electrochemical Society* **2003-25**, 66-85 (2004).

21. Fonseca, I.T.E., Lima, N., Rodrigues, J.A., Pereira, M.I.S., Salvador, J.C.S. and Ferreira, M.G.S. Passivity breakdown of Al 2024-T3 alloy in chloride solutions: a test of the point defect model. *Electrochemistry Communications* **4**, 353-357 (2002).

22. Jones, D.Y. Principles and Prevention of Corrosion, Second Edition. (Prentice Hall, Upper Saddle River, NJ; 1996).

23. Conway, B.E. Electrochemical oxide film formation at noble metals as a surface-chemical process. *Progress in Surface Science* **49**, 331-452 (1995).

24. Tremiliosi-Filho, G., Dall'Antonia, L.H. and Jerkiewicz, G. Limit to extent of formation of the quasi-two-dimensional oxide state on Au electrodes. *Journal of Electroanalytical Chemistry* **422**, 149-159 (1997).

25. Watanabe, T. and Gerischer, H. Photoelectrochemical studies on gold electrodes with surface oxide layers. Part I. Photocurrent measurement in the visible region. *Journal of Electroanalytical Chemistry and Interfacial Electrochemistry* **117**, 185-200 (1981).

26. Xia, S.J. and Birss, V.I. A multi-technique study of compact and hydrous Au oxide growth in 0.1 M sulfuric acid solutions. *Journal of Electroanalytical Chemistry* **500**, 562-573 (2001).

27. Burke, L.D. and Lyons, M.E.G. Electrochemistry of hydrous oxide films. *Modern Aspects of Electrochemistry* **18**, 169-248 (1986).

28. Conway, B.E., Barnett, B., Angerstein-Kozlowska, H. and Tilak, B.V. A surface-electrochemical basis for the direct logarithmic growth law for initial stages of

extension of anodic oxide films formed at noble metals. *Journal of Chemical Physics* **93**, 8361-8373 (1990).

29. Jerkiewicz, G. and Borodzinski, J.J. Studies of formation of very thin oxide films on polycrystalline rhodium electrodes: application of the Mott-Cabrera theory. *Langmuir* **9**, 2202-2209 (1993).

30. Moon, S.-M. and Pyun, S.-I. The mechanism of stress generation during the growth of anodic oxide films on pure aluminum in acidic solutions. *Electrochimica Acta* **43**, 3117-3126 (1998).

31. Pyun, S.I., Kim, J.D. and Oriani, R.A. Stress generation during anodic oxidation of tungsten. *Materials Science Forum* **185-188**, 407-417 (1995).

32. Nelson, J.C. and Oriani, R.A. Stress generation during anodic oxidation of titanium and aluminum. *Corrosion Science* **34**, 307-326 (1993).

33. Kim, J.-D., Pyun, S.-I. and Seo, M. Stress generation during anodic and cathodic polarization of titanium thin film electrode in pH 8.4 borate buffer solution. *Proceedings - Electrochemical Society* **2001-22**, 217-224 (2001).

34. Archibald, L.C. and Leach, J.S.L. The anodic oxidation of zirconium. I. Growth stresses in anodic zirconia films. *Electrochimica Acta* **22**, 15-20 (1977).

35. Nelson, J.C. and Oriani, R.A. Stresses produced by the anodic oxidation of nickel. *Electrochimica Acta* **37**, 2051-2057 (1992).

36. Kim, J.-D., Pyun, S.-I. and Oriani, R.A. Effects of applied current density and potential step on the stress generation during anodic oxidation of tungsten in 0.1 M H2SO4 solution. *Electrochimica Acta* **40**, 1171-1176 (1995).

37. Pilling, N.B. and Bedworth, R.E. Oxidation of metals at high temperatures. *J. Inst. Metals (advance proof)*, 54 pp (1923).

38. Stringer, J. Stress generation and relief in growing oxide films. *Corrosion Science* **10**, 513-543 (1970).

39. Kubaschewski, O. and Hopkins, B.E. Oxidation of Metals and Alloys. (1962).

40. Machalett, F., Edinger, K., Ye, L., Melngailis, J., Venkatesan, T., Diegel, M. and Steenbeck, K. Focused-ion-beam writing of electrical connections into platinum oxide films. *Applied Physics Letters* **76**, 3445-3447 (2000).

41. Mack, L.M., Reisman, A. and Bhattacharya, P.K. Stress measurements of thermally grown thin oxides on (100) silicon substrates. *Journal of the Electrochemical Society* **136**, 3433-3437 (1989).

4 *In vitro* release of BCNU

4.1 Introduction and motivation

1,3-bis(2-chloroethyl)-1-nitrosourea (BCNU), also called carmustine, is a member of the most extensively used antitumor agents[1, 2]. It was chosen as a model therapeutic compound to demonstrate the localized controlled release capability of the MEMS device *in vivo*. Because of the complex metabolic process and high cost associated with the *in vivo* studies, *in vitro* evaluation of BCNU release serves as useful controls to explain the *in vivo* study results. It also provides a quick and cheap method to investigate some of the problems encountered in the *in vivo* studies. This chapter first discusses control of ^{14}C-BCNU leakage from packaged devices, which is an important prerequisite for the release study and yet has been found to be a nontrivial task. A series of BCNU *in vitro* release experiments are presented, followed by discussion on the effects of drug formulation and packaging method on the BCNU *in vitro* release kinetics.

4.2 Experimental methods

4.2.1 Device fabrication

Devices were fabricated using the same process described in Chapter 2. The gold electrodes on some devices (from Wafer # 070103-3) were patterned by lift-off of the evaporated gold film. The electrodes on the other devices (from Wafer # 070103-6) were patterned by wet etching of the sputtered gold film.

4.2.2 Device packaging

Devices were packaged using two methods with different frame materials and packaging sequence:

(1) Stainless steel frame package

This is the same method described in Chapter 3. A neoprene gasket (1/16″ thick, McMaster-Carr Supply Co, Los Angeles, CA) was used instead of the silicone gasket because the silicone gasket was found to be permeable to BCNU in the *in vivo* release study. Accordingly, a thicker stainless steel middle frame was used to accommodate the

gasket thickness difference. A masking tape (9144, Ideal Tape Co., Lowell, MA) was also used, either alone or in combination with the neoprene gasket, to seal the filled reservoirs and test for leakage. After wire bonds were made and mechanically strengthened by epoxy (Masterbond EP42HT, Hackensack, NJ), the frames were opened for chemical filling. The devices were resealed in their frames after filling using bolts and nuts (# 000-120, Small Parts Inc., Miami Lakes, FL).

(2) Pyrex package

This method was developed to increase the capacity of the device and overcome the problem of incomplete payload release from the stainless steel frame package. Two Pyrex chips (500 μm thick) containing machined "macro-reservoirs" were bonded to the backside of the drug delivery device. A solid Pyrex plate was then bonded to the back of the macro-reservoir plate to enclose the macro-reservoirs. Chemical filling was performed along the channels machined on one of the two Pyrex chips (see Figure 4.1). The four edges of the front side of the device was connected to a stainless steel frame by epoxy for easy handling of the package and for attachment of a connector board to establish electrical connection between the device and the potentiostat.

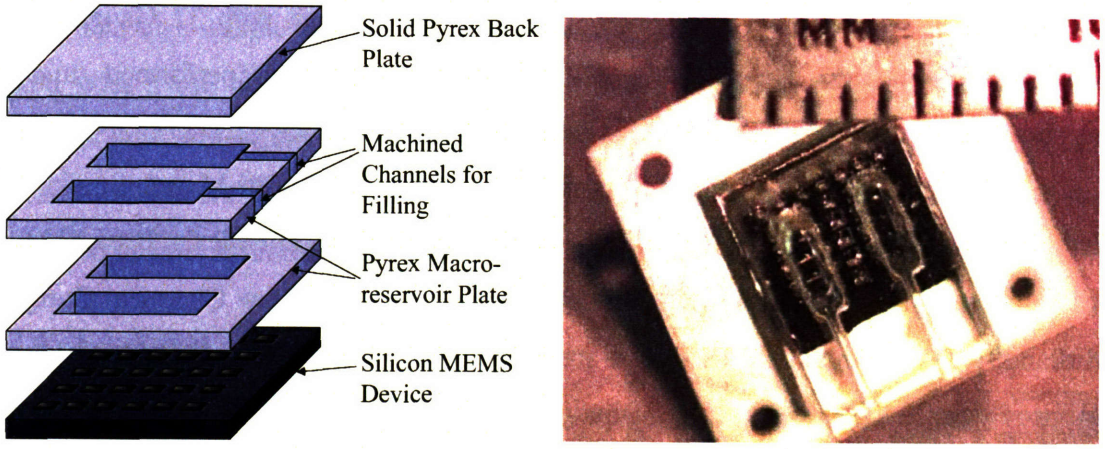

(a) (b)

Figure 4.1 (a) Schematic showing the Pyrex package design. (b) Photograph of an assembled device. Schematic drawn by Malinda Tupper. Photo taken by Lenny Rigione.

Two methods were used to bond the Pyrex chips. One method is to use UV epoxy (1-20542 cationic epoxy, Dymax Corporation, Torrington, CT). A silicone thick film with patterned grid lines was first fabricated from a silicone mold and glued onto a glass slide. A small amount of epoxy was spread along the film using a squeegee. The Pyrex chip was then coated with a thin uniform layer of epoxy by being pressed against the silicone film and lift up. The epoxy coated chip was placed on top of the Si device or another Pyrex chip and exposed under UV light (Cure Spot 50, Dymax Corporation, Torrington, CT) for 20 seconds. The bonded part was left at room temperature for 4~5 hours for the epoxy to completely cure. Another method is to use the silicon-Pyrex anodic bonding and Pyrex-Pyrex diffusion bonding, which is expected to achieve real hermetic sealing. Details about the Pyrex chip machining, anodic and diffusion bonding can be found in Ho Duc's thesis[3]. All devices for the *in vitro* release studies presented in this chapter were bonded using UV epoxy.

4.2.3 Chemical filling

Microinjection was used to fill the reservoirs using a micropump system, which consists of a UMP-1 Ultra Micro Pump with Micro-1 controller and a Kite-R micromanipulator with a TB-1 tilting base (all from World Precision Instruments, Sarasota, FL). Solutions were injected from a 10 μL syringe with 32 Gauge needles (Hamilton Company, Reno, NV). The microinjection was performed under a stereomicroscope (PZMT, World Precision Instruments, Sarasota, FL).

Chemicals used for the filling included BCNU (Bristol-Myers Squibb Co., Evansville, IN), radiolabeled BCNU (^{14}C-BCNU, Moravek Biochemicals, Brea, CA), and poly ethylene glycol (PEG, Mw 200 or 400, Carbowax™, The Dow Chemical Company, Midland, MI). For the stainless steel frame packaged devices, the sequence of chemical injection was 20 nL PEG (dissolved in ethanol, 10 vol%), 15 nL ^{14}C-BCNU (dissolved in ethanol) for 3~5 times, and 25 nL PEG (dissolved in ethanol, 80 vol%). For the Pyrex packaged devices, a mixture solution containing ^{14}C-BCNU, unlabeled BCNU, and PEG was used. The mixture solution was made by first dissolving ^{14}C-BCNU (approximately 50 μCi) and BCNU (approximately 160 mg) in ethanol (0.1~0.2 mL) in a 1 mL glass vial, mixed on a vortex machine (Vortex-Genie 2, VWR Scientific Products), and dried under

flowing nitrogen to evaporate the ethanol. The weight change of the drug containing vial was monitored on a balance (AE 100, Mettler-Toledo, Inc., Columbus, OH) to ensure complete removal of ethanol. A 10 μL syringe with 26 Gauge needles (Hamilton Company, Reno, NV) was used to dispense PEG and BCNU by the specified volume ratio in a 1 mL glass vial with tapered interior. The BCNU density was measured to be 1.2 g/mL by a microbalance. BCNU (light yellow) and PEG (clear) did not mix readily, and approximately 1-minute vortex led to a uniform mixture of the two agents with no observable color separation in the solution. The mixture solution was injected along the channel into the reservoirs. Ethanol instead of water was used as the dissolving medium because BCNU has a relatively longer half-life in ethanol (74 days[4]) than in aqueous media (10 to 20 minutes[5, 6]). PEG was initially chosen to help reduce the drying stress on the membrane. It was later found out that a more important role of PEG was to adjust the BCNU release kinetics, as discussed in Section 4.3.3.

The actual ^{14}C-BCNU activity ordered from Moravek usually deviates from the specified value and tends to change from one order to another. Therefore, the actual activity was checked for each order by scintillation counting of a known volume of ^{14}C-BCNU/ethanol solution. Each time packaged devices were filled, 2 or 3 bare devices were also filled with the same amount of radioactive solution to serve as dosage controls.

The test sample for the ^{14}C detection was placed in a 7 mL scintillation vial, mixed with 5 mL ScintiSafe fluid (Fisher Scientific, Atlanta, GA), and counted on a Packard Tri-Carb liquid scintillation analyzer (Model 2200CA, Perkin-Elmer Life Sciences, Downers Grove, IL). Raw DPM (disintegrations per minute) data were converted to activity in microcuries (μCi) by a conversion factor of 2.2×10^6 DPM/μCi.

4.2.4 Leak test

In vitro leak testing was performed to evaluate the hermeticity of the packaged devices filled with ^{14}C-BCNU. Devices were filled and packaged without attachment of the connector boards. The four outer edges of the stainless steel package were covered by the 2-component epoxy (Masterbond EP42HT, Hackensack, NJ), and the edges of the Pyrex package covered by UV epoxy. Packaged devices were immersed in a 20 mL glass vial with 16 mL DI water (or PBS solution) placed on a stirrer with mild stirring (stirrer

setting at ~3) to ensure thorough mixing. One mL samples were taken at pre-determined time points (3-4 times on the first day and once every day on following days), and the testing medium replenished with 1 mL DI water (or PBS) after removal of each aliquot. The sample ^{14}C content was analyzed by scintillation counting as described in the previous paragraph. The leakage percent was calculated for each packaged device, with the total ^{14}C loading determined from scintillation counting of control devices that were filled with the same volume of solution and at the same time when devices for the leak testing were filled. The leak test was performed at either room temperature or 37 °C by keeping the glass vial in a water bath.

4.2.5 *In vitro* release studies

Each packaged device filled with ^{14}C-BCNU was placed in a 20 mL glass vial containing 16 mL PBS (0.15 M Cl^-, pH=7.2) mildly stirred (stirrer setting at ~3). Devices were activated using the same voltammetry profile described in Chapter 3, with 4 cycles of cathodic cleaning from –1.0 to –1.5 V, 4 cycles of diagnostic scan from 0 to 1.5 V, and 10-minute square wave voltammetry between 0 and 0.8 V. All potentials were relative to a blackened Pt wire placed about 5 mm away from the device in the same PBS containing glass vial. One mL samples were taken more frequently immediately after activation (every 20 or 30 minutes) than at later times (2 or 3 times a day). One mL PBS was added to the release medium after removal of each aliquot. The sample ^{14}C content was analyzed by scintillation counting as described in Section 4.2.3. The percentage of payload release was calculated, with the total ^{14}C loading determined from scintillation counting of control devices that were filled with the same volume of solution and at the same time when devices for the release studies were filled.

4.3 Results and discussion

4.3.1 Origin of ^{14}C-BCNU leakage

Leakage of ^{14}C-BCNU was found in the first *in vivo* release study and the cause was attributed to the silicone gasket being permeable to BCNU[7]. Soaking a device packaged using the silicone gasket in water led to 50% leakage of the radioactivity within 24 hours. Different sealing materials were tested to find a better gasket material. The

neoprene gasket seemed to have better sealing property than the 9144 tape. However, there was still an appreciable amount of leakage within 2 days, as shown in Figure 4.2.

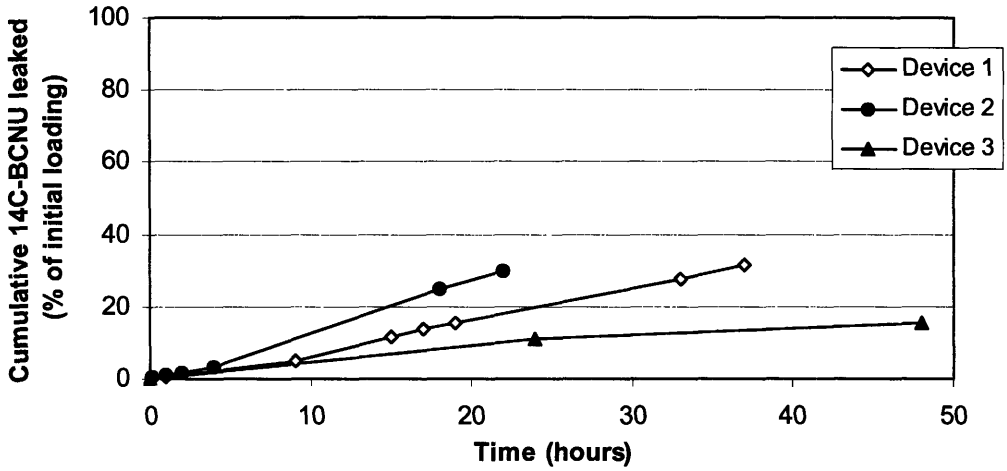

Figure 4.2 Leak test of stainless steel frame packaged devices with different gasket sealing materials. Device 1 was sealed using neoprene gasket and 9144 tape, Device 2 sealed using only 9144 tape, and Device 3 sealed using only neoprene gasket. Each device was filled with 0.31 μCi ^{14}C-BCNU. Test performed at 37 °C in PBS.

Leakage of ^{14}C-BCNU was still observed for packaged devices with all inner and outer edges of steel frames covered by epoxy, and was stopped only when all the gold membranes were also covered by epoxy, as shown in Figure 4.3.

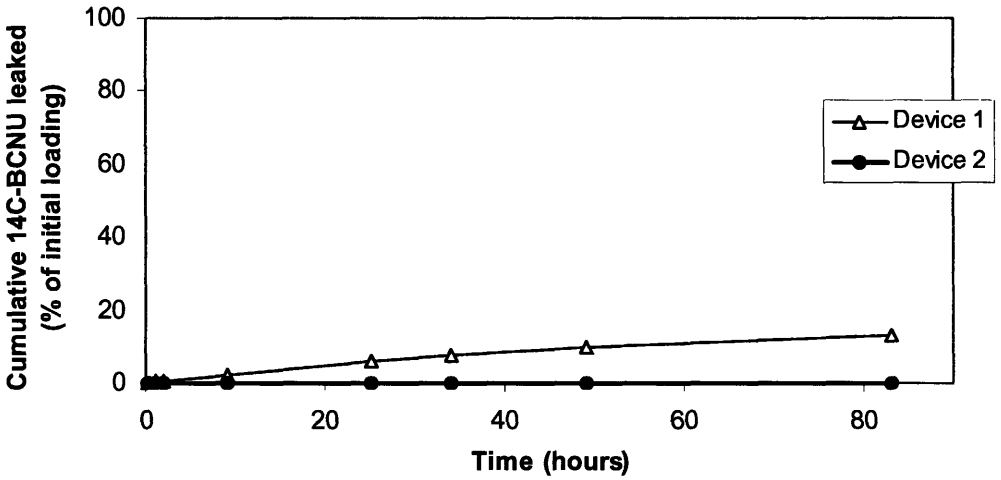

Figure 4.3 Leak test of stainless steel frame packaged devices sealed using neoprene gasket. Device 1 had all inner and outer edges of steel frames covered by epoxy, and Device 2 had all inner and outer edges of steel frames, and all gold membranes covered by epoxy. Each device filled with 0.31 μCi ^{14}C-BCNU. Test performed at 37 °C in PBS.

Further optical microscopy observation of the gold membranes revealed two types of morphologies after the reservoirs were filled with ^{14}C-BCNU. Most of the membranes remained smooth and shiny as they were before the filling (Figure 4.4). A few other membranes however, showed some stained pattern after the filling (Figure 4.5).

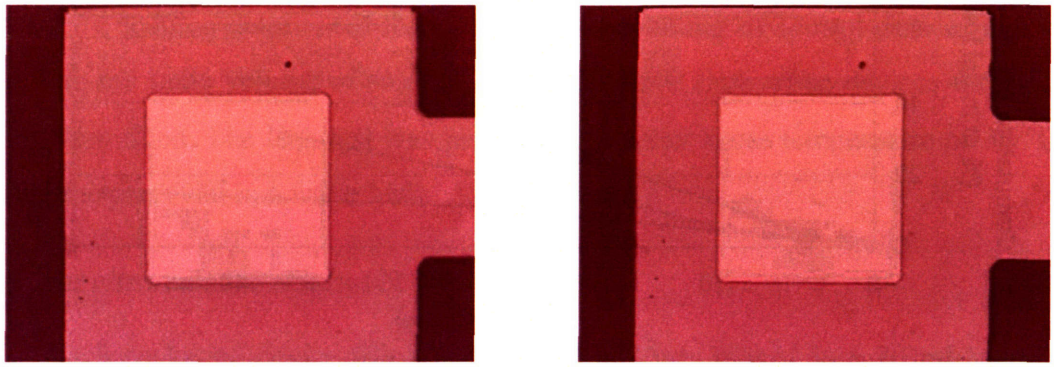

(a) (b)

Figure 4.4 Optical micrographs of a gold membrane (a) before and (b) after ^{14}C-BCNU/ethanol solution was filled, showing no change in the membrane morphology.

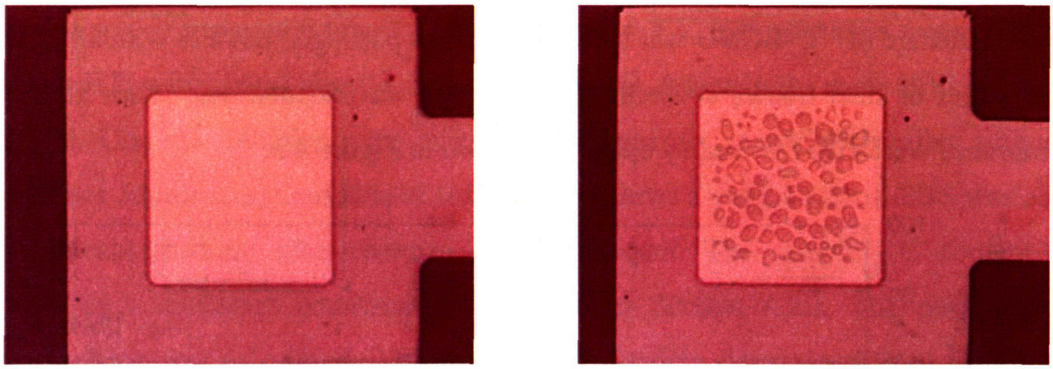

(a) (b)

Figure 4.5 Optical micrographs of a gold membrane (a) before and (b) after ^{14}C-BCNU/ethanol solution was filled, showing stained morphology after the filling.

When the stained membranes were covered by epoxy, a dramatic decrease in the leakage rate was observed (see Figure 4.6). All these results indicated that the defects on the gold membranes were an important source of leakage for the small molecule ^{14}C-BCNU (Mw=181). These defects allow the penetration of the ethanol solution (containing ^{14}C-BCNU) through the gold membranes to the surface and leave stains after the ethanol evaporates.

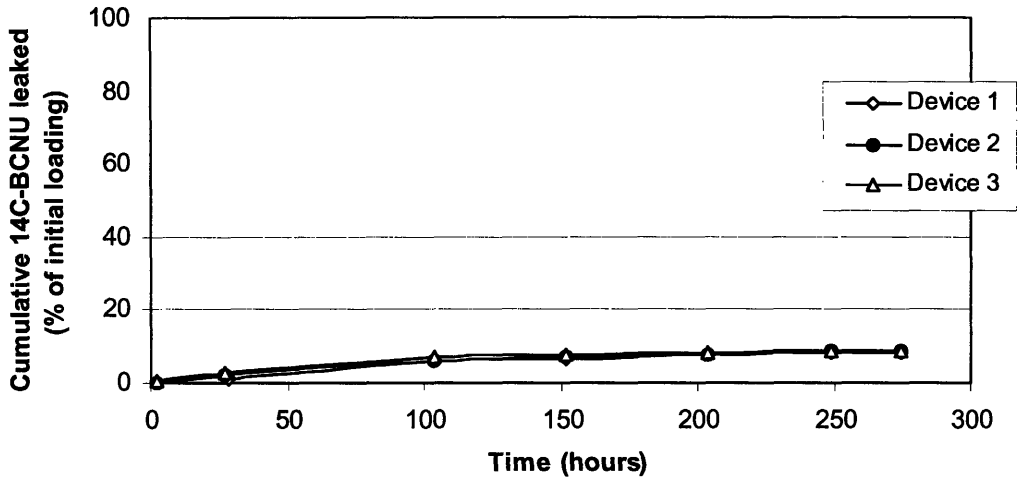

Figure 4.6 Leak test of three stainless steel frame packaged devices patterned by lift off, sealed using neoprene gasket, with all inner and outer edges of steel frames, and all stained gold membranes covered by epoxy. Device 1 and Device 2 each filled with 0.0315 μCi ^{14}C-BCNU loading, and Device 3 filled with 0.015 μCi ^{14}C-BCNU loading. Test performed at room temperature in deionized water.

All the leak tests described above were performed on devices with evaporated gold membranes. On average, 5 evaporated gold membranes were stained if all the 34 reservoirs were filled with the ^{14}C-BCNU/ethanol solution for one device. In contrast, at most 2 sputtered gold membranes were observed to be stained if all the 34 reservoirs were filled with the same volume of ^{14}C-BCNU/ethanol solution for one device. Leak test on a packaged device with sputtered gold membranes also showed a lower leakage rate (~7% over one month, see Figure 4.7) than devices with evaporated gold membranes (~10% over 10 days, see Figure 4.6). All this indicates that wafers with sputtered gold films (electrode patterning by wet etching) indeed have a higher device yield and better membrane quality than wafers with evaporated gold films (electrode patterning by lift off).

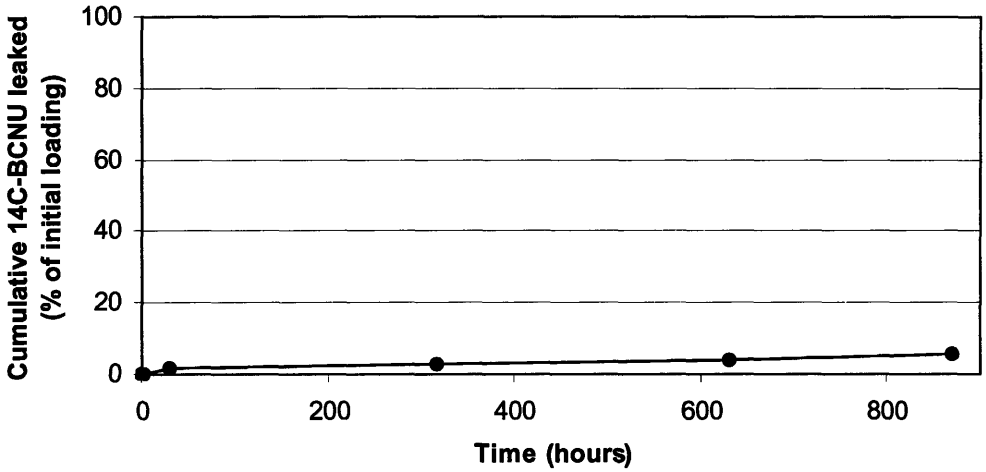

Figure 4.7 Leak test of one stainless steel frame packaged device with sputtered gold membranes patterned by wet etching, sealed using neoprene gasket, with all inner and outer edges of steel frames. Device filled with 0.012 μCi ^{14}C-BCNU. Test performed at room temperature in deionized water.

Figure 4.8 shows the leak test result on two stainless steel frame packaged device with sputtered gold membranes. The much higher percentage of ^{14}C-BCNU leakage arises from two differences: One difference is that the inner edges of the steel frames on this device were not covered by epoxy. The other difference is a much larger mass contained in each filled reservoir of these two devices. For all the other devices tested before Figure 4.8, each filled reservoir contained 2 nL PEG and about 2 nCi ^{14}C-BCNU. The mass for 2 nCi ^{14}C-BCNU is 6.8 ng calculated according to the specific activity of ^{14}C-BCNU (53 mCi/mmol). For the devices tested in Figure 4.8, besides the 2 nL PEG and 6.8 ng ^{14}C-BCNU, another 20 nL PEG was filled so each reservoir was almost full. The much higher leakage rate for the devices in Figure 4.8 clearly showed that the stainless steel package was leaky, most probably because the neoprene gasket did not form a hermetic seal against the filled reservoirs. Although covering the inner edges of the steel frames can solve the package leak problem, it is not an ideal solution. When sequential release of payload from different rows of filled reservoirs is desired, opening one row can lead to outflow of the payload from adjacent rows of reservoirs through the opened membranes.

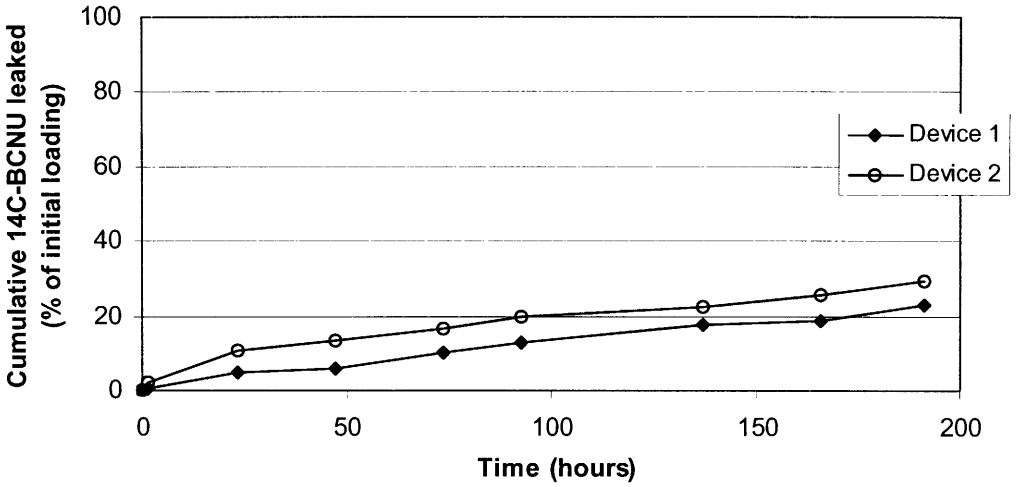

Figure 4.8 Leak test of two stainless steel frame packaged devices sealed using neoprene gasket, with all outer edges of steel frames. The ^{14}C-BCNU for both devices was 0.022 μCi. Each filled reservoir also contained 22 nL PEG. Test performed at room temperature in deionized water.

Figure 4.9 shows the leak test of a Pyrex packaged device. The leakage rate of ^{14}C-BCNU before Day 12 was essentially zero, indicating good hermeticity of the package. The abrupt increase in the leakage percentage after Day 12 suggests that the UV epoxy was not durable to resist the attack of BCNU for long time. It is hoped that the anodic and diffusion bonding method will lead to real long term hermetic seal of the package.

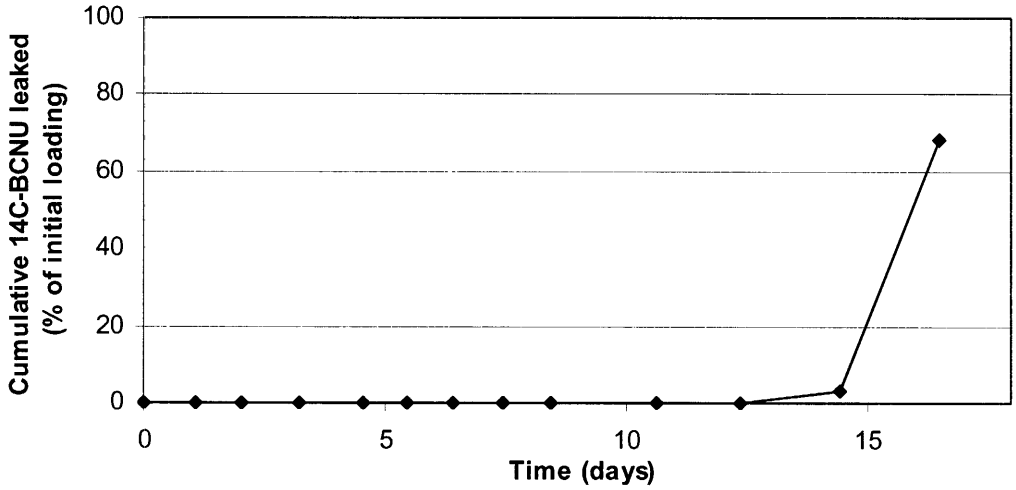

Figure 4.9 Leak test of one Pyrex packaged device filled with 2 μL mixed solution of BCNU and PEG with 80:20 volume ratio and a total radioactivity of 0.25 μCi ^{14}C-BCNU. Test performed at room temperature in deionized water.

4.3.2 *In vitro* BCNU release kinetics

4.3.2.1 Stainless steel frame packaged devices

Two *in vitro* release tests were performed on the stainless steel frame packaged devices. The first test studied the release kinetics of ^{14}C-BCNU from devices filled with predominantly PEG in volume (22 nL) relative to ^{14}C-BCNU (less than 2 nL), as shown in Figure 4.10. Each activation was followed by a rapid increase in the ^{14}C counting and establishment of equilibrium within 30 minutes after activation. Approximately 40 % of the initial ^{14}C loading was detected from the release medium, although all the membranes were opened as confirmed by the optical microscopy examination. The remaining 60 % was recovered by subsequently soaking the unpackaged devices in saline and analyzed by scintillation counting. The neoprene gasket was found to contain most of the radioactivity, with 45 % of the radioactivity recovered after soaking for three days. The inner edges of the steel frames of the two packaged devices were not covered by epoxy. Although there was concern about the cross-talking between neighboring rows due to incomplete seal, the radioactivity measurement did not show obvious difference in the amount of ^{14}C released from each row, probably because the time interval between each activation was too short for the cross-talking to show an effect.

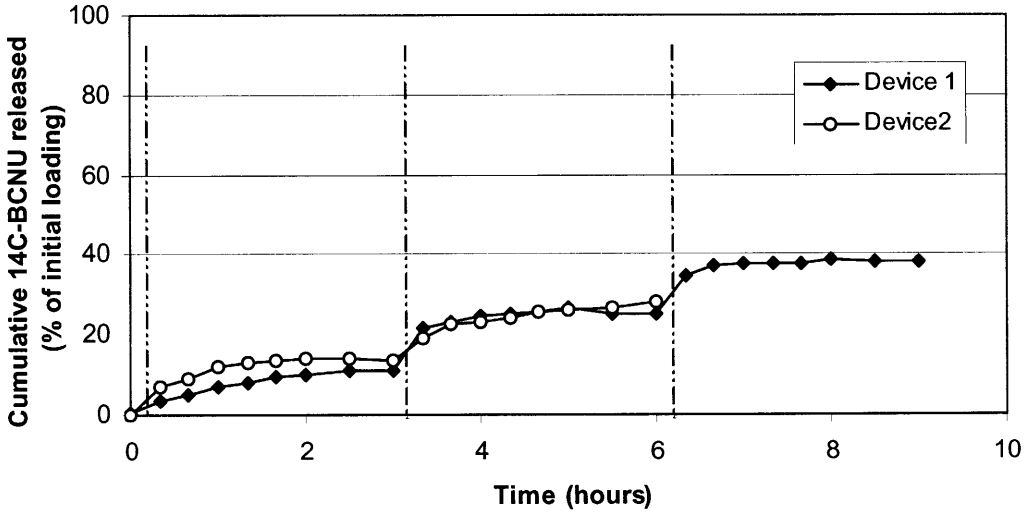

Figure 4.10 Cumulative percentages of ^{14}C-BCNU released from two devices packaged using stainless steel frames and neoprene gasket. Each activation (denoted by the dashed line) corresponds to opening of one row of reservoirs with 0.01 μCi loading. Each filled reservoir also contained 22 nL PEG. Test performed at room temperature in PBS.

The second test evaluated the ^{14}C-BCNU release kinetics from devices filled with different volume ratio BCNU/PEG (see Figure 4.11). The silicone gasket was used instead of the neoprene gasket to seal the reservoirs. Although the silicone was known to be permeable to BCNU, it was expected that the much thinner silicone gasket (125 μm thick) would not trap as much radioactivity as the neoprene gasket (1.58 mm thick). The results show an interesting trend of higher percentage of ^{14}C-BCNU released with higher percentage of PEG in the initial formulation. The time to reach plateau ^{14}C level was also faster with more PEG added into the reservoir.

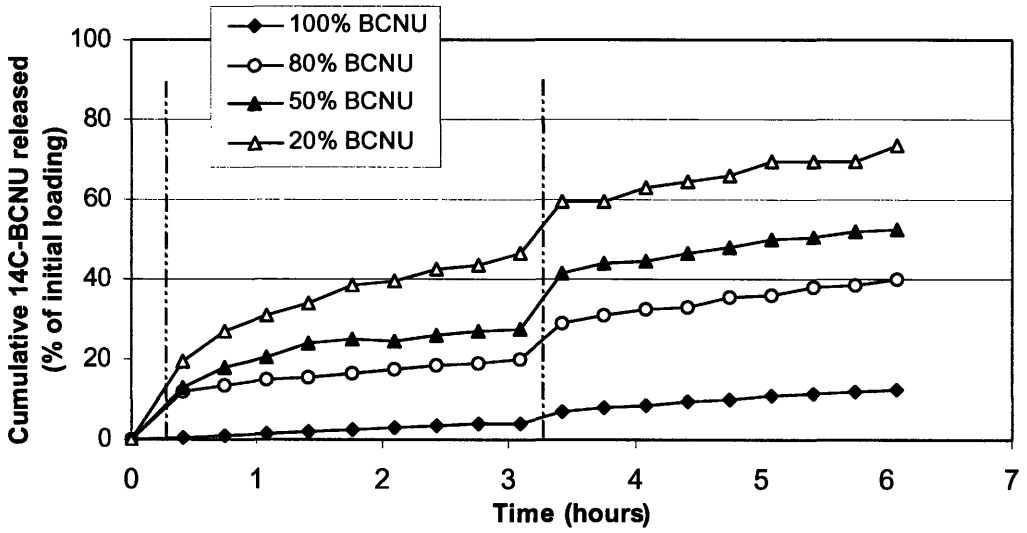

Figure 4.11 Cumulative percentages of ^{14}C-BCNU released from four devices packaged using stainless steel frames and silicone gasket. Each activation (denoted by the dashed line) corresponds to opening of 10 reservoirs with half of the initial loading. Each filled reservoir contained 20 nL mixed solution of ^{14}C-BCNU/BCNU/PEG with different BCNU/PEG volume ratio. Test performed at room temperature in PBS.

4.3.2.2 Pyrex packaged devices

The Pyrex package allows the *in vitro* release test to be performed with longer time interval between activations. The Cumulative release results of ^{14}C-BCNU from 4 Pyrex packaged devices are shown in Figure 4.12. Incomplete release of payload and sluggish kinetics were observed for the devices filled with 100 % BCNU. In contrast, the other three devices showed close to 100 % release of the radioactivity. The time to reach equilibrium ^{14}C level was fastest for the device filled with 80 % PEG (approximately 6

hours), and slightly longer for the other two devices filled with 50 % and 20 % PEG (15 ~ 20 hours).

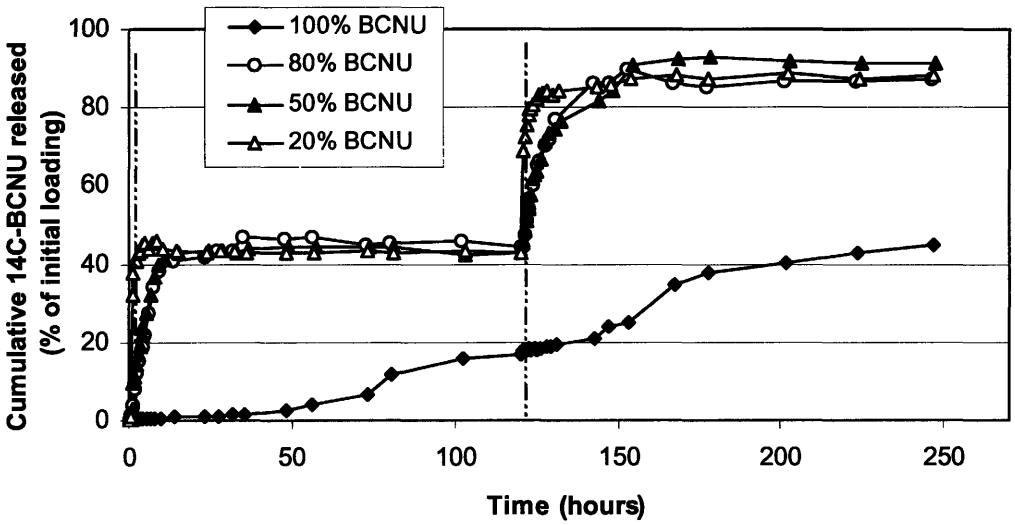

Figure 4.12 Cumulative percentages of ^{14}C-BCNU released from four devices packaged using Pyrex plates. Each activation (denoted by the dashed line) corresponds to opening of 10 microreservoirs with half of the initial loading. Each device was filled with a mixed solution of ^{14}C-BCNU/BCNU/PEG with different BCNU/PEG volume ratio. The BCNU loading was 1.2 mg in each of the three devices (100 % BCNU, 80 % BCNU and 50 % BCNU) and 0.96 mg in the device with 20 % BCNU. Test performed at room temperature in PBS.

4.3.2.3 Effects of drug formulation and packaging method

In vitro release results from the previous two sections clearly show that co-formulation of Polyethylene glycol (PEG) greatly enhanced the BCNU release kinetics, in terms of both the percentage of payload release and the time to reach equilibrium ^{14}C level. The sluggish release kinetics from devices filled with 100 % BCNU can be explained by the high lipophilicity (or hydrophobicity) of BCNU. PEG is a non-toxic water soluble polymer. Conjugating biomolecules with PEG, a process known as PEGylation, is an established method for improving the pharmacokinetics and pharmacodynamics of many protein and liposomal drugs[8]. Although the BCNU in our study was not PEGylated, the presence of PEG helped to drive the out diffusion of BCNU when the membranes were opened, leading to more complete and rapid release of payload.

The Pyrex package also showed obvious advantages over the stainless steel framed package. The capacity of the Pyrex packaged devices was greatly increased comparing to the stainless steel frame packaged devices because of the addition of the two macroreservoirs with an approximate volume of 9 μL, which is much larger than the total volume of the 34 microreservoirs (0.85 μL). Addition of the Pyrex plates increased the thickness of the package. But this increase was offset by the decrease in the lateral dimension of the package due to elimination of the steel frames. The overall volume of the Pyrex package is in fact smaller than the steel frame package. One limitation is that only two release events can be achieved with the current Pyrex package, yet it is possible to modify the design and increase the number of macroreservoirs on one Pyrex chip in order to achieve more independent release events.

Another advantage of the Pyrex package is the more complete release of payload. With the same BCNU/PEG formulation, the time to reach plateau ^{14}C-BCNU level after activation for the Pyrex packaged devices (several hours) was longer than for the stainless steel frame packaged devices. One possible reason is that the drug mixture was directly injected into each microreservoir for the stainless steel frame packaged devices. Whereas it was impossible to directly address individual microreservoir when filling along the channels on the Pyrex chip and completely fill the micro and macroreservoirs (as the BCNU/PEG solution tended to creep along the channel and wet the end of the channel when the reservoirs are close to full, which prevented sealing). After the membranes were opened, the remaining air bubbles inside the reservoirs could hinder the out diffusion of BCNU, delaying the time to reach equilibrium.

4.4 Conclusions

The *in vitro* leak test results presented in this chapter illustrate the importance of fabricating high quality gold membranes through processing optimization. Co-formulation of polyethylene glycol (PEG) with BCNU effectively enhanced the release kinetics of BCNU *in vitro*. The Pyrex package demonstrated obvious advantages over the stainless steel frame package with greatly increased capacity and more complete payload release. Results from these experiments serve as controls as well as useful guidance for

the *in vivo* BCNU release kinetics study and tumor effect study presented in the next two chapters.

4.5 Acknowledgements

Hong Linh Ho Duc fabricated all the Pyrex chips used in this chapter's study. Dr. Malinda Tupper fabricated the silicone thick film used for coating the UV epoxy onto the Pyrex chips.

4.6 References

1. Barnhart, E.R. and Huff, B.B. Physicians' Desk Reference, Edition 48. (Medical Economics Company, Oradell, NJ; 1988).
2. Carter, S.K., Schabel, F.M., Jr., Broder, L. and Johnston, T.P. 1,3-Bis(2-chloroethyl)-1-nitrosourea (BCNU) and other nitrosoureas in cancer treatment. Review. *Advances in Cancer Research* **16**, 273-332 (1972).
3. Ho Duc, H.L. Packaging for a drug delivery microelectromechanical system, Master's Thesis, Massachusetts Institute of Technology, 2004.
4. Montgomery, J.A., James, R., McCaleb, G.S. and Johnston, T.P. Modes of decomposition of 1,3-bis(2-chloroethyl)-1-nitrosourea and related compounds. *Journal of Medicinal Chemistry* **10**, 668-674 (1967).
5. Montgomery, J.A., James, R., McCaleb, G.S., Kirk, M.C. and Johnston, T.P. Decomposition of N-(2-chloroethyl)-N-nitrosoureas in aqueous media. *Journal of Medicinal Chemistry* **18**, 568-571 (1975).
6. Laskar, P.A. and Ayres, J.W. Degradation of carmustine in mixed solvent and nonaqueous media. *Journal of Pharmaceutical Sciences* **66**, 1076-1078 (1977).
7. Shawgo, R.S. *In vivo* activation and biocompatibility of a MEMS microreservoir drug delivery device, Ph.D. Thesis, Massachusetts Institute of Technology, 2004.
8. Molineux, G. Pegylation: engineering improved biopharmaceuticals for oncology. *Pharmacotherapy* **23**, 3S-8S (2003).

5 Release kinetics of ^{14}C-BCNU *in vivo*

5.1 Introduction and motivation

Understanding the release kinetics of BCNU from the MEMS device is important as it may differ from the known pharmacokinetics of BCNU administered by injection or other methods. For the *in vitro* release of ^{14}C-BCNU presented in the previous chapter, all the released radioactivity can be collected from the release medium for direct analysis of the release kinetics. The drug released from the devices *in vivo*, however, experiences metabolism, partition among different organs, and excretion. This necessitates a good understanding of the *in vivo* pharmacokinetics of ^{14}C-BCNU in order to choose an appropriate model to study its release kinetics from the drug delivery device *in vivo*.

Available pharmacokinetic data using ^{14}C-BCNU indicate that the compound and its metabolites are accumulated in the liver, kidney and lungs, and that approximately 78% of a radioactive dose injected intraperitoneally, subcutaneouly, or taken orally, is excreted from mice within 24 hours. The plasma ^{14}C concentration, though only a small portion (1-5%) of the dose, remains constant in the plasma for relatively long duration with a 67-hour half life[1]. It is therefore appropriate to measure pulses of BCNU release from the drug delivery device using plasma samples to obtain the temporal release kinetics. This approach however is limited by the relatively low sensitivity of the conventional liquid scintillation counting (LSC) with respect to the low plasma ^{14}C level. An alternative tool of isotope detection is the accelerator mass spectrometry (AMS), a highly sensitive method for quantifying extremely low concentrations of radioisotopes with ultrahigh precision[2, 3]. This chapter introduces a collaborative study to utilize the AMS facility at Lawrence Livermore National Laboratory (LLNL) for evaluating the release kinetics of ^{14}C-BCNU *in vivo*[4].

5.2 Experimental methods

5.2.1 Device fabrication and packaging

Devices (from Wafer # 070103-3) were fabricated using the same process described in Chapter 2. The gold electrodes were patterned by lift-off of the evaporated

gold film. Devices were packaged into stainless steel frames with neoprene gaskets (McMaster-Carr Supply Co, Los Angeles, California) to seal the reservoirs. Wirebonds connected the bondpads on the device to connector boards and Teflon coated cables (UT3201TFK16, Axon' Cable Inc., Schaumburg, IL). Wirebonds were mechanically protected and electrically isolated with epoxy (Masterbond EP42HT, Hackensack, NJ). A blackened platinum wire (approximately 6mm long) was soldered to exposed end of one cable with epoxy covering the soldering joint to be used as an *in vivo* reference electrode.

Four devices were filled with ethanol solutions of PEG (Mw 200) and ^{14}C-BCNU (Moravek Biochemicals Inc., Brea, CA) using a UMP-1 Ultra Micro Pump with Micro-1 controller and a Kite-R micromanipulator with a TB-1 tilting base (all from World Precision Instruments, Sarasota, FL) under the stereomicroscope. Each device had three rows of reservoirs filled, with each row containing 0.01 μCi ^{14}C-BCNU. Each filled reservoir also contained 22 nL PEG.

5.2.2 Animal protocol

The *in vivo* release study was performed in Dr. Henry Brem's group at Johns Hopkins Medical Institutions (JHMI). The animal study protocol was approved by the Animal Care and Use Committee of JHMI before implementation of any procedure.

Female rats (Fisher 344, weight 150~200 g) were purchased from Charles River. Animals were given standard rat chow and water *ad libitum* at the JHMI Animal Facilities.

Devices were sterilized by gamma irradiation using a Mark1-68 irradiator (JLS Shepherd, Glendale, CA) with a Cerium 137 source for a total dose of 40 Gray. Prior to surgery, the rats were anesthetized with an intraperitoneal injection of 0.6 mL of a stock solution of ketamine hydrocholoride 25 mg/ml, xylazine 2.5 mg/ml, and 14.25 % ethyl alcohol diluted in 0.9 % NaCl solution. The skin of the left flank was shaved and prepped with betadine. Under sterile conditions, an incision (approximately 1 cm) was made in the skin of the flank to form a subcutaneous pocket caudally. Devices were implanted subcutaneously with the electrodes facing the anterior flank and the cable exiting through the incision. The incision was closed with autoclips. Post-operative analgesics were given following every surgical procedure using a subcutaneous injection of buprenorphine

(0.1 mg/kg). All operating procedures were performed using sterile technique, with all instruments autoclaved and sterile gloves and masks worn throughout the procedure.

Activations were performed on three devices at 3-hour intervals. The applied voltammetry included four cathodic cleaning cycles from –1.0 to –1.5 V, four diagnostic scan cycles from 0 to 1.8 V, and 10-minute square wave voltammetry between 0.2 and 1.4 V, all relative to the blackened Pt wire reference electrode.

The femoral artery catheterization was performed on each rat one hour before the device activation. A small incision was made into the femoral artery to allow insertion of a catheter that was used to remove blood samples and inject sterile saline. Blood samples of 100 μL were taken every 20 to 30 minutes before and after each activation. Sterile saline with 10 vol% heparin was injected through the catheters after taking each blood sample to replace the blood volume lost as well as to keep the catheters from clogging. The rats need to be kept at the anesthetized state by injection of 0.2 mL anesthetic solution every two hours because their movement could displace the catheter and affect the blood sample taking process. This catheterization procedure was problematic until the technique could be perfected as two rats expired before completing all the scheduled activations. Blood samples were centrifuged at 6000 rpm for 5 minutes to yield approximately 75 μL plasma for each sample. The plasma ^{14}C concentration was measured by AMS, as described in the section below.

Controls included animals with an unactivated device and with subcutaneously injected ^{14}C-BCNU. The study was designed to have one rat receive three subcutaneous injections of 0.15 mL sterile saline solution containing 0.01 μCi ^{14}C-BCNU at 3-hour intervals. It was later found out that the ^{14}C-BCNU stock received from Moravek had a higher activity than the specified value. The actual ^{14}C loading for each injection was 0.014 μCi as determined by LSC. Two devices activated *in vitro* in saline were used as *in vitro* controls.

Animals were euthanized by either CO_2 inhalation or a sodium pentobarbital overdose (200 mg/kg, to effect) at the conclusion of experiments. Devices were explanted and shipped to MIT for optical microscopy inspection (Olympus BH-2).

5.2.3 AMS analysis of plasma ^{14}C concentration

Detection of ^{14}C (half life 5760 years) can be made either by measuring the decay (such as liquid scintillation counting, or LSC) or by directly counting the radiocarbon atoms using the Accelerator Mass Spectrometry (AMS). Use of LSC on small samples with low ^{14}C activity is often limited by high backgrounds, low specificity and low counting efficiency. On the other hand, AMS can detect one ^{14}C ion in a quadrillion (10^{15}) other ions (equivalent to 0.14 DPM) with a precision of 0.5~1%[5]. The high detection sensitivity (10^5 to 10^6 higher than LSC) arises from the design of the spectrometer, which allows the molecular dissociation process at the accelerator and charge detection at the end (see Figure 5.1). A number of studies have also validated the AMS against LSC for analyzing ^{14}C labeled drugs in human and animal body fluids with superior analytical sensitivity and accuracy[6-8].

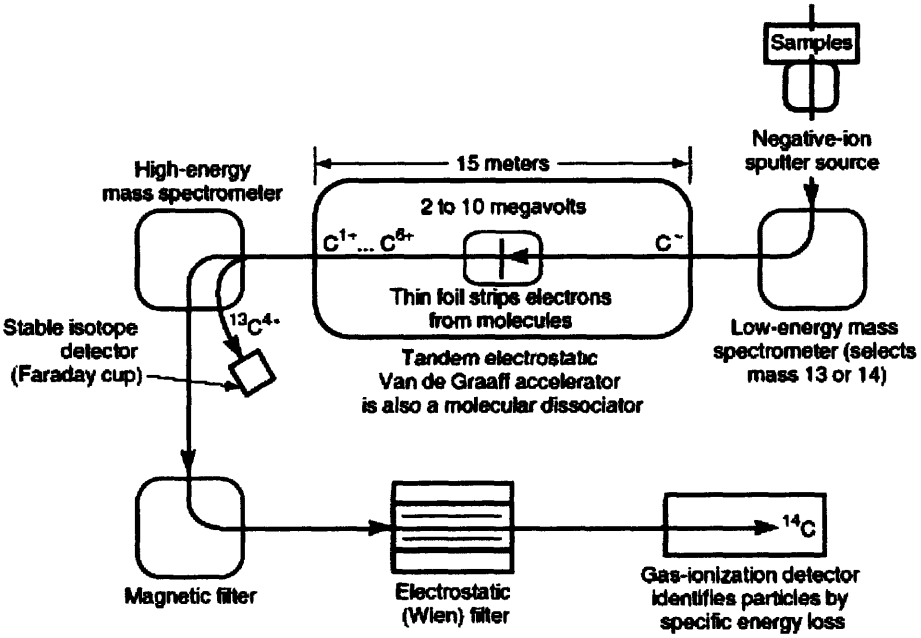

Figure 5.1 Schematic of the accelerator mass spectrometer for ^{14}C detection. Courtesy of Paul Henderson.

The high sensitivity of AMS requires strict contamination control in the sample preparation and handling to maintain sample integrity[9]. This was especially important in our study where high ^{14}C level work (for LSC of the urine samples) had been performed. Nine swipes were taken of all the work area related to the *in vivo* test, including cages,

the centrifuge equipment, doorknobs, sink handles, the microscope stage and workbench. These swipes and three blank blood samples were analyzed by AMS. The results showed acceptable contamination control level except the centrifuge equipment. In the subsequent release kinetics study, great care was taken to avoid contact of the pipette with the outside of the centrifuged Eppendorf tube when transferring the plasma samples.

A pilot study was also conducted on AMS analysis of 5 plasma samples from a rat with one subcutaneous injection of 0.6 nCi ^{14}C-BCNU (dissolved in 0.1 mL ethanol) and 6 plasma samples from a rat with one activated device filled with approximately 0.6 nCi ^{14}C-BCNU loading. The purpose of the pilot study was to establish experimental protocols of using AMS for the release kinetics study.

The AMS analysis was made at the Center for Accelerator Mass Spectrometry at LLNL. Plasma samples shipped from JHMI were thawed at room temperature, vortexed and centrifuged in order to obtain a homogeneous liquid sample. A 25 μL aliquot of each sample was placed in a quartz tube and dried by vacuum centrifuge. The sample was converted to CO_2 by combustion, and was quantitatively reduced to graphite in the presence of zinc and titanium hydride condensing onto catalytic iron at ~500 °C for 4 hours[10]. The graphite samples were introduced into the spectrometer for three to seven replicate measurements to a precision of 3 % or better.

AMS measures an isotope ratio, expressed as ^{14}C per mass of carbon[5]:

$$R_{measure} = \left(\frac{^{14}C}{C}\right)_{measure} = \frac{^{14}C_{trace} + ^{14}C_{natural}}{C_{trace} + C_{natural}} \approx \frac{^{14}C_{trace} + ^{14}C_{natural}}{C_{natural}} = \frac{^{14}C_{trace}}{C_{natural}} + R_{natural}$$

(Equation 5.1)

where $^{14}C_{trace}$ and C_{trace} are the radioactivity and mass of sample, and $^{14}C_{natural}$ and $C_{natural}$ the radioactivity and mass of the control sample of a similar tissue. C_{trace} can be neglected because usually a picomole (10^{-12}) or less radiolabeled compound is contained in milligram-sized samples. $R_{natural}$ in our study used the AMS measurement of the baseline plasma sample for each rat that was taken prior to the device implantation or injection. The unit of the AMS measurement is called "Modern". 1 Modern is equivalent to 6.11 fCi ^{14}C/mg carbon, or 97.89 amol ^{14}C/mg carbon[5]. The plasma ^{14}C concentration (unit: fCi/μL), therefore, can be calculated by:

$$Plasma\ ^{14}C\ conc. = (R_{measure} - R_{natural}) \times 6.11 \frac{fCi}{mg\,C} \times C\% \times Plasma\ density$$

(Equation 5.2)

Plasma normally contains 3% carbon by weight. The plasma samples in our study, however, also contained a small amount of heparin (a carbon containing compound). Total percent carbon in the blood plasma was measured with an Exeter CE-440 elemental analyzer (Exeter Analytical, Inc., Chelmsford, MA) to 3.28 percent (+/- 0.63), as determined in selected samples taken throughout each experiment. A value of 3.28% was used for the calculation. The plasma density is 1.01 mgC/μL.

5.3 Results and discussion

5.3.1 Pilot study results

Figure 5.2 shows the pilot study results. Subcutaneous injection of 0.6 nCi ^{14}C-BCNU led to increase of the plasma ^{14}C concentration, which seemed to reach a plateau within 3 hours. This plasma ^{14}C concentration of the rat with the activated device, however, was not significantly higher than the background level throughout the 3-hour measurement. The *in vitro* release studies in Chapter 4 showed incomplete of payload release from devices packaged using the stainless steel frames and neoprene gaskets. Besides, the packaged device was soaked in water for 2 days to test leakage before the device implantation. The LSC data showed slightly higher than background values (~ 50 DPM). But it was difficult to determine the exact amount of ^{14}C-BCNU leaked because the initial total loading was too low. All these were possible factors leading to the lower plasma ^{14}C level in the rat with the activated device than in the subcutaneous injected control. Nevertheless, the injected control result was encouraging and clearly demonstrated the high sensitivity of AMS with respect to low ^{14}C detection. It was also determined from this study that the suitable plasma sample size for AMS analysis was 25 μL as it showed the lease variation among repeated measurements.

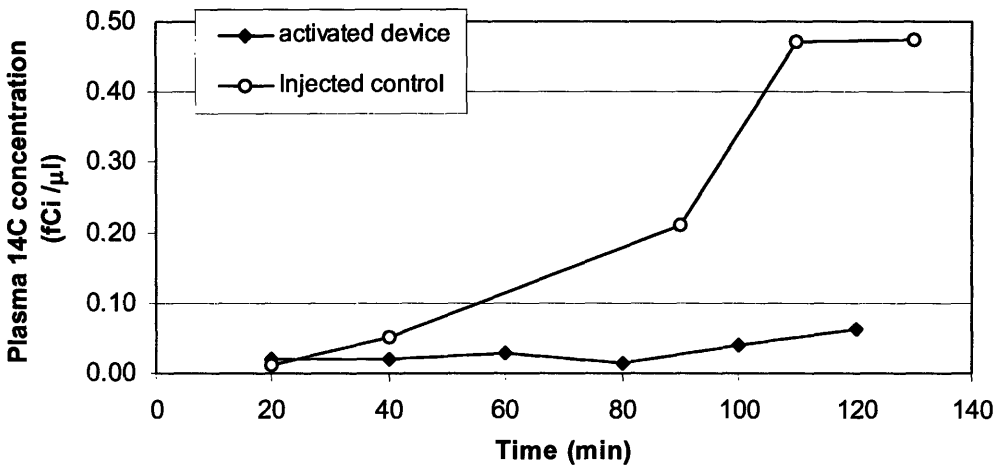

Figure 5.2 Plasma ^{14}C concentration measured by AMS from a device activated *in vivo* and a subcutaneous injected control. Both the activation and injection started at time zero. Each data point represents means of 3~7 replicate measurements with 25 µL plasma sample.

5.3.2 *In vivo* release of ^{14}C-BCNU

Six activations, each corresponding to the opening of one row of three or four reservoirs with a total loading of 0.01 µCi ^{14}C per row, were performed on three rats. Five out of these six activations were successful with all of the membranes opened, as confirmed by the optical microscopy observation of the explanted devices. The unsuccessful activation was due to faulty wiring on a single row of one device. Figure 5.3 shows the temporal profile of *in vivo* BCNU release evaluated by AMS analysis of the plasma ^{14}C concentration of the blood samples from all successful activations. The plasma ^{14}C concentration remained at the background level following the unsuccessful activation on one rat, as shown in the first segment in Figure 5.3a.

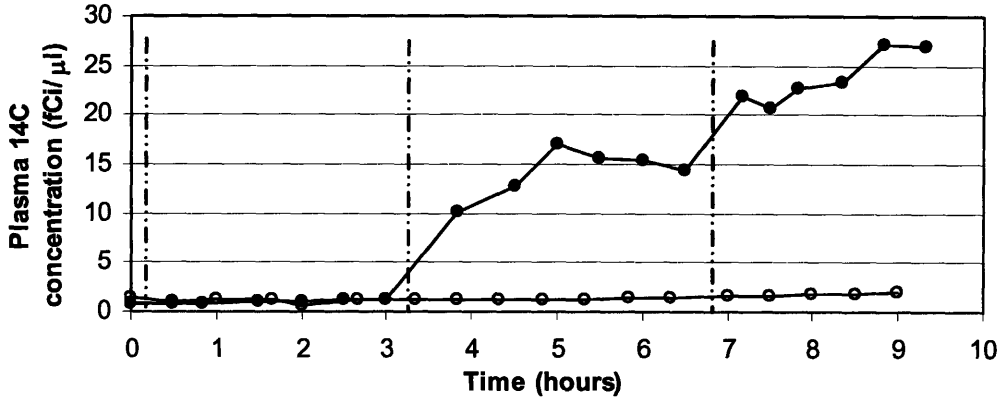

(a)

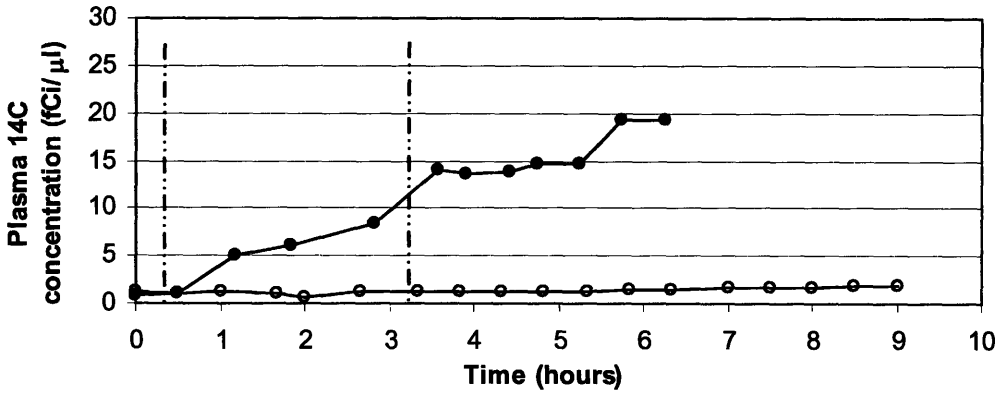

(b)

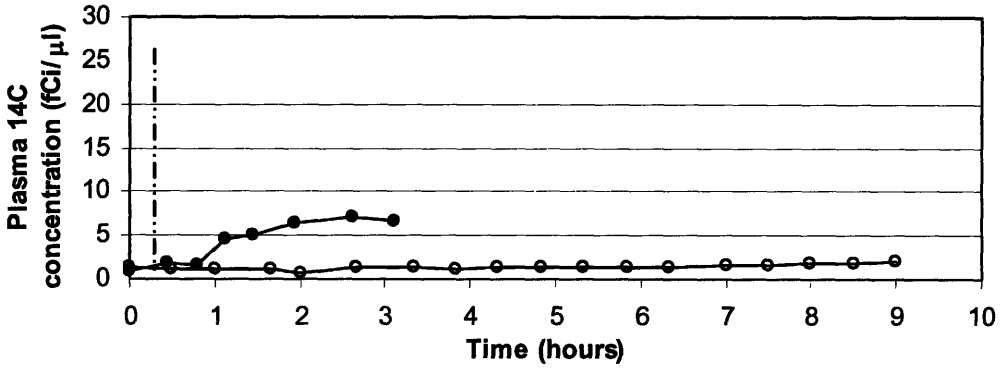

(c)

Figure 5.3 Plasma ^{14}C concentration measured by AMS from devices activated *in vivo*, with three sequential activations in (a), two activations in (b), and one activation in (c). Plasma ^{14}C concentration from an unactivated device is plotted in each graph (empty circle labeled) as controls. Each activation (denoted by the dashed line) corresponds to opening of one row of reservoirs with 0.01 μCi loading. Each data point represents means of 3~7 replicate measurements with 25 μL plasma sample.

All successful activations led to a sharp increase in the plasma ^{14}C concentration followed by a plateau, which is similar to both the *in vitro* (Figure 5.4) and injected controls (Figure 5.5). The ^{14}C level reached equilibrium almost instantaneously after each activation for the *in vitro* controls. It took about half an hour to reach the plateau plasma ^{14}C concentration for the injected control, and slightly longer for the rats with activated devices.

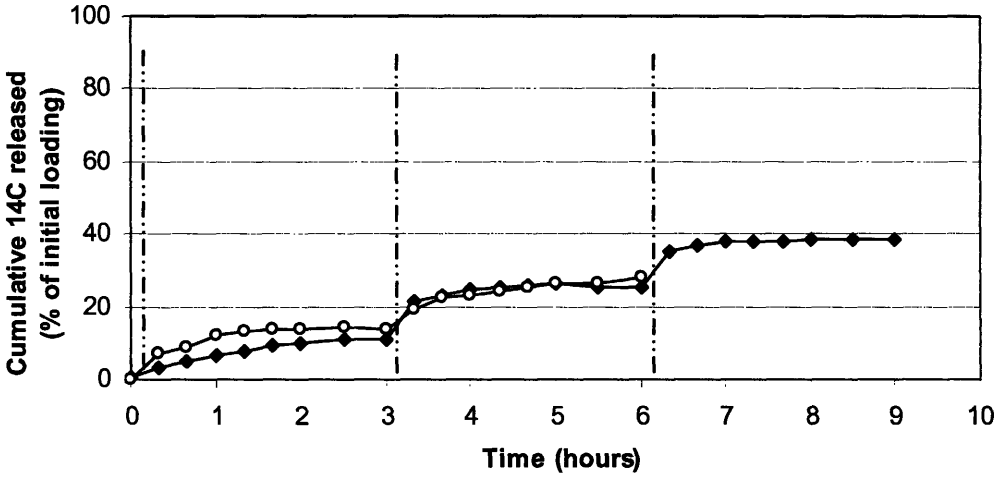

Figure 5.4 Cumulative ^{14}C released from devices activated *in vitro* in saline. Each activation (denoted by the dashed line) corresponds to opening of one row of reservoirs with 0.01 μCi loading. Plot from the same data in Figure 4.10.

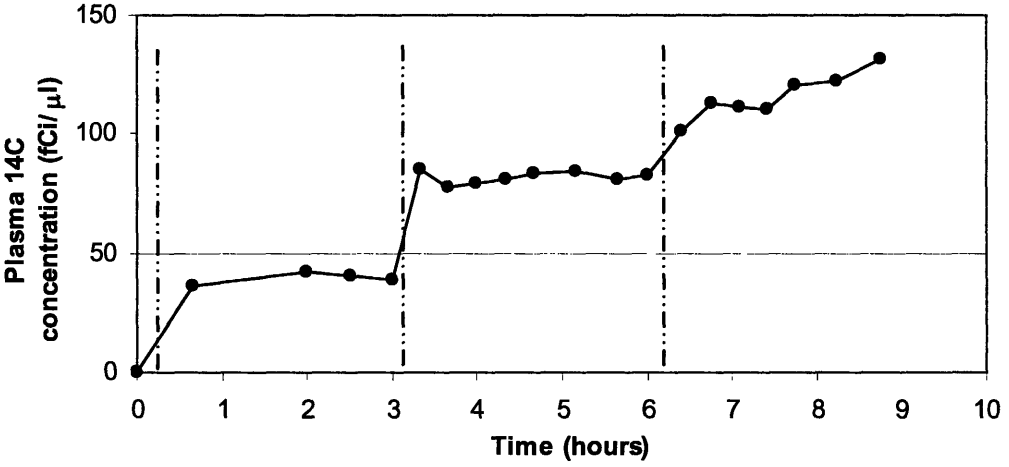

Figure 5.5 Plasma ^{14}C concentration measured by AMS from a subcutaneous injected control. Each injection (denoted by the dashed line) corresponds to 0.014 μCi loading. Each data point represents means of 3~7 replicate measurements with 25 μL plasma sample.

5.3.3 Discussion

The similarity in the shape of the ^{14}C labeled BCNU release profiles between the activated devices *in vivo* and both the *in vitro* and injected controls implies that the pharmacokinetics dominated the release kinetics in all cases. The time to reach the steady-state plasma ^{14}C concentration was on the order of one hour. The diffusion of ^{14}C labeled BCNU from the activated devices *in vivo* also played a role by prolonging the drug clearance time in the blood. Comparison of Figure 5.4 with Figure 5.3 shows that the intrinsic release rate from an activated device *in vitro* was faster than the distribution rate from an activated device *in vivo*. Clearly, the limiting resistance for *in vivo* distribution is external to the device. Comparison of Figure 5.5 with Figure 5.3 shows that more rapid distribution of BCNU occurred from the injected control than from activated devices. The drug was diluted in saline solution just before injection, but was mixed with the polyethylene glycol (PEG) gel in the reservoirs before activation. The difference in the release rate between the activated MEMS device and the injected control indicated that transport from a 50 μm opening into surrounding tissue was intrinsically slower than transport from a solution bolus delivered by injection.

It is also noted that the plasma ^{14}C concentration of the injected control was about three to five times higher than that of the rats with activated devices, even though the ^{14}C dosing of each injection was only 1.4 times the loading for each activation of the devices. The main reason is the incomplete release of payload from stainless steel frame packaged devices, as discussed in Chapter 4. The equilibrium plasma ^{14}C concentration after the first successful activations was about the same for two rats, but was nearly twice that value for the other rat with an activated device. This interindividual variability is probably due to the variability in the drug disposition between these animals, which may be correlated with the low partition and hence the low bioavailability of the drug in blood. Higher than tenfold interpatient variation in the blood level of BCNU has been reported in the clinical study of high dose alkylators for the treatment of primary breast cancer[11]. Majority of the unreleased radioactivity was found to be trapped in the neoprene gasket. Therefore, another possible reason for the different equilibrium plasma ^{14}C level was the different amount of radioactivity trapped in the neoprene gasket, although all devices were packaged and filled in the same manner and *in vitro* release of two devices

packaged in the same batch showed very little difference in the percentage of payload release among the three activations (Figure 5.4).

BCNU has been known to degrade in aqueous media with a half-life of 10 to 20 minutes[12]. There appears to be two competing degradation mechanisms. It can be enzymatically metabolized by the liver into an inactive form, or hydrolyzed in tissue to an active alkylating agent[13, 14]. BCNU has a relatively longer half-life in non-aqueous media, with 74 days in 95% ethanol[15]. Both the PEG gel and ^{14}C labeled BCNU were dissolved in ethanol for injection into the devices to avoid decomposition of the drug prior to release. Most of the measured ^{14}C in plasma probably represented the radioactivity carried by the degraded BCNU fragment, as proposed by DeVita[1]. This could explain the rapid clearance of the plasma ^{14}C level shown in Figure 5.3 and 5.5, although BCNU is known to be a highly lypophilic compound.

The blood volume (BV) of rats can be estimated using 7% of body weight[16] (BW). The rats used in our study weighed in the range of 150~200 grams. Using a middle value of 175 grams as the body weight, we can estimate the percentage of ^{14}C distribution in the blood:

$$^{14}C \text{ in blood } \% = \frac{\text{Plasma } ^{14}C \text{ conc.} \times BV}{^{14}C \text{ injected}} \qquad \text{(Equation 5.3)}$$

The plasma ^{14}C concentration can be read from Figure 5.5 to be 45 fCi/μL. Using a blood volume of 12.25 mL and 0.014 μCi injected loading, the percentage of ^{14}C that entered the blood was approximately 4 %. This value agrees with the reported 1~5 % range in literature[1].

The plasma ^{14}C concentration analysis gives acute release kinetics information with high temporal resolution. Measuring the excreted ^{14}C level is another approach to obtain release kinetics information on a longer time scale and with more direct data regarding mass balance[17].

5.4 Conclusions

The results of this study clearly demonstrate the feasibility of delivering BCNU from this drug delivery MEMS device *in vivo*. Use of AMS made it possible to obtain

accurate release kinetics of ^{14}C-BCNU *in vivo*. The BCNU release kinetics information also provides guidance for the tumor effect study presented in the next chapter.

5.5 Acknowledgements

All surgical procedures and animal care for the *in vivo* release study presented in this chapter were performed by Betty Tyler in Dr. Henry Brem's group at JHMI. The AMS work was performed under the auspices of the U.S. Department of Energy by University of California Lawrence Livermore National Laboratory (LLNL) under Contract W-7405-Eng-48 and in collaboration with the National Center for Research Resources Grant RR13461. Drs. Paul Henderson and John Vogel helped with the experimental design and coordination of the AMS sample analysis. Kurt Haack and Ester Ubeck prepared the AMS samples at LLNL.

5.6 References

1. DeVita, V.T., Denham, C., Davidson, J.D. and Oliverio, V.T. The physiological disposition of the carcinostatic 1,3-bis(2-chloroethyl)-1-nitrosourea (BCNU) in man and animals. *Clinical pharmacology and therapeutics* **8**, 566-577 (1967).
2. Turteltaub, K.W. and Vogel, J.S. Bioanalytical applications of accelerator mass spectrometry for pharmaceutical research. *Current Pharmaceutical Design* **6**, 991-1007 (2000).
3. Vogel, J.S., Turteltaub, K.W., Finkel, R. and Nelson, D.E. Accelerator mass spectrometry: isotope quantification at attomole sensitivity. *Analytical Chemistry* **67**, 353A-359A (1995).
4. Li, Y., Shawgo, R.S., Tyler, B., Henderson, P.T., Vogel, J.S., Rosenberg, A., Storm, P.B., Langer, R., Brem, H. and Cima, M.J. *In vivo* release from a drug delivery MEMS device. *Journal of Controlled Release* **100**, 211-219 (2004).
5. Vogel, J.S. Quantitating isotopic molecular labels with accelerator mass spectrometry, in Methods in Enzymology. (ed. A.L. Burlingame) (Academic Press, New York, NY; In Press).
6. Garner, R.C. and Leong, D. Pushing the accelerator - speeding up drug research with accelerator mass spectrometry. *Nuclear Instruments & Methods in Physics Research, Section B: Beam Interactions with Materials and Atoms* **172**, 892-898 (2000).
7. Garner, R.C., Barker, J., Flavell, C., Garner, J.V., Whattam, M., Young, G.C., Cussans, N., Jezequel, S. and Leong, D. A validation study comparing accelerator MS and liquid scintillation counting for analysis of ^{14}C-labelled drugs in plasma,

urine and fecal extracts. *Journal of Pharmaceutical and Biomedical Analysis* **24**, 197-209 (2000).

8. Gilman, S.D., Gee, S.J., Hammock, B.D., Vogel, J.S., Haack, K., Buchholz, B.A., Freeman, S.P.H.T., Wester, R.C., Hui, X. and Maibach, H.I. Analytical performance of accelerator mass spectrometry and liquid scintillation counting for detection of ^{14}C-labeled atrazine metabolites in human urine. *Analytical Chemistry* **70**, 3463-3469 (1998).
9. Buchholz, B.A., Freeman, S.P.H.T., Haack, K.W. and Vogel, J.S. Tips and traps in the ^{14}C bio-AMS preparation laboratory. *Nuclear Instruments & Methods in Physics Research, Section B: Beam Interactions with Materials and Atoms* **172**, 404-408 (2000).
10. Vogel, J.S. Rapid production of graphite without contamination for biomedical AMS. *Radiocarbon* **34**, 344-350 (1992).
11. Petros, W.P., Broadwater, G., Berry, D., Jones, R.B., Vredenburgh, J.J., Gilbert, C.J., Gibbs, J.P., Colvin, O.M. and Peters, W.P. Association of high-dose cyclophosphamide, cisplatin, and carmustine pharmacokinetics with survival, toxicity, and dosing weight in patients with primary breast cancer. *Clinical Cancer Research* **8**, 698-705 (2002).
12. Levin, V.A., Hoffman, W. and Weinkam, R.J. Pharmacokinetics of BCNU in man: a preliminary study of 20 patients. *Cancer treatment reports* **62**, 1305-1312 (1978).
13. Guaitani, A., Corada, M., Lucas, C., Lemoine, A., Garattini, S. and Bartosek, I. Pharmacokinetics of fotemustine and BCNU in plasma, liver and tumor tissue of rats bearing two lines of Walker 256 carcinoma. *Cancer Chemotherapy and Pharmacology* **28**, 293-297 (1991).
14. Hill, D.L., Kirk, M.C. and Struck, R.F. Microsomal metabolism of nitrosoureas. *Cancer Research* **35**, 296-301 (1975).
15. Montgomery, J.A., James, R., McCaleb, G.S. and Johnston, T.P. Modes of decomposition of 1,3-bis(2-chloroethyl)-1-nitrosourea and related compounds. *Journal of Medicinal Chemistry* **10**, 668-674 (1967).
16. Lee, H.B. and Blaufox, M.D. Blood volume in the rat. *Journal of nuclear medicine: official publication, Society of Nuclear Medicine* **26**, 72-76 (1985).
17. Shawgo, R.S. *In vivo* Activation and Biocompatibility of a MEMS Microreservoir Drug Delivery Device, Ph.D. Thesis, Massachusetts Institute of Technology, 2004.

6 Tumor effect study

6.1 Introduction and motivation

One specific objective of this NIH project is to evaluate efficacy of drug release from the MEMS device on a tumor model. We chose the tumor model because our collaborator, Dr. Henry Brem at Johns Hopkins Medical Institutions (JHMI) has pioneered local delivery of chemotherapeutic agents for treatment of malignant brain tumors and his group has extensive experience in the preclinical efficacy evaluation of various tumor models.

The efficacy evaluation of the drug delivery MEMS device on an experimental tumor model has been designed in three phases. Phase I study is designed to ensure proper device operation *in vivo* and to obtain BCNU dosage information necessary to choose the proper operating space for the BCNU/IL-2 combination therapy. Phase II study aims to develop dose-response curves for local delivery of combination BCNU/IL-2 therapy, and to determine the drug delivery regimen that most effectively retards or reverses growth of the tumor. Phase III study will evaluate the therapeutic regimen established in Phase II study in a 180-day survival study in order to compare the relative merit of the drug delivery MEMS technology with other existing technologies in improving the animal survival against the tumor challenge.

This chapter describes two animal tests performed in collaboration with Dr. Henry Brem's group at JHMI. The first test, though unsuccessful, presented the direction to modify the device packaging and drug formulation so that the second test accomplished the goal of Phase I study.

6.2 Experimental methods

6.2.1 Device fabrication and packaging

Devices (from Wafer # 070103-6) were fabricated using the same process described in Chapter 2. The gold electrodes were patterned by wet etching of the sputtered gold film.

Different packaging methods were used in the two animal studies. Sixteen devices in the first animal study were packaged using stainless steel frames with neoprene gaskets. Each packaged device was filled with a total BCNU dosage of 0.6 mg distributed evenly in 25 reservoirs. ^{14}C-BCNU was also filled into these reservoirs with a total loading of 0.04 μCi for each device. Details about the packaging and chemical filling can be found in Chapter 4.

Twenty-four devices in the second animal study were packaged using Pyrex frames and plates, using the same method described in Chapter 4 except that the bonding of the Pyrex chip to the Si device was achieved using anodic bonding instead of UV epoxy bonding. This change arose from the observation that occasionally a few gold membranes facing the reservoir opening became contaminated by the UV epoxy when the Pyrex chip was pressed against the Si device, which could affect the membrane opening. Detailed procedures of the anodic bonding can be found in Ho Duc's thesis[1]. Bonding of the Pyrex-Pyrex parts was still made using the UV epoxy. Another difference in the packaging is the absence of the top stainless steel frame from these devices in order to avoid discomfort and pain to the animals caused by the thin (250 μm thick) frame with larger lateral dimension (11 × 11 mm) than the Pyrex chips (7.5 × 5.5 mm). Devices were filled with mixture of ^{14}C-BCNU (Moravek Biochemicals, Brea, CA), BCNU (Bristol-Myers Squibb Co., Evansville, IN) and PEG (Mw 400) at 50:50 volume ratio between BCNU and PEG. Three BCNU dosages (0.67 mg, 1.2 mg and 2 mg) were used to fill these devices.

Both the stainless steel frame and Pyrex packaged devices used a blackened platinum wire (approximately 6mm long) as an *in vivo* reference electrode. The wire was soldered to the exposed end of one cable with epoxy covering the soldering joint. Packaged devices were shipped overnight to JHMI on dry ice.

6.2.2 Animal protocol

The two animal tests used the same general procedure but different experimental design in terms of number of animals, activation sequence, and controls, as described below.

6.2.2.1 General procedure

The tumor effect studies were performed in Dr. Henry Brem's group at JHMI. The animal study protocol was approved by the Animal Care and Use Committee of JHMI before implementation of any procedure.

Female rats (Fisher 344, weight 150~200 g) were purchased from Charles River. Some rats were housed in normal cages; while others were housed individually in metabolic cages (Nalgene model # 650-0100, Braintree Scientific Inc., Braintree, MA). The metabolic cage features a unique funnel and cone design that effectively separates feces and urine into tubes outside the cage. Animals were given standard rat chow and water *ad libitum* at the JHMI Animal Facilities. Animals housed in metabolic cages were given sugar water (4 tsp / 500 mL), which encouraged the animals to drink more and allowed more frequent collection of urine samples. The urine tubes were rinsed clean each time samples were taken. The metabolic cages were cleaned under flowing warm tap water every three days.

Animals were anesthetized prior to all surgical procedures using an intra-peritoneal injection of a stock solution containing ketamine hydrochloride (25 mg/mL), xylazine (2.5 mg/mL), and 14.25% ethyl alcohol in normal saline. Post-operative analgesics were given following every surgical procedure using a subcutaneous injection of buprenorphine (0.1mg/kg). All operating procedures were performed using sterile technique, with all instruments autoclaved and sterile gloves and masks worn throughout the procedure.

The 9L glioma, an experimental gliosarcoma syngeneic to the F344 rat, was maintained in the flank of a carrier rat. Each rat in the tumor effect study was implanted with a 2 mm^3 piece of 9L tumor from the carrier animal. Ten days after the tumor implantation, the rats were randomized into different groups to receive different treatment.

Sterilized devices were implanted subcutaneously next to the established tumor with the electrodes facing the tumor and the cable exiting through the incision. The incision was closed with autoclips. Animals were re-anesthetized on scheduled days for activation. Their original incision was prepped and opened to allow electrical connection

to the potentiostat. Following activation, the cable was cut flush at the end and returned to the subcutaneous pocket and the incision was closed with autoclips.

Tumor growth was evaluated using calipers three times a week and the tumor volume calculated using approximation of an ellipsoid:

$$V_{tumor} = Length \times Width \times Height \times \pi/6 \qquad \text{(Equation 6.1)}$$

Animals were checked daily for physical or behavioral evidence of toxicity, such as decreased alertness, impaired grooming, or gait disturbances. If any deficits developed, the animals would be euthanized by CO_2 inhalation and all organs removed for histological examination. The end point of the Phase I efficacy study was set at 22 days post tumor implantation. Animals were euthanized after experiments were completed by either CO_2 inhalation or a sodium pentobarbital overdose (200 mg/kg, to effect). Devices were explanted and shipped to MIT for optical microscopy inspection (Olympus BH-2).

Device activation was performed using the same protocol for the *in vivo* ^{14}C-BCNU release kinetics study in Chapter 5, which included four cathodic cleaning cycles from –1.0 to –1.5 V, four diagnostic scan cycles from 0 to 1.8 V, and 10-minute square wave voltammetry between 0 and 1.2 V, all relative to the blackened Pt wire reference electrode.

Excreted radioactivity from each rat housed individually in metabolic cages was analyzed to correlate with the tumor size measurement. Only urine samples were taken after an initial trial showed no radioactivity recovered in fecal samples. A 1 mL urine sample was mixed with 5 mL scintillation fluid (Ready Gel, Beckman Coulter Inc., Fullerton, CA) in a 7 mL scintillation vial and measured on a liquid scintillation counter (Beckman Coulter Inc., Fullerton, CA). A counting efficiency of 0.91 was used to convert the output data from counts per minute (CPM) to disintegrations per minute (DPM), which was then converted to radioactivity by a conversion factor of 2.2×10^6 DPM/μCi.

6.2.2.2 First tumor effect study

Twenty-four rats were divided into 5 groups 10 days after the tumor implantation that received different treatment, as described in Table 6.1. Controls for this study

included 4 rats with unactivated devices, 2 rats with empty devices, and 6 rats with no treatment.

Table 6.1 Animal grouping and device activation sequence for the first tumor effect study.

Rat #	Device #	Activation sequence	Notes
R1~R6	A1~A1	1 activation of full dose on 3/9/04	Rats housed in metabolic cages
R7~R12	A7~A12	1 activation of 2/5 dose on 3/9/04, 1 activation of 3/5 dose on 3/15/04	Rats housed in metabolic cages
R13~R16	U1~U4	1 activation of half dose on 7/1/04, 1 activation of another half dose on 7/6/04	Rats housed in metabolic cages
R17~R18	E1~E2	No activation	Empty chip control
R19~R24	N/A	N/A	No treatment control

6.2.2.3 Second tumor effect study

Forty-eight rats were divided into 8 groups 10 days after the tumor implantation that received different treatment, as described in Table 6.2. Controls for this study included 6 rats with unactivated devices, 3 groups of 18 rats with subcutaneously injected BCNU, and 6 rats with no treatment. Due to the limited number of metabolic cages available at the time of this study, 3 rats in each group were housed in metabolic cages for collection of urine samples for ^{14}C analysis, and the other 3 rats from each group were housed in normal cages. The tumor growth of all rats was monitored using a caliper.

The same BCNU/PEG mixture (at 50:50 volume ratio) that was used to fill the devices was used for the injection groups. Because of the difficulty in precisely controlling the injected volume manually using a 10 μL syringe, the actual dosage that the injected control rats received was higher than the target value. The actual amount of the injected dosage was estimated by comparing the scintillation counting data of the manually injected volume to that using a micropump.

Table 6.2 Animal grouping and device activation sequence for the second tumor effect study.

Rat #	Device #	Activation sequence	Notes
R1~R6	A1-1~A1-6 (0.67 mg BCNU)	1 activation of halfdose on 7/1/04, 1 activation of another half dose on 7/6/04	Metabolic cages used for Rats R1 ~ R3
R7~R12	A2-1~A2-6 (1.2 mg BCNU)	1 activation of half dose on 7/1/04, 1 activation of another half dose on 7/6/04	Metabolic cages used for Rats R7 ~ R9
R13~R18	A3-1~A3-6 (2 mg BCNU)	1 activation of half dose on 7/1/04, 1 activation of another half dose on 7/6/04	Metabolic cages used for Rats R13 ~ R15
R19~R24	U1-1~U1-6 (2 mg BCNU)	No activation	Metabolic cages used for Rats R19 ~ R21
R25~R30	0.67mg (1.4 mg) BCNU*	1 injection of half dose on 7/1/04, 1 injection of another half dose on 7/6/04	Metabolic cages used for Rats R25 ~ R27
R31~R36	1.3 mg (1.5 mg) BCNU*	1 injection of half dose on 7/1/04, 1 injection of another half dose on 7/6/04	Metabolic cages used for Rats R31 ~ R33
R37~R42	2 mg (2mg) BCNU*	1 injection of half dose on 7/1/04, 1 injection of another dose on 7/6/04	Metabolic cages used for Rats R37 ~ R39
R43~R48	N/A	N/A	No treatment control

*: The numbers before the parenthesis indicate the target BCNU dosage, and the numbers in parenthesis indicate the actual dosage that the injected control rats received.

6.3 Results and discussion

6.3.1 First tumor effect study

Figure 6.1 shows the tumor growth over time for the different treatment groups. No statistical difference was observed in the tumor size between rats with activated devices and unactivated controls or No treatment controls.

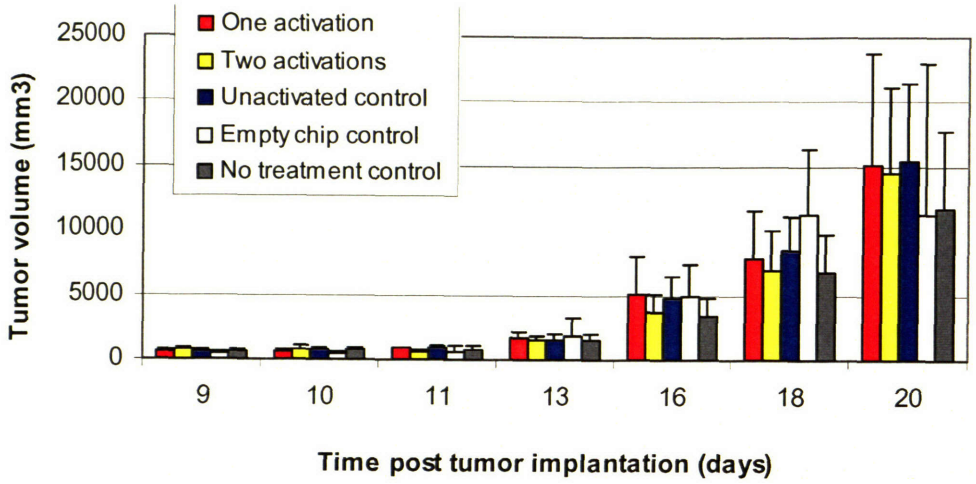

Figure 6.1 Tumor growth measurement for different treatment groups in the first tumor effect study.

The above tumor growth results could be correlated with the cumulative percentage of urinary ^{14}C recovery data shown in Figure 6.2. Optical microscopy examination on the explanted devices showed that 10 out of the 12 activated devices had more than 85% of the membranes fully opened. The other 2 devices had about 25% membrane opening rate, probably because of faulty wiring and/or insufficient fluid around the devices *in vivo*. The cumulative ^{14}C-BCNU excreted from the urine, however, was only a small portion (5-11%) of the total loading for all the activated devices. Our previous study showed about 60% urinary recovery of ^{14}C from a subcutaneously injected dose of ^{14}C-BCNU in the rat flank.

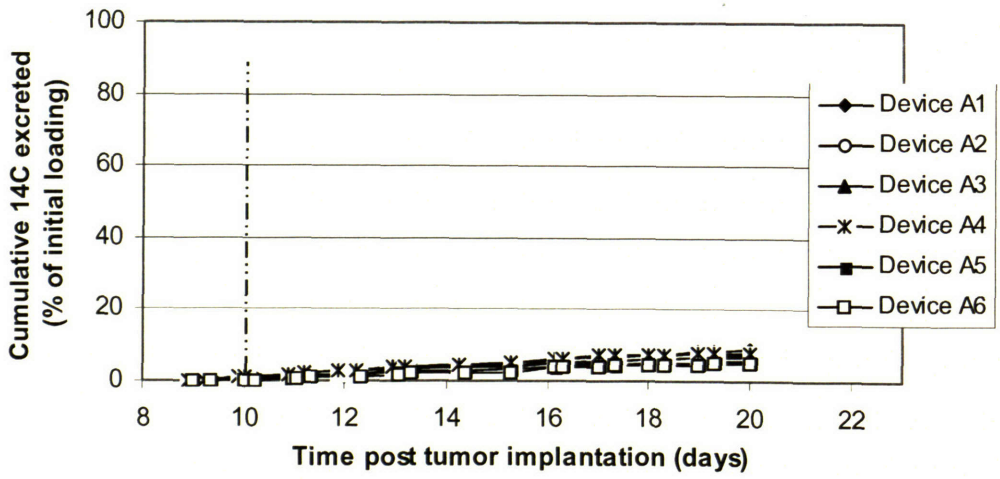

(a)

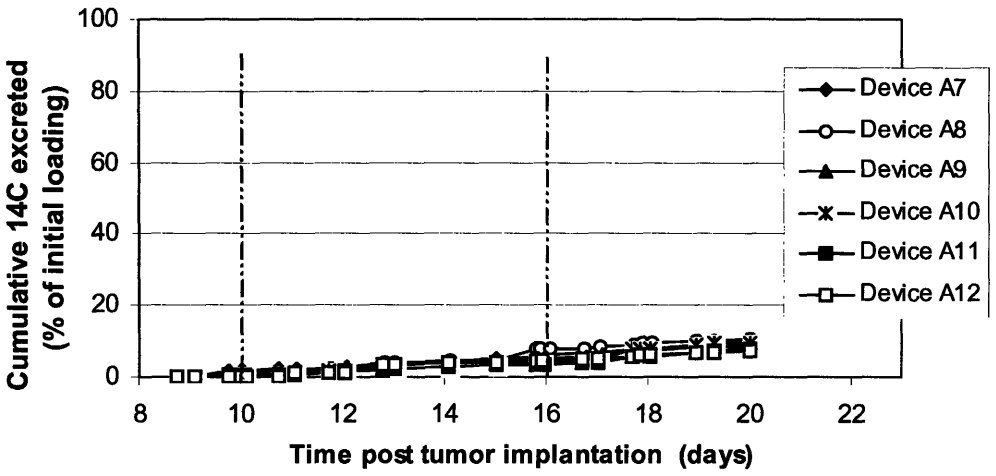

(b)

Figure 6.2 Cumulative percentage of ^{14}C excreted from urine in rats with (a) devices with 25 membranes activated on Day 10 and (b) devices with 10 membranes activated on Day 10 and 15 membranes on Day 16. Each device loaded with 0.04 μCi ^{14}C-BCNU and 0.6 mg BCNU.

Two *in vivo* activated devices were dissembled. Scintillation counting on the individual components soaked in deionized water overnight indicated a large amount of ^{14}C retained in the neoprene gasket (approximately 25%). About 5% radioactivity was also recovered from the packaging frames. Moreover, the *in vitro* BCNU release test also showed a very low percentage of payload release from devices filled with pure BCNU, but higher percentage of payload release with addition of polyethylene glycol (see Figure 4.10). All these results motivated the design of a Pyrex package and the investigation of drug formulation effect on BCNU release kinetics, as discussed in Chapter 4.

6.3.2 Second tumor effect study

The tumor growth over time in the second tumor effect study is shown in Figure 3. A noticeable difference between Figure 6.3 and Figure 6.1 is the much slower tumor growth in the rats that received activated devices or subcutaneous BCNU injections than the unactivated or No treatment control groups in the second study. Both the activated groups and injected control groups showed dose related retarding effect on the tumor growth; that is, the higher the BCNU dosage delivered, the slower the tumor growth. It is also interesting to note comparable tumor size between the activated groups and injected control groups with the same BCNU dosage.

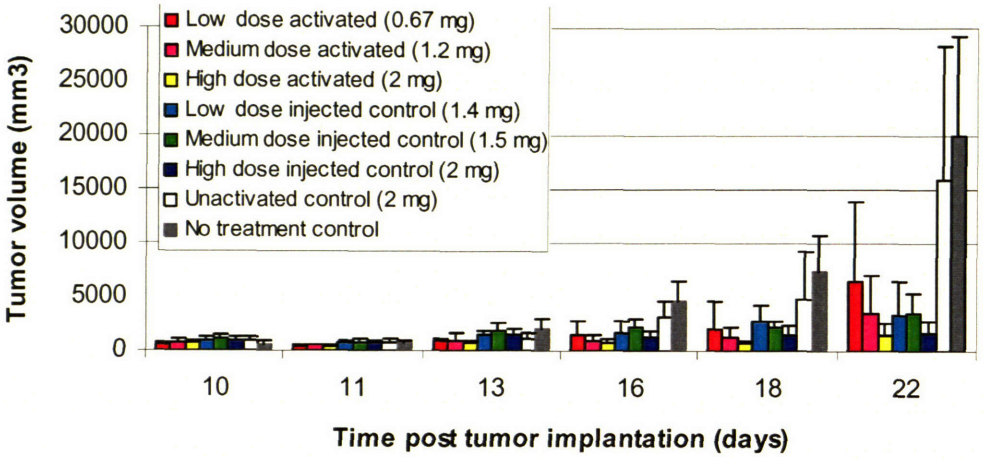

Figure 6.3 Tumor growth measurement for different treatment groups in the second tumor effect study. Each data point represents mean ± SD of measurements from 6 rats.

Figure 6.4 shows the cumulative percentage of ^{14}C excreted from the 3 rats housed in metabolic cages in each of the 3 groups that received activated devices. Optical microscopy examination of the explanted devices showed that all the activated devices had more than 80 % of the membranes fully opened except one device filled with 1.2 mg BCNU dosage. This device had all the membranes on top of the one macroreservoir opened, but none of the membranes on top of the other macroreservoir opened, or even showed any sign of corrosion. Optical microscopy did not show broken wire bonds on this device. A most probable explanation for the uncorroded membranes on this device could be that the membranes that were already activated in the first activation were activated again in the second activation by mistake. All urine counting and tumor measurement data from this device were excluded from further analysis. The urinary recovery of ^{14}C for all other devices after two activations was 51 ± 12 % of the initial loading.

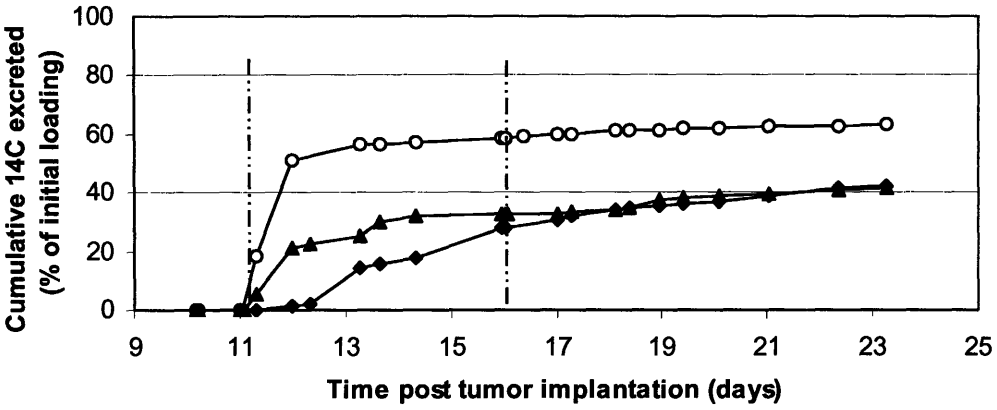

(a)

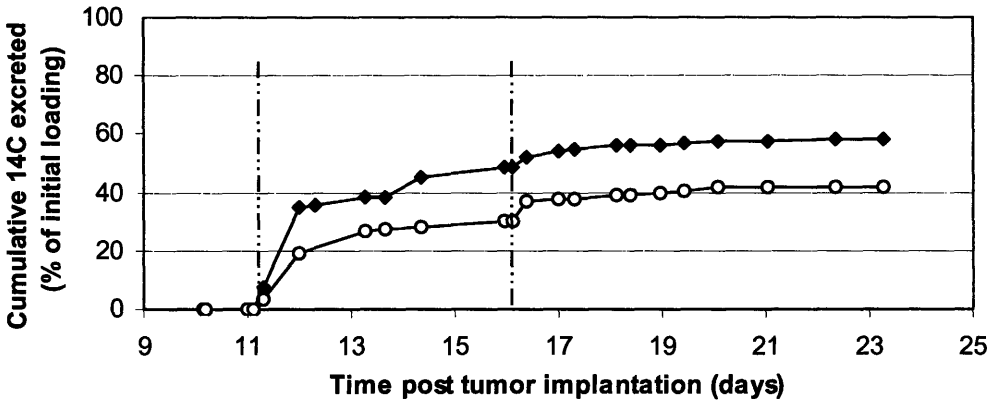

(b)

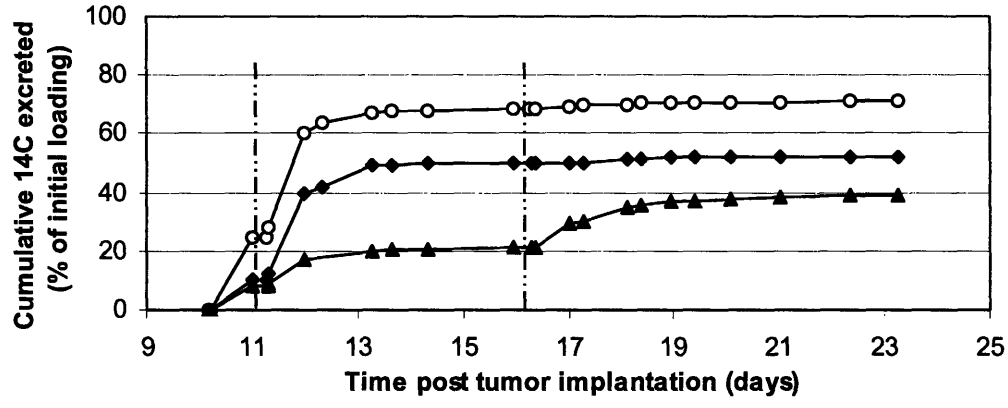

(c)

Figure 6.4 Cumulative percentage of ^{14}C excreted from rats with devices activated *in vivo* filled with different BCNU dosage (a) 0.67 mg, (b) 1.2 mg and (c) 2 mg. Dashed lines indicated time of activations to release half of the filled dosage.

The first device activation led to a sharp increase in the excreted ^{14}C level, which seemed to be cleared from urine within 1 day. The magnitude of increase in the urinary ^{14}C level after the second activation was much smaller than after the first activation for majority of the rats housed in metabolic cages with activated devices. The 3 devices with high BCNU dosage leaked only one day after implantation (Figure 6.4c). The 3 unactivated control devices also showed leakage of ^{14}C within 3 to 5 days after implantation (Figure 6.5).

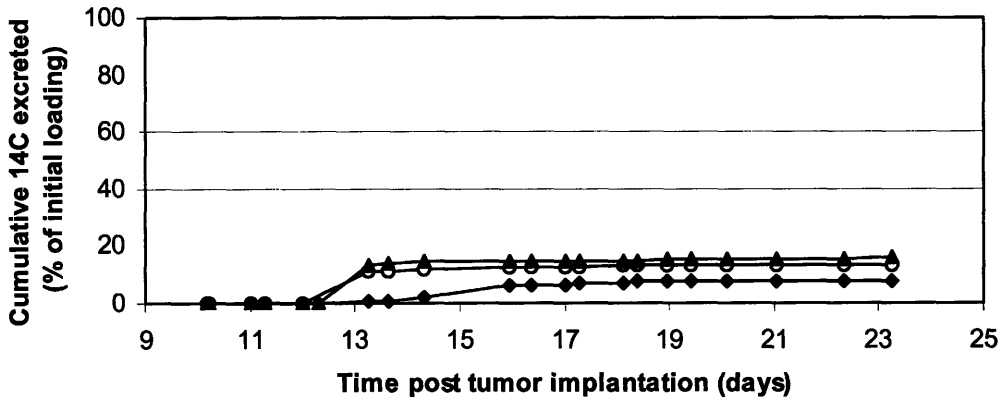

Figure 6.5 Cumulative percentage of ^{14}C excreted from rats with unactivated devices filled with 2 mg BCNU dosage.

The cumulative ^{14}C release profiles of the injected control groups showed two clear plateaus within 1 day after the injection (see Figure 6.6). The urinary recovery of ^{14}C was 57 ± 13 % of the total injected loading.

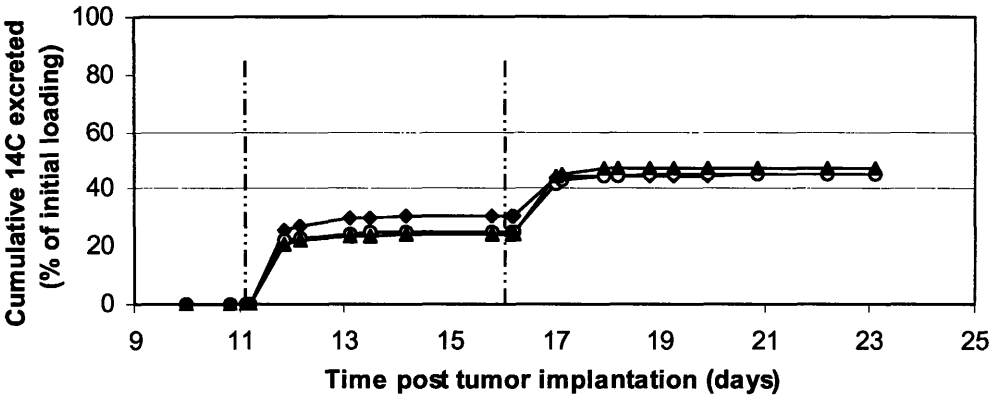

(a)

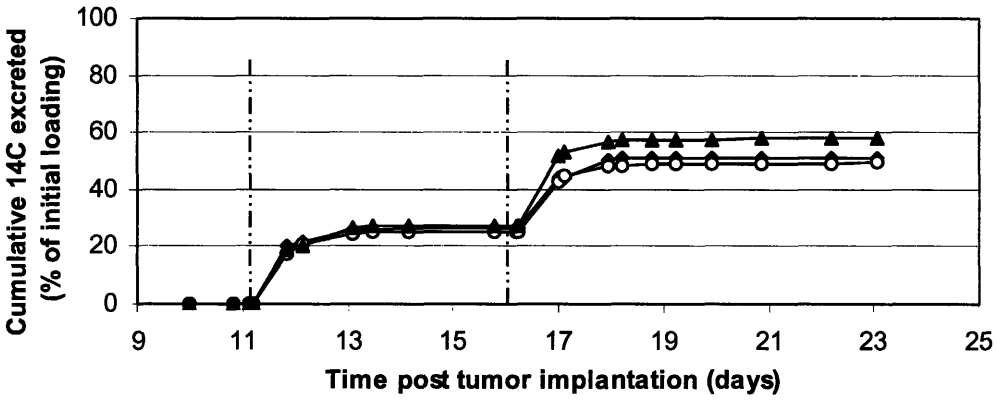

(b)

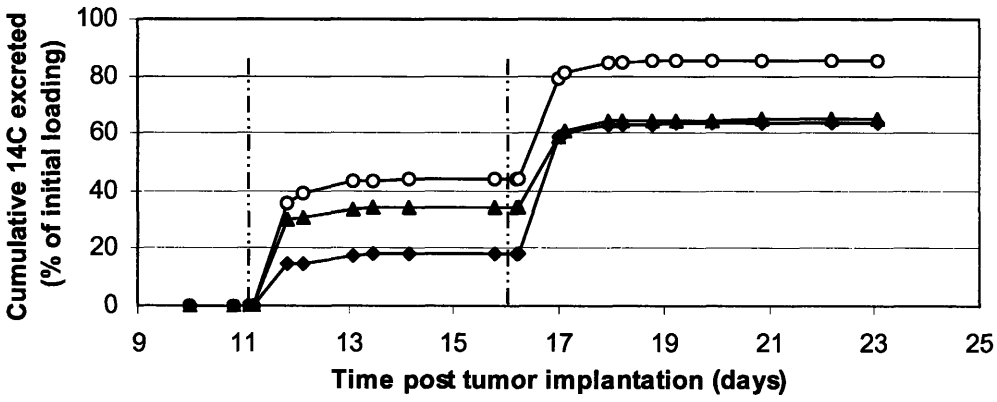

(c)

Figure 6.6 Cumulative percentage of ^{14}C excreted from subcutaneously injected control groups with BCNU dosages of (a) 1.4 mg (b) 1.5 mg and (c) 2 mg.

6.3.3 Discussion

Results from the second tumor effect study successfully demonstrated the efficacy of BCNU released from the drug delivery device on the 9L rat flank tumor model. This success comes from improvement in the device packaging and drug formulation over the first unsuccessful tumor effect study. The Pyrex package effectively enhanced the device capacity without increasing the overall package dimension. Co-formulation of PEG with BCNU led to complete and rapid release of drug *in vivo*, as supported by the closeness in the urinary ^{14}C level and clearance time between the activated device groups and the injected control groups.

Rats with activated devices showed comparable tumor growth data to rats with subcutaneous injections, indicating that the device packaging, shipping and gold membrane corrosion processes did not seem to affect the therapeutic effect of BCNU delivered from the activated devices. The antitumor activity of BCNU arises from its alkylating decomposition products that induce DNA crosslinking and kill cells[2]. Sealing of the MEMS device after BCNU filling was made by 20-second UV exposure. A colorimetric assay[3] (conducted by Helen Tsai and Grace Kim) has shown very similar slope of the standardization curves from BCNU samples with and without 1-minute UV exposure, suggesting that the UV exposure did not change the activity of the drug. It is unclear whether the corrosion process had an effect on the decomposition of BCNU contained inside the reservoirs. Nevertheless, BCNU delivered from the activated drug delivery device seemed to exhibit similar antitumor activity to BCNU directly delivered from injection. On the other hand, this conclusion may not be applicable to other therapeutic agents delivered from the drug delivery device. Appropriate *in vitro* assays will be necessary to evaluate the influence of filling methods and device activation on the drug activity and to ensure that the drugs remain active prior to release.

It is interesting to compare the tumor growth data from this study with those using other BCNU local delivery technologies. Figure 6.7 shows the tumor volume 22 days post tumor implantation for rats implanted with the MEMS device, with the GLIADEL® wafer (a polyanhydride based copolymer wafer with BCNU distributed uniformly in the wafer[4]), and with the polymer chip (a resorbable polymeric device with rows of drug containing reservoirs each covered by a biodegradable polymer[5]) at different BCNU

dosages. The data at zero BCNU dosage correspond to results from no chip/wafer control groups. The variation in the tumor volume of these control groups makes it difficult to conclude if there was statistically significant difference in the efficacy between the pulsatile release from the MEMS device and the sustained release from the polymer systems on this flank tumor model. Sustained delivery of BCNU from both the GLIDEL® wafer and poly (L-lactide co-glycolide) (PLG) microspheres have been shown to be statistically more effective than the equipotent bolus injection of BCNU to enhance survival in rat glioma models[6-8]. Further study is needed to directly evaluate the efficacy of the MEMS device comparing to the polymer systems against the 9L tumor model. On the other hand, sustained delivery of BCNU can also be achieved using the MEMS device simply by sequential superposition of the pulsatile profiles from many individual reservoirs.

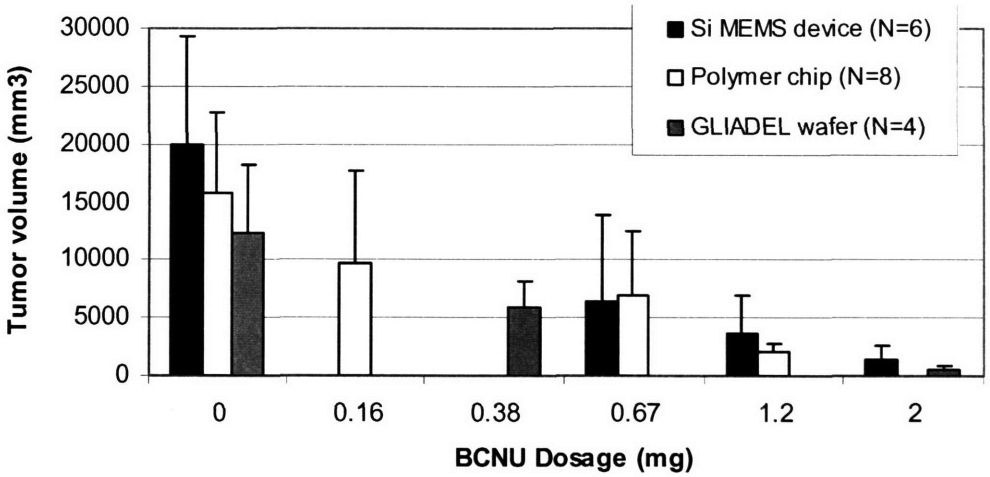

Figure 6.7 Tumor volume measured 22 days after tumor implantation in the rat flank using different delivery vehicles.

Some devices showed unexpectedly earlier leakage of payload *in vivo* (3~5 days after device implantation) comparing to the *in vitro* leak test result (zero leakage up to 12 days). A possible reason could be the damage of gold membranes due to the direct contact of the device top surface with the animal tissue. Optical microscopy examination on the explanted devices showed at least one broken anode gold membrane on 5 out of the 6 unactivated devices. About one third of all the explanted devices (including both the

activated and the unactivated devices) had broken membranes on the cathode too. Therefore, it is proposed that a protective frame be added on top of the device packaging in order to prevent the premature drug leakage due to broken gold membranes in future *in vivo* studies.

It is also noted that despite the leakage of the unactivated devices, the tumor growth of this group was hardly inhibited comparing to the activated and No treatment control groups. It was observed at the time of the first activation that the cable attached to the device was too long, which displaced the Si device from the tumor site by about 10 mm. The device was pulled back with the electrode surface facing the tumor before the activation. After activation, the cable was cut short to ensure close contact of the device with the tumor after the incision was closed. No action was taken to the rats with unactivated devices. It is suspected that majority of the leaked drug from the unactivated devices was not able to diffuse to the tumor site to inhibit its growth.

6.4 Conclusions

BCNU delivered from the MEMS device has shown efficacy against the growth of a 9L flank tumor in rats. Co-formulation of BCNU with PEG led to complete and rapid release of drug *in vivo*. The retarding effect of BCNU on the tumor growth was dose dependent in the range of 0.67 ~ 2 mg investigated in this chapter. BCNU delivered from activated devices seemed to be as effective as equipotent injections of BCNU in retarding the tumor growth. These results provide important BCNU dosage information for the second phase efficacy study. The drug leakage problem discovered from the *in vivo* study should be addressed before the next efficacy study. It may also be necessary to test leakage of any proposed new packaging method *in vivo* to ensure that the leakage problem is indeed solved.

6.5 Acknowledgements

All surgical procedures and animal care for the *in vivo* release study presented in this chapter were performed by Betty Tyler in Dr. Henry Brem's group at JHMI. Hong Linh Ho Duc assisted with the device activation in the first tumor effect study. He also

fabricated all the Pyrex chips and performed the anodic bonding in packaging the devices used in the second tumor effect study. Tiffany Williams, a summer student in Dr. Henry Brem's lab from University of California at San Francisco, assisted with the animal surgery and care in the second tumor effect study. Dr. Malinda Tupper helped with the experimental design of both tumor studies.

6.6 References

1. Ho Duc, H.L. Packaging for a drug delivery microelectromechanical system, Master's Thesis, Massachusetts Institute of Technology, 2004.
2. Kohn, K.W. Interstrand cross-linking of DNA by 1,3-bis(2-chloroethyl)-1-nitrosourea and other 1-(2-haloethyl)-1-nitrosoureas. *Cancer Research* **37**, 1450-1454 (1977).
3. Loo, L.T. and Dion, R.L. Colorimetric method for the determination of 1,3-bis(2-chloroethyl)-1-nitrosourea. *Journal of Pharmaceutical Sciences* **54**, 809-810 (1965).
4. Brem, H. and Langer, R. Polymer-based drug delivery to the brain. *Science & Medicine (Philadelphia)* **3**, 52-61 (1996).
5. Grayson, A.C.R., Choi, I.S., Tyler, B.M., Wang, P.P., Brem, H., Cima, M.J. and Langer, R. Multi-pulse drug delivery from a resorbable polymeric microchip device. *Nature Materials* **2**, 767-772 (2003).
6. Buahin, K.G. and Brem, H. Interstitial chemotherapy of experimental brain tumors: comparison of intratumoral injection versus polymeric controlled release. *Journal of neuro-oncology* **26**, 103-110 (1995).
7. Emerich, D.F., Winn, S.R., Hu, Y., Marsh, J., Snodgrass, P., LaFreniere, D., Wiens, T., Hasler, B.P. and Bartus, R.T. Injectable chemotherapeutic microspheres and glioma I: enhanced survival following implantation into the cavity wall of debulked tumors. *Pharmaceutical Research* **17**, 767-775 (2000).
8. Emerich, D.F., Winn, S.R., Snodgrass, P., LaFreniere, D., Agostino, M., Wiens, T., Xiong, H. and Bartus, R.T. Injectable chemotherapeutic microspheres and glioma II: enhanced survival following implantation into deep inoperable tumors. *Pharmaceutical Research* **17**, 776-781 (2000).

7 Conclusions and future study

7.1 Summary of results

This thesis presents an in-depth study on the mechanical integrity of gold membranes on the drug delivery MEMS device. The *in vivo* operation of the device has been evaluated using a chemotherapeutic agent against a flank tumor model.

A bulge test apparatus was constructed to pressurize the gold membrane from underneath and to measure the membrane deflection using optical interferometry. Fitting the deflection and pressure data to an available bulge equation allowed extraction of the elastic modulus and residual stress of the gold membrane. Different processing conditions led to different gold membrane microstructure and mechanical properties. The bulge test was also used combined with an *in situ* observation setup to study the electrochemical disintegration process of the gold membranes in chloride containing solutions. A gradual loss of the membrane mechanical integrity was observed with progression of corrosion. The gold membrane disintegration probably occurred by a combination of membrane thinning through active dissolution and accumulation of plastic deformation due to the transient formation of a passive film on top of the gold membrane.

In vivo release of a chemotherapeutic agent, BCNU, from the drug delivery device was demonstrated in a rat flank model. Acute temporal release kinetics of ^{14}C-BCNU *in vivo* was evaluated by analysis of the plasma ^{14}C concentration using the accelerator mass spectrometry (AMS) technique. Furthermore, BCNU delivered from the drug delivery device showed a dose dependent retarding effect on the growth of a 9L flank tumor model in rats.

The mechanical characterization studies presented in this thesis provided a deeper understanding of the materials science issues related with the drug delivery device so that the device yield and quality could be improved through optimized processing conditions. Obtaining high quality devices was critical to the success of evaluating their *in vivo* operation. The *in vivo* studies provided preliminary efficacy validation of the drug delivery device as well as important dosage information for further efficacy evaluation. All these results also provided guidance for further improvement and more comprehensive evaluation of the device operation *in vivo*.

7.2 Future work

7.2.1 Dielectric coating for long term implantation and operation

This thesis has focused on the processing optimization of the gold membranes on the drug delivery device. Another component that may need further processing optimization for reliable long term operation is the dielectric passivation coating that is patterned on the device surface to protect part of the gold electrode (traces) from unwanted corrosion.

Key requirements for the dielectric coating include biocompatibility, stability and hermeticity. The current MEMS device uses silicon dioxide (SiO_2) grown by plasma enhanced chemical vapor deposition (PECVD) as the passivation layer. *In vivo* test of this material using the cage implant system has shown good biocompatibility and superior biofouling reduction compared to unmodified silicon[1]. However, long term (up to 6 months) *in vivo* studies showed a significant detachment and dissolution of SiO_2 within two months post-implantation[2]. There is also literature reporting the dissolution of SiO_2 films from retinal implants after subretinal implantation in rabbits for 6-12 months[3].

Other materials, such as silicon nitride (SiN_x, x here denoting nonstoichiometric nitride) or amorphous silicon carbide[4] (*a*-SiC:H) can be explored to replace SiO_2 as the dielectric coating suitable for long term implantation and operation of the MEMS device. Adhesion of the dielectric coating to the gold is critical to ensuring long term stability of the coating. The "Scotch tape test" provides a quick qualitative evaluation of the adhesion property of the coating[5]. Chronic soaking tests can be performed to measure the coating dissolution rate in PBS. Candidates that show superior properties in the above *in vitro* tests will be further evaluated for long term biocompatibility and stability *in vivo*.

7.2.2 Improvement of membrane opening reliability *in vivo*

Current drug delivery devices use electrochemical corrosion to open the gold membranes for drug release. Results from Chapter 3 showed that the non-uniform nature of the corrosion process led to scatter in the time needed to open a membrane, and that 10-minute square wave voltammetry was sufficient to achieve 100% opening of all the

membranes on one device *in vitro*. However, results from Chapter 5 and Chapter 6 showed approximately 85 % success of membrane opening *in vivo*. Possible reasons for the failure in membrane opening may include wrong wiring, insufficient body fluid, breakdown of electric path due to scratch on the dielectric coating along the trace, or adhesion of proteins or other molecules on the gold surface. It is important to address these problems in order to achieve failsafe operation of the device *in vivo*.

Results from Chapter 3 showed that blackening the platinum reference electrode improved the reproducibility of the cyclic electrochemical results. The blackening approach can also be applied to the gold membranes for more reproducible opening. Christopher Puleo and Nolan Flynn have developed an electrodeposition process to blacken the anode gold membranes. Further study is needed to test whether this procedure has the intended effect to improve the reproducibility of membrane opening *in vivo*. Device with blackened gold membranes should also be tested for leakage to ensure that the blackening procedure does not compromise the integrity of the gold membranes. Another possible area of improvement is the voltammetry parameters for activating the gold membranes, including the time and potential range of the cathodic cleaning stage, and the potential range, duty cycle and frequency of the square wave voltammetry. Further investigation of the plastic deformation of the corroded gold membranes may provide useful guidance in the optimization of activation parameters.

An alternative approach is to adopt a fuse activation mechanism that uses resistive heating to melt the membranes. One obvious advantage of the fuse activation mechanism is that it does not need the presence of chloride ions for the membrane activation, and thus is expected to exhibit higher operation reproducibility than the electrochemical activation mechanism. Hong Linh Ho Duc has successfully demonstrated this mechanism *in vitro* on devices with modified electrode design. Further study will focus on optimization of the membrane materials, evaluation of the biological response of this mechanism, and *in vivo* evaluation of the device operation reliability.

7.2.3 Delivery of IL-2/BCNU combination therapy to the tumor model

Interleukin-2 (IL-2) is a cytokine that exerts a number of immunomodulatory activities in a paracrine fashion, including enhancement of the T cell growth, T cell activation, cytotoxic T lymphocyte growth and natural killer cell activation[6, 7]. Local delivery of IL-2, either by genetically engineered tumor cells or by gelatin/chondroitin sulphate polymer microspheres, in combination with the local delivery of BCNU from biodegradable polymers, has recently been shown to achieve synergistic efficacy in various animal tumor models[8, 9]. Precise control of the delivery timing and dosage of IL-2 and BCNU is critical to achieving optimal efficacy, which is nevertheless difficult to achieve using the available polymer wafer system. Therefore, the IL-2/BCNU combination therapy provides a suitable experimental paradigm for evaluating the efficacy of the drug delivery MEMS device.

Further efficacy evaluation of delivering the IL-2/BCNU combination therapy from the drug delivery device on the 9L flank tumor model will be conducted based on the Phase I study completed in this thesis. IL-2 is a protein drug. It is important that IL-2 retain its activity during the filling, sealing and other handling processes. Studies are currently being carried out by Grace Kim to develop *in vitro* IL-2 activity assays so that the influence of drug formulation, device packaging and activation on the IL-2 contained in the reservoirs can be evaluated. A series of dose ranging studies, using similar protocols as in the Phase I study, will be conducted to establish the optimal IL-2 and BCNU dosages and delivery sequence that most effectively retards the tumor growth. *In vivo* release profiles of radiolabeled IL-2/BCNU combination will also be evaluated to correlate with the tumor effect study results. The capacity of the current Pyrex packaged device is expected to be sufficient to contain therapeutic amounts of IL-2 and BCNU. However, the Pyrex chip design may need to be modified to contain more compartments and hence allow more impendent release events from one device.

The optimized treatment regimen established from the dose ranging study will be evaluated in the Phase III survival study with 180-day duration. Results will be compared with currently available therapies using the BCNU polymer wafer, the IL-2 microspheres, or their combination to evaluate the relative merit of the drug delivery MEMS technology against the challenge of the 9L flank tumor model.

7.2.4 Exploration of other applications

The tumor model is a suitable experimental paradigm for evaluating the efficacy of the drug delivery MEMS device with promises of leading to useful clinical applications. This device has also been used to locally deliver an antioxidant drug as inducers for gene regulation in a nude mouse model. Both *in vitro* and *in vivo* studies have shown successful induction evaluated by the luciferase assay. Further study will investigate the delivery of both the gene coded virus and inducer from one device *in vivo*. At the same time, this device can be used to deliver a wide array of other therapeutic agents that capitalize on the unique capability of the device to locally deliver multiple substances with precise control of the dosages and temporal profiles. An even broader perspective, however, is to envision the MEMS technology, the key design principle of this drug delivery device, as a uniquely powerful platform for improved physiological integration of the chemical or physical stimuli with the delicate systems of the human body than is currently available in clinical or commercial treatments[10].

7.3 References

1. Voskerician, G., Shive, M.S., Shawgo, R.S., Recum, H.v., Anderson, J.M., Cima, M.J. and Langer, R. Biocompatibility and biofouling of MEMS drug delivery devices. *Biomaterials* **24**, 1959-1967 (2003).
2. Voskerician, G. Long term non-functional drug-free biocompatibility and biofouling of MEMS drug delivery devices. Unpublished.
3. Hammerle, H., Kobuch, K., Kohler, K., Nisch, W., Sachs, H. and Stelzle, M. Biostability of micro-photodiode arrays for subretinal implantation. *Biomaterials* **23**, 797-804 (2001).
4. Cogan, S.F., Edell, D.J., Guzelian, A.A., Liu, Y.P. and Edell, R. Plasma-enhanced chemical vapor deposited silicon carbide as an implantable dielectric coating. *Journal of Biomedical Materials Research, Part A* **67A**, 856-867 (2003).
5. Ohring, M. Materials Science of Thin Films, Deposition and Structure., Second Edition. (Academic Press, San Diego, CA; 2002).
6. Fearon, E.R., Pardoll, D.M., Itaya, T., Golumbek, P., Levitsky, H.I., Simons, J.W., Karasuyama, H., Vogelstein, B. and Frost, P. Interleukin-2 production by tumor cells bypasses T helper function in the generation of an antitumor response. *Cell (Cambridge, MA, United States)* **60**, 397-403 (1990).
7. Pardoll, D.M. Paracrine cytokine adjuvants in cancer immunotherapy. *Annual Review of Immunology* **13**, 399-415 (1995).

8. Rhines, L.D., Sampath, P., DiMeco, F., Lawson, C., Tyler, B.M., Hanes, J., Olivi, A. and Brem, H. Local immunotherapy with interleukin-2 delivered from biodegradable polymer microspheres combined with interstitial chemotherapy: a novel treatment for experimental malignant glioma. *Neurosurgery* **52**, 872-879; discussion 879-880 (2003).

9. Sampath, P., Hanes, J., DiMeco, F., Tyler, B.M., Brat, D., Pardoll, D.M. and Brem, H. Paracrine immunotherapy with interleukin-2 and local chemotherapy is synergistic in the treatment of experimental brain tumors. *Cancer Research* **59**, 2107-2114 (1999).

10. Grayson, A.C.R., Shawgo, R.S., Johnson, A.M., Flynn, N.T., Li, Y., Cima, M.J. and Langer, R. A bioMEMS review: MEMS technology for physiologically integrated devices. *Proceedings of the IEEE* **92**, 6-21 (2004).